

MULTISCALE MODELING OF
THE HYGRO-MECHANICAL
RESPONSE OF PAPER SHEETS

PRIYAM SAMANTRAY

A catalogue record is available from the Eindhoven University of Technology Library.
ISBN: 978-90-386-4768-5

Cover design by Loeloe Vermuelen.
Printed by PROEFSCHRIFTMAKEN, The Netherlands.

© Copyright, 2019, Priyam Samantray. All rights reserved. No part of this publication may be reproduced, stored in a retrieval system, or transmitted, in any form or by any means, electronic, mechanical, photocopying, recording or otherwise, without prior permission of the author.

This document was typeset using the typographical look-and-feel `classicthesis` developed by André Miede and Ivo Pletikosić.

The research described in this thesis has been funded by the European Commission through an Erasmus Mundus grant in the framework of the Simulation in Engineering and Entrepreneurship Development program. Also, it has been funded by Océ, A Canon Company.

MULTISCALE MODELING OF THE HYGRO-MECHANICAL RESPONSE OF PAPER SHEETS

PROEFSCHRIFT

ter verkrijging van de graad van doctor aan de Technische
Universiteit Eindhoven, op gezag van de rector magnificus prof.dr.ir.
F.P.T. Baaijens, voor een commissie aangewezen door het College
voor Promoties, in het openbaar te verdedigen op donderdag 16 mei
2019 om 13:30 uur

door

PRIYAM SAMANTRAY

geboren te Bhubaneswar, India

Dit proefschrift is goedgekeurd door de promotoren en de samenstelling van de promotiecommissie is als volgt:

voorzitter:	Prof.dr.ir. A.A. van Steenhoven
1 ^e promotor:	Prof.dr.ir. M.G.D. Geers
2 ^e promotor:	Prof. T.J. Massart (Université libre de Bruxelles)
copromotor:	dr.ir. R.H.J. Peerlings
leden:	Prof.dr.ir. H.M.A. Wijshoff
	Assoc. Prof. B. François (Université libre de Bruxelles)
	Prof. S. Östlund (KTH Royal Institute of Technology)
	Assoc. Prof. P. Berke (Université libre de Bruxelles)

Het onderzoek of ontwerp dat in dit proefschrift wordt beschreven is uitgevoerd in overeenstemming met de TU/e Gedragscode Wetenschapsbeoefening.

Logic will get you from A to B. Imagination will take you everywhere.

— Albert Einstein

S U M M A R Y

Paper sheets reveal pronounced changes in shape and dimensions upon exposure to variations in moisture, which comprises digital printing operations. These are observed in the form of curls, waviness and buckling at the sheet-scale of paper. In digital printing, this undesired behavior is due to the fact that the moisture is rapidly absorbed in paper and thereafter evaporated within a short period of time.

These dimensional changes originate from the single fibre level, which affects the fibre network through the inter-fibre bonds (regions where the fibres overlap). At these bonds, an interaction of the hygroscopic and mechanical response of the fibres occurs, entailing micro-stresses and associated sheet-scale deformations. In order to understand this macro-scale behavior of paper, it is essential to study the complex fibrous network at the micro-scale.

In Chapter 2, a level-set based XFEM approach is used to model the hygro-elastic response of complex fibrous networks in a two dimensional framework. The fibres are assumed to be completely bonded in the inter-fibre bonds. The fibre edges are described by the zero level-set of a higher dimensional function. The level-set method coupled with X-FEM captures the geometrical description of the fibres adequately with a lower system size, since the discretization is decoupled from the geometry. Therefore, LS-XFEM formalism is shown to be successful in modeling the hygo-mechanical response of complex networks of fibres.

During the manufacturing process of paper, when the pulp is dried under restraint, internal stresses/strains are developed as explained by the fibre segment activation mechanism. Upon exposure to a moisture cycle (e.g. during printing), these strains are released at the fibre level which induces permanent deformations at the macro-scale accompanied by dimensional instabilities. To capture such phenomena, a rate-independent kinematic hardening plasticity model is developed for the individual fibres in Chapter 3. The results obtained from the numerical network simulations using this model illustrate the influence of microstructural properties of the network (e.g. the fraction of free-standing fibres versus bonded fibres) on the macroscopic irreversible strains.

In addition to printing, the moisture infiltration in paper occurs also via the environment. Under sustained loading over a period of time, creep takes place in paper networks. These macroscopic deformations observable in paper networks over time are of great interest due to the lack of a suitable model that explains this behavior. Furthermore, this intrinsic time-dependence is of significant importance for the service conditions of paper packaging products. In order to understand the effects of time scales on the dimensional alterations in paper, a rate-dependent plasticity model based on a power law is adopted in Chapter 4. The model parameters are identified from experimental results performed on single paper fibres (Jentzen [32] and Sedlachek [64]). Thereafter, network simulations are performed, which demonstrate the time dependence at the sheet level.

In order to understand the role of the degree of bonding between the fibres in bonded regions on the sheet-scale response of the network, the assumption in Chapters 2, 3 and 4 of a full kinematic

constraint between fibres at the bonds is partially relaxed in Chapter 5. In the relaxed bond model, the fibres in bonds can have independent displacements, whereby the displacement difference is governed by interfacial stiffness. This is modeled numerically by embedded interfacial elements that connect the fibres in the bonded regions of network. The computational results reveal the influence of the kinematic constraints in the bonds at the sheet-level behavior of the network in addition to the anisotropic response of the network.

With the research undertaken in this thesis, it has been made possible to capture the complex geometry of paper networks adequately, enabling the prediction of their hygro-expansive response. A clear understanding has been achieved on the role of various network parameters in determining the hygro-mechanical behavior of paper. The developed numerical models allowed to gain insight into the hygro-mechanical response of paper fibres and can be further developed to model macro-level properties of paper.

CONTENTS

1	INTRODUCTION	1
1.1	Motivation	2
1.2	Objectives	3
1.3	Structure of thesis	4
2	MODELING FIBROUS NETWORKS: LEVEL SET AND XFEM FORMALISM	5
2.1	Introduction	6
2.2	Fibre network model	8
2.2.1	Fibre Model	8
2.2.2	level-set formalism	10
2.2.3	Random fibre network creation	10
2.3	Modeling methodology	11
2.3.1	XFEM methodology	11
2.3.2	Discretization with the level-set and XFEM formalism (LS-XFEM)	12
2.3.3	Numerical integration scheme	14
2.3.4	Mesh Refinement	14
2.4	Results and discussion	17
2.4.1	Simplified networks	17
2.4.2	Complex networks	20
2.5	Conclusions	26
3	MODELING IRREVERSIBLE STRAINS IN PAPER FIBRES SUBJECTED TO MOISTURE CYCLE	29
3.1	Introduction	30
3.2	Microstructural modeling by kinematic hardening plasticity	33
3.2.1	Random network creation	33
3.2.2	Modeling fibre longitudinal and transverse behavior	33
3.3	Results and discussions	36
3.3.1	Modeling the effects of manufacturing constraints	36
3.3.2	Input parameters for fibres and networks	37
3.3.3	Simplified meso-scale network	38
3.3.4	Complex networks	39
3.4	Conclusions	43
4	MODELING THE EFFECT OF CREEP IN PAPER FIBRES	45
4.1	Introduction	46
4.2	Fibre scale constitutive model	48
4.2.1	Fibre model	48
4.2.2	Implementation aspects	50
4.3	Identification of single fibre parameters from experimental tests	51
4.3.1	Jentzen's creep tests on wetted single fibres	51
4.3.2	Sedlachek's creep recovery and cyclic humidity tests on single fibres	53
4.4	Rate dependent fibre network response	54
4.4.1	Random fibre network generation	56

4.4.2	Hygro-mechanical model	56
4.4.3	Bond constitutive model	57
4.4.4	Moisture cycle simulation on networks	57
4.4.5	Influence of moisture content and coverage on the network relaxation	58
4.5	Conclusions	60
5	EFFECT OF KINEMATIC CONSTRAINTS IN THE BONDED REGIONS AT THE SHEET-SCALE.	63
5.1	Introduction	64
5.2	Hygro-mechanical constitutive model and Numerical discretization	66
5.2.1	Fibre model	66
5.2.2	Bond model	66
5.2.3	Network Model	70
5.2.4	Macroscopic Response	71
5.2.5	Numerical discretization	72
5.3	Results and discussions	74
5.3.1	Simplified two fibre network (A meso-scale model)	74
5.3.2	Complex networks	76
5.3.3	Hygro-expansion	76
5.3.4	Tensile loading	78
5.3.5	Anisotropy	79
5.4	Conclusions	81
6	CONCLUSIONS AND FUTURE WORK	83
6.1	Results and discussion	84
6.2	Future scope	86
6.2.1	Material and modeling aspects	86
6.2.2	Other realms for possible exploration linked with the hygro-mechanical response of paper	86
A	APPENDIX	89
A.1	Derivation of plastic multiplier and consistent tangent operator	89
A.2	Non-linear global equilibrium equations	91
A.3	Derivation of plastic multiplier in the creep model	93
A.4	Derivation of material tangent modulus	94
	BIBLIOGRAPHY	95

LIST OF FIGURES

Figure 1	Illustration of the microstructure of a paper sheet and the role of fibre bonds in hygro-expansion.	6
Figure 2	A model of a fibrous network represented as a periodic unit cell.	7
Figure 3	The local and global coordinate axes.	9
Figure 4	Sign convention used for signed distance function representing the rectangular fibres.	10
Figure 5	Anisotropic orientation function and a random network of fibres.	11
Figure 6	Partitioning of a triangular finite element intersected by the boundaries of two (rectangular fibres) for the area integration. (a) The finite element r_1 is partially covered by two fibres (b) As a first step, fibre 1 is considered. Since the finite element lies partially in the fibre (the level-set values at the vertices are not all of the same sign), it is bisected along the longest edge, resulting in triangles r_{10} and r_{11} . (c) Both of the newly formed triangles r_{10} and r_{11} are again lying partially in fibre 1. They are hence further bisected (d) Triangles r_{100} , r_{101} and r_{110} are further split; r_{111} remains unaffected as it is completely outside the fibre. The partitioning further continues until a certain tolerance is reached.	15
Figure 7	Illustration of the Longest Edge Propagation path (LEPP) refinement in a triangular mesh. (a) The LEPP is given by r_0, r_1, r_2, r_3 with r_3 being the terminal triangle. (b) r_3 is bisected along its longest edge and the new LEPP is r_0, r_1, r_2, r_{31} (c) r_{31} and r_2 , being the terminal triangles, are bisected along their longest edge. The LEPP is r_0, r_1, r_{21} . (d) r_{21} and r_1 are bisected along their longest edge. The LEPP is r_0 and r_1 . (e) r_{11} and r_0 are bisected. This concludes the refinement.	16
Figure 8	(a) A refined mesh. (b) Zoomed view depicting the non-conforming character of the mesh relative to fibre interfaces.	17
Figure 9	A single fibre in a periodic unit cell.	18
Figure 10	Fibre network with a regular mesh non-conforming to the geometry. The σ_{xx} profiles along the cross-sections A-A and B-B are depicted in Fig.13.	19
Figure 11	Stress distributions, σ_{xx}/σ_0 , in horizontal fibre.	19
Figure 12	Stress distributions, σ_{xx}/σ_0 , in the vertical fibre.	20
Figure 13	Stress, σ_{xx}/σ_0 , in cross-sections as defined in figure 10a.	21
Figure 14	Geometry of the complex network and the zoom of mesh used.	22
Figure 15	Deformed network as computed by FEM and LS-XFEM. The displacements have been magnified by a factor of 50.	22
Figure 16	Convergence of the effective hygroscopic coefficients normalized with $\beta_l \Delta \chi$ obtained by the LS-XFEM as a function of the characteristic element size.	23
Figure 17	A high coverage network ($c=1.8$ and $q=0.5$). The displacements have been magnified by a factor of 50.	24

- Figure 18 LS-XFEM solution obtained with refined mesh (48475 nodes, $c=0.9$ and $q=0.5$). 25
- Figure 19 FEM with mesh size $h_5=l/400$ for the network ($c=0.9$ and $q=0.5$). 25
- Figure 20 Normalized strain in the network at cross-sections A–A and B–B unresolved regions. 26
- Figure 21 The discretized network with the finite element triangle at c/s A-A and $x=0.16$ are highlighted. 27
- Figure 22 Fibre segment activation mechanism and Meso-scale network representation. 30
- Figure 23 Experimental results for a hand sheet obtained by Mäkelä [43]. 31
- Figure 24 A periodic random fibrous network of coverage, $c=0.5$ represented by a periodic unit cell. 33
- Figure 25 The local and global coordinate axes. 34
- Figure 26 Schematic diagram of the entire paper making process and subsequent exposure to a wetting-drying cycle. 37
- Figure 27 Normalized local plastic strain (longitudinal component) distribution ${}^p\epsilon_l/(\beta_l\Delta\chi)$, in meso-scale network of coverage, $c=0.5$. 38
- Figure 28 History of the normalized local plastic strain (longitudinal component) in the free standing fibre region of the network and the normalized macroscopic hygro-expansive strain $\epsilon_{xx}/(\beta_l\Delta\chi)$ during the moisture cycle ($\chi_{low} - \chi_{high}$ and vice-versa) for different coverages of the meso-scale network. Note: Curves have been shifted such that $\epsilon_{xx}=0$ corresponds to as-produced sheet in (b) 39
- Figure 29 Normalized local longitudinal plastic strain distribution ${}^p\epsilon_l^f/(\beta_l\Delta\chi)$ in networks with coverage, $c=0.5, 1.0, 2.0$ and 5.0 (left to right) after paper is manufactured. 40
- Figure 30 Normalized local longitudinal plastic strain distribution ${}^p\epsilon_l^f/(\beta_l\Delta\chi)$ in networks with coverage, $c=0.5, 1.0, 2.0$ and 5.0 (left to right) after release of strains. 40
- Figure 31 Normalized macroscopic strains $\epsilon_{xx}/(\beta_l\Delta\chi)$ in the networks subjected to a moisture cycle after manufacturing. 41
- Figure 32 Hygro-expansive strain, ϵ_{xx} normalized with $\beta_l\Delta\chi$ in the fibrous network 1 obtained by numerical model. 41
- Figure 33 Plots of area fractions and irreversible shrinkage for five network realizations of different coverages. 42
- Figure 34 Coefficient of effective hygro-expansion normalized with β_l at the sheet-level for different coverages of complex networks. 42
- Figure 35 The local and global coordinate axes. 49
- Figure 36 Results of Jentzen's experimental tests (overall strain vs time) reproduced from Jentzen [32], and comparison with simulated response. 52
- Figure 37 Results of Sedlachek's experimental creep recovery test (overall strain vs time) reproduced from Sedlachek [64], and comparison with simulated results. 53
- Figure 38 Sedlachek's single fibre cyclic humidity tests (overall strain vs time), reproduced from Sedlachek [64] and comparison with numerical model. 55

Figure 39	A periodic unit cell representing an infinite random network of coverage $c=1.0$. 56	
Figure 40	Macroscopic irreversible strain release during first wetting-drying cycle, normalized with $ \beta_l \Delta\chi$, as a function of the network coverage. 58	
Figure 41	Relaxation of a network of coverage, $c=1.0$ and single fibre at different moisture content. 59	
Figure 42	The stress relaxation response of a network with creep (normalized with the elastic response) at different coverages (4 different realizations of each). 60	
Figure 43	A two fibre meso-scale idealized network subjected to hygroscopic strain. 64	64
Figure 44	The local and global coordinate axes. 67	
Figure 45	Representation of the fibres in 3D by the bond model in 2D. 68	
Figure 46	The mechanism of the bond model interconnecting overlapping fibres. 69	69
Figure 47	Periodic unit cell of a random fibrous network and a simple sparse network. 70	
Figure 48	Interfacial elements at the bonds 71	
Figure 49	A periodic unit cell with three stacked fibres. 72	
Figure 50	(a) A randomly generated fibrous network of paper(top left) (b) Bond region (top right) (c) Interfacial element(bottom center) 73	
Figure 51	A two fibre meso-scale idealized network subjected to hygroscopic strain. 75	75
Figure 52	Random isotropic networks in a periodic unit cell. 76	
Figure 53	Normalized effective hygro-expansivity of the networks averaged in both direction vs the ratio of bond stiffness and shear modulus of fibre. The dashed lines represent the case of fully coupled bonding between fibres. 77	
Figure 54	Strain distribution $\epsilon_{xx}/ \beta_l $ in the network of coverage, $c=1.0$. 77	77
Figure 55	Strain distribution $\epsilon_{xx}/ \beta_l $ in the network of coverage, $c=5.0$. 78	78
Figure 56	Normalized effective stiffness of networks averaged in both direction vs the ratio of the bond stiffness versus the fibre shear modulus. The dashed lines represent the case of fully coupled bonding between fibres. 78	
Figure 57	Probability distribution function for fibre orientations in networks with different anisotropy levels [8]. 79	
Figure 58	Anisotropic response of networks with a varying interfacial element modulus k_l . 80	

LIST OF TABLES

Table 1	Computed stresses and areas obtained by the standard FEM and LS-XFEM. 18	
Table 2	Computed effective hygro-expansive coefficients normalized with β_l for the anisotropic network ($c=0.9$ and $q=0.5$). 23	

Table 3	Computed effective hygro-expansive coefficients normalized with β_l for the isotropic network ($c=0.9$ and $q=0$).	24
---------	--	----

INTRODUCTION

This chapter provides a highlight of previous work in the literature on the modeling of the hygroscopic response of paper fibres and networks. Limitations of existing work are assessed, providing the motivation for the approach adopted here. This is followed by an outline of the objectives of the thesis. In the final section, the structure of the thesis is presented.

1.1 MOTIVATION

At a microscopic level, paper consists of fibres produced from wood pulp. Because of the papermaking process, these fibres have a preferential orientation called the machine direction, [56]. When they are subjected to a change in moisture content e.g. in printing operations, swelling of these fibres occurs which translates in macroscopic expansion which in turn may give rise to curl and buckling. Such dimensional stability issues are to be avoided in industrial applications.

Since this behavior originates at the fibre level, it becomes essential to understand the swelling phenomena of the complex fibrous network at the micro-scale and to assess its influence on the macroscopic response of the network. Some earlier works were devoted to the modeling of fibrous networks, mostly addressing the mechanical response only [12, 36, 63, 66, 67]. There were certain works [9, 36, 72] that involved the modeling of the hygro-expansivity and determining the dimensional stability of paper. They modeled the network using the regular FEM approaches in 2D as well as 3D, thereby becoming computationally expensive. Also, they were not concerned about discretizing the fibre edges at the bonded regions with a higher accuracy in the complex geometry of a paper network. Therefore, there is a need to devise a simple constitutive model in 2D and a numerical method that can model the geometry of complex network of fibres accurately using a regular grid.

Experimental observations made by [43], showed that a permanent macroscopic deformation arises in paper sheets when they are subjected to a moisture cycle after being initially dried under restraint in the papermaking process. This was explained by the fact that the restrained drying induces dried-in strains in the manufactured paper. Upon subsequent exposure to a moisture cycle, e.g. printing operations, these strains get released, causing irreversible deformations. Some works have been conducted to model the micromechanical mechanisms responsible for this property [7]. In addition, some earlier works were carried out to establish a connection between the microstructural network properties and the macroscopic behavior for certain fibrous networks [2, 5, 15, 76, 77]. However, these papers did not address the micro-scale parameters for a complex paper network that govern the sheet-scale hygro-mechanical response when exhibiting irreversible deformations. Hence, a numerical model is required that captures those sheet-scale phenomena, allowing to identify the network properties affecting it in a complex network.

Paper products such as printing paper, corrugated boxes or packaging also suffer deformations due to changes in ambient humidity and applied loading extending over a period of time. It was found through experiments that the time scales play a crucial role in determining the hygro-mechanical response of single paper fibres and paper fibre networks [16, 32, 64]. Alfthan [3] developed and extended the Cox [17] network model by adding hygro-expansion, creep and bonds. Strömbro and Gudmundson [68] captured the experimental results by a theoretical network model they developed. What remains a challenge is to simulate the creep response of the paper network based on constitutive laws formulated at the level of fibres, which are instrumental for acquiring a proper understanding of the microstructural parameters affecting the creep strain rates and irreversible strains at the network level.

In the fibrous network of paper, the fibres interact mechanically via bonded regions. These bonds play a crucial role in the hygro-mechanics of paper because the hygroscopic behavior develops in each fibre and gets transferred across the network through the bonded regions, leading to the

observed macroscopic response. Therefore, the extent of bonding between fibres is of key importance in determining the sheet-level behavior. Literature suggests that there is a scientific scope to explore the role of the inter-fibre stiffness in the sheet-level hygro-expansivity. In the earlier 2D models, a full kinematic coupling is assumed between the fibres which are a part of bond even across the entire thickness of the network [9, 12, 38, 40, 67]. This may well introduce too a strong coupling. One way to avoid this is a full 3D model, but that is expensive. Therefore, we need to study the effect by relaxing the full kinematic coupling and introducing a finite stiffness in the 2D model.

1.2 OBJECTIVES

In order to predict the hygro-mechanical response of paper at the sheet-scale, it is important to establish the relation with the underlying microstructure. Therefore, the central theme of the thesis is to identify the micro-level parameters that determine the macro-level behavior of paper networks under hygroscopic and mechanical loading. This can be achieved by developing a numerical model to represent the microstructure of paper and further study its response to changes in moisture content. However, in order to deal with the geometrical complexity of the fibres in a network, a suitable computational approach is essential that adequately serves the purpose of the anticipated model. This leads to the following questions addressed in the thesis.

Is it possible to model complex fibrous network by capturing the fibre geometry adequately with less computational effort than in conforming finite element discretizations?

As discussed earlier, the occurrence of irreversible strains upon a wetting cycle after papermaking is one of the causes of the dimensional instabilities in paper. A suitable fine-scale mechanism can be invoked to explain such phenomena. Here, the aim is to understand the parameters at the fibre scale that govern this behavior at the sheet-scale. This gives rise to the second set of questions posed in the thesis.

How to model the mechanism of sheet-scale irreversibility based on the fibre level in a network? Which microstructural properties of the network determine primarily the irreversibility observed at macro-scale?

Moreover, the time scales have a considerable influence on the overall sheet-level response of paper fibres subjected to humidity changes. In order to understand this influence, a micro mechanical model needs to be developed that predicts this behavior. Therefore, the third research question reads:

How to incorporate the time dependency in the model in accordance with experimental results? Can it be further applied to study the various fine-scale parameters in a network that govern the rate effects of a paper network?

In the models developed so far the inter-fibre bonds of the network are assumed to be completely rigid in the considered 2D network idealizations. However, the fibres in bonds may undergo independent displacements in reality, which affects the macroscopic deformation and anisotropic response. Therefore, the assumptions on the kinematic constraints in the bonds needs to be relaxed. This entails the final research theme:

What micromechanical model needs to be adopted for relaxation of kinematic constraints in inter-fibre bonds? How does it affect the macro-scale deformation of networks of different coverages?

Several difficulties have been encountered in the past for identifying the causes of hygro-mechanical behavior of paper fibres. However, in the present work, attempts have been made to mitigate these difficulties and analyze the hygro-mechanical response of networks with these outlined objectives.

1.3 STRUCTURE OF THESIS

The core of this thesis consists of 4 chapters explaining in detail the methods adopted to reach the objectives, leading to the concluding chapter in this thesis.

Chapter 2: This chapter presents a novel level-set based XFEM formalism applied to a fibrous network. It discusses the efficiency of level-set functions in capturing complex fibre and bond boundaries and of XFEM in modeling the strong geometrical discontinuities within the network. Finally, simulation results are presented, which measure the performance of the adopted method.

Chapter 3: The irreversible strains at the sheet-level as observed in experiments involving a wetting-drying cycle after papermaking are modeled in this chapter. A suitable mechanism responsible for this behavior is discussed. It involves the implementation of a rate-independent kinematic hardening plasticity model with a moisture dependent yield stress. It is implemented at the fibre level in order to investigate its effect at the macro-scale of the network. The findings obtained in the simulations give adequate insights in the dependence of the irreversible strain on the network properties.

Chapter 4: This chapter discusses the time-dependent behavior of paper. A suitable rate-dependent model is adopted at the fibre level for this purpose. It highlights the results of this rate-dependent model identified on the basis of existing experimental results on single fibres. Finally, these identified parameters are used in the network model to compute its response under an applied strain and changes in humidity.

Chapter 5: The assumption of a perfect kinematic bonding in the inter-fibre bonds is relaxed by allowing the fibre midplanes to exhibit relative displacements. For this purpose, an interfacial element is used in each of the bonded regions of the fibrous network. The overall response of the network is studied for a varying bond stiffness between fibres in inter-fibre bonds when subjected to moisture changes and tensile loading. Also, the role of these kinematic constraints between fibres in the bonds on the anisotropy of the network is analyzed.

Chapter 6: The final chapter presents the major findings of the work reported in this thesis. It highlights the assumptions used in the adopted approaches and the results achieved. Additionally, other interesting areas of research are also suggested.

LEVEL-SET BASED EXTENDED FINITE ELEMENT MODELING OF THE RESPONSE OF FIBROUS NETWORKS UNDER HYGROSCOPIC SWELLING

Materials like paper, consisting of a network of natural fibres, exposed to variations in moisture, undergo changes in geometrical and mechanical properties. This behavior is particularly important for understanding the hygro-mechanical response of sheets of paper in applications like digital printing. A two-dimensional microstructural model of a fibrous network is therefore developed to upscale the hygro-expansion of individual fibres, through their interaction, to the resulting overall expansion of the network. The fibres are modeled with rectangular shapes and are assumed to be perfectly bonded where they overlap. For realistic networks the number of bonds is large and the network is geometrically so complex that discretizing it by conventional, geometry-conforming, finite elements is cumbersome. The combination of a level-set and XFEM formalism enables the use of regular, structured grids in order to model the complex microstructural geometry. In this approach, the fibres are described implicitly by a level-set function. In order to represent the fibre boundaries in the fibrous network, an XFEM discretization is used together with a Heaviside enrichment function. Numerical results demonstrate that the proposed approach successfully captures the hygro-expansive properties of the network with fewer degrees of freedom compared to classical FEM, preserving desired accuracy.

Keywords: Fibrous network, hygro-expansion, Level-set functions, XFEM

2 This chapter is based on: P. Samantray, R.H.J. Peerlings, E. Bosco, M.G.D. Geers, T.J. Massart, O. Rokos, 2019. *Level set based eXtended finite element modeling of the response of fibrous networks under hygroscopic swelling*. In preparation.

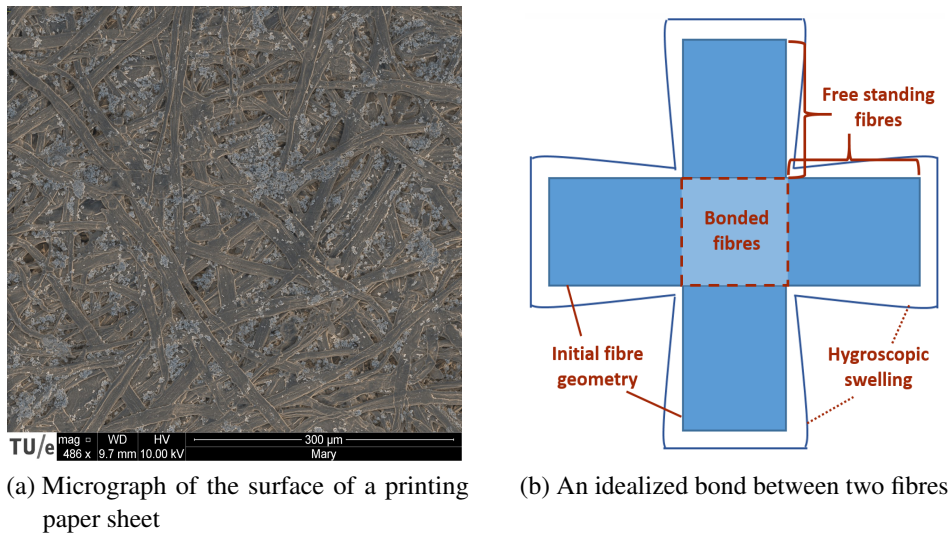


Figure 1: Illustration of the microstructure of a paper sheet and the role of fibre bonds in hygro-expansion.

2.1 INTRODUCTION

At the micro-scale, a paper sheet consists of a network of fibres that is produced from wood pulp as shown in Fig. 1a. The paper fibres have a preferential orientation (machine direction) due to the manufacturing process, which results in the observed anisotropic behavior [56]. In the network, fibres are bonded with each other in certain regions and free standing elsewhere. Upon exposure of a sheet of paper to a humid environment or liquid water, moisture-induced swelling takes place, which is called hygro-expansion [37].

In practical applications related to printing, this results in macro-scale effects such as curling, waviness and cockling. At the microstructural level, the changes in each individual fibre due to the variation in moisture content are transmitted to the neighboring fibres by the bonds in the fibrous network as sketched in Fig. 1b. These changes include geometrical variations of the shape in each fibre and the accompanying stress concentrations induced by the bonded areas. Understanding these phenomena and their dependence on the properties of the individual fibres and the network geometry is essential for predictive modeling of sheet-scale phenomena in paper as well as other networks of natural fibres.

Gaining insight in the behavior of a fibrous network subjected to hygroscopic swelling is essential to unravel the influence of different properties of the fibres and network on the overall hygro-expansive response. Among the early attempts to model the mechanical response of paper, Cox [17] studied the effect of orientation of fibres on stiffness and strength of paper by assuming that fibres carry only axial forces. The flexural stiffness of the fibres was also taken into account [1]. The deformation of bonds and the elasto-plastic behavior of fibres was also studied [53]. Assuming constant strain, the transverse properties of fibres were included [63]. Later, a model incorporating shear forces, axial and bending and torsional moments between rigid bonds was developed for a network of fibres [67]. Inter-fibre bonding was also considered in modeling the fibrous network [12]. Some of the recently developed numerical models for fibrous networks mostly modeled the fibrous

material with two dimensional assumptions considering the individual fibres as trusses or beams with only isotropic properties [20, 36, 66]. Most of these works were carried out for the description of the mechanical behavior of the fibrous network, without any coupling to the hygroscopic response.

Several other studies addressed the hygro-expansivity and dimensional stability of paper. Some studies focused on the hygro-expansion in order to understand the factors affecting it [47, 59, 72] which included shrinkage during drying, effect of fibre curl and bonding between the fibres . Also, studies on the dimensional stability of paper at the macro-scale were carried out [8, 21, 37, 45, 46, 49, 71] which included studies on shrinkage as a function of the beating of the pulp, characterization of hygroexpansion in MD and CD, hygroexpansivity of fibres, effect of interaction of paper with surrounding air on the strain rates, established correlation between drying shrinkage and dimensional stability, relation between drying shrinkage and hygro-expansion coefficient and finally a meso-scale model to predict hygro-expansive response respectively . Several other works were done on studying the hygro-expansion of paper fibres. However, most of these studies lack in modeling the hygro-mechanical behavior of complex fibrous networks like paper subjected to moisture fields.

The aim of the present study is to model the hygro-mechanical behavior of fibrous materials through a multi-scale analysis of the network using periodic homogenization [10, 22, 52]. The fibres are modelled as two dimensional ribbon like elements in a network subjected to hygro-expansion, for which a finite element framework was used in [9]. This study used a regular grid of triangular finite elements to model the network which inevitably is not aligned with most of fibres. However, the use of such non-conforming finite elements does not allow to accurately capture the geometry of the fibres and of the voids and bonded regions between them. Non-conforming FEM considers any fibre lying inside the centroid of a finite element to contribute to its stiffness. This leads to a geometrical representation of a fibre in the network with jagged boundaries. To better resolve the fibre boundaries, a very fine discretization was therefore employed in [9], which increases the computational effort. Note that, in a two dimensional microstructure with overlapping fibres at the bonds, a mesh conforming to the different fibre geometries present in the same bonded regions is difficult to generate. This may result in a very fine mesh which will result in high computational effort required for the subsequent simulations. In complex networks as shown in Fig. 2 (a paper network represented as ribbon shaped rectangular fibres), it will be difficult to generate a conforming mesh as shown in the magnified view for all fibres in the densely bonded regions . There is thus a need to

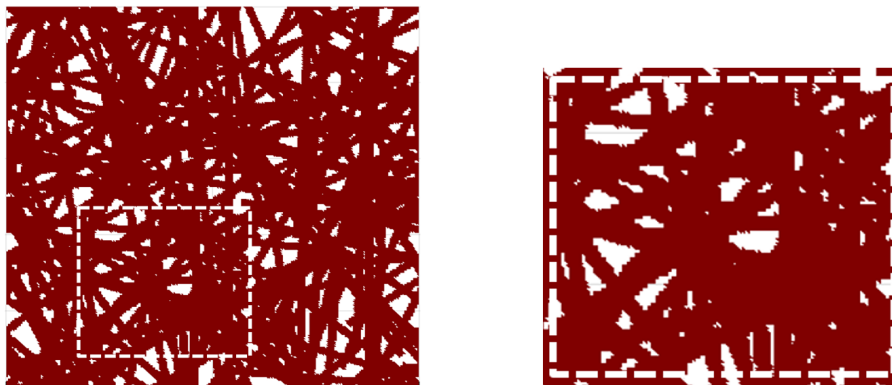


Figure 2: A model of a fibrous network represented as a periodic unit cell.

develop models that capture the fibre boundaries with a better accuracy and less computational effort.

Here, an advanced discretization scheme is combined with the hygro-mechanical model developed by [9] to enable modeling of larger systems in two-dimensional configurations, with the potential to be extended towards three dimensions. The level-set formalism is used in combination with the Extended Finite Element Method (XFEM) to capture the geometrical complexity of the network - here in two dimensions. The level-set methodology is a mathematical tool to describe boundaries (or, more generally, geometry) implicitly (Sethian [65]). The boundary of a fibre is represented by the zero level-set of a higher dimensional function. This results in a versatile geometrical description that is de-coupled from the spatial discretization. XFEM [18] allows to account for the effect of interfaces (boundaries of fibres) on the mechanical behavior of the problem. In the bonded regions, the interpolation functions classically used in the elements are modified by discontinuous enrichment functions, so that geometrical discontinuities associated with the fibre interfaces can be resolved. This allows to capture the fibre's boundaries in the bonded regions accurately using reasonably coarse meshes by coupling of the level-set functions with the XFEM enrichment.

This chapter is organized as follows: In section 2, the geometry of the fibre network model is discussed briefly, along with the level-set formalism used to represent it. In section 3, the XFEM discretization used for the fibrous network is described, together with the required specific numerical integration scheme to accommodate it. Section 4 presents the simulation results of the hygro-mechanical behavior of paper using the XFEM enrichment, first for the simplified models presented in [8], and subsequently for more complex networks with different coverages. The local and global responses are analyzed for complex networks. Finally, section 5 reports the conclusions and perspectives.

Throughout this contribution, the following notations are used for operations on the Cartesian tensors. Scalars, vectors and tensors are denoted by a , \vec{a} and \mathbf{A} respectively. The 4th order tensors are represented by ${}^4\mathbf{A}$. For tensor and vector operations, the following equivalent notations are used with Einstein's summation convention on indices: $\mathbf{A}:\mathbf{B}=A_{ij}B_{ji}$ with ($i = x,y,z$ for the global reference system and $i = 1,t,z$ for the local reference system). The Voigt notation used to represent tensors and tensor operations in a matrix format is depicted as follows: \underline{a} and $\underline{\underline{A}}$ denote a column matrix and a matrix of scalars respectively. The matrix multiplication is denoted as $(\underline{\underline{A}} \underline{a} = A_{ij}a_j)$.

2.2 FIBRE NETWORK MODEL

2.2.1 Fibre Model

The fibre level constitutive model formulated in [8] is adopted here. A two dimensional plane stress model is assumed. The fibres in consideration are oriented in the (x,y) plane of the (x,y,z) global reference frame, and subjected to a uniform moisture change. The moisture content χ is defined as the ratio of the weight of the moisture in paper to the total weight of the paper. For the fibre constitutive model, a local reference frame (1,t,z) is considered along the directions of the fibre as shown in the Fig. 3. The hygro-mechanical properties of the paper fibres are assumed to be transversely isotropic with respect to their longitudinal axis. The general elastic constitutive law

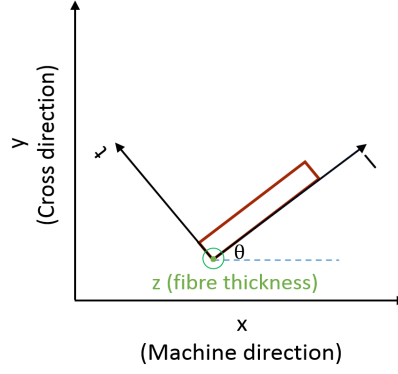


Figure 3: The local and global coordinate axes.

for a fibre, assuming plane stress state in the z -direction, and subjected to a moisture change $\Delta\chi$ is expressed as

$$\sigma^f = {}^4D^f : (\epsilon^f - {}^h\epsilon^f) \quad (1)$$

where the hygroscopic strain ${}^h\epsilon^f$ is given by

$${}^h\epsilon^f = \beta^f \Delta\chi \quad (2)$$

In these expression, ${}^4D^f$, ϵ^f and β^f are the elastic constitutive tensor, the strain tensor and the hygro-expansivity tensor of the fibre respectively. In matrix notation, ${}^4D^f$ and β^f are represented as

$$\underline{D}^f = \begin{pmatrix} \frac{E_l}{(1-\nu_{lt}\nu_{tl})} & \frac{E_l\nu_{tl}}{(1-\nu_{lt}\nu_{tl})} & 0 \\ \frac{E_t\nu_{lt}}{(1-\nu_{lt}\nu_{tl})} & \frac{E_t}{(1-\nu_{lt}\nu_{tl})} & 0 \\ 0 & 0 & G_{lt} \end{pmatrix}, \underline{\beta}^f = \begin{pmatrix} \beta_l \\ \beta_t \\ 0 \end{pmatrix} \quad (3)$$

In Eq. (3), E_l and E_t denote the elastic moduli in the longitudinal and transverse direction with respect to the fibre axis, G_{lt} is the in-plane shear modulus, ν_{lt} and ν_{tl} the in-plane Poisson ratios. The coefficients of hygroscopic expansion, β_l , β_t , are different in the longitudinal and transverse directions of the fibre. It was observed by Bosco, Peerlings, and Geers [8] that the value of the Poisson's ratio has a minor effect on the effective hygro-expansivity of the network. All the material parameters are assumed to be independent of the moisture content χ . In this study, the main objective being the analysis of the performance of the LS-XFEM formalism, the material properties were kept constant. Also, this serves the purpose of having a simplified description of the material.

The local reference system of a fibre m is oriented at an angle $\theta^{(m)}$ with respect to the global reference system (x,y,z) . Therefore, the relationships (Eq. (1)-Eq. (3)) need to be transformed from the local (fibre) frame to the global frame of the paper material for each fibre in the network (Roylance [55]).

The fibre bonds are important because of their influence on the overall behavior of the network. In the 2D modeling, the fibres are assumed to be perfectly bonded to simulate the interplay between hygro-expansion and elasticity of the fibres. This implies full displacement strain compatibility inside a bond for all the fibres interconnected in that bond.

2.2.2 level-set formalism

The level-set formalism [48, 65] is here used to describe the geometry of fibres. In this method, the fibres is described as the zero level-set of a higher dimensional level-set function $\phi(\vec{x})$ (see Fig. 4) . In most cases, including the current , the level-set function gives the signed distance of a point \vec{x} to

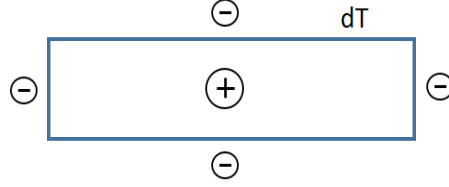


Figure 4: Sign convention used for signed distance function representing the rectangular fibres.

the interface of the rectangular fibre defined by dT in Fig. 4. The level-set function $\phi(\vec{x})$ is defined as

$$\phi(\vec{x}) = \pm \min_{\vec{x}_T \in dT} |\vec{x} - \vec{x}_T| \quad (4)$$

where the sign is negative if \vec{x} is outside and positive if it is inside the contour defined by dT .

2.2.3 Random fibre network creation

In order to understand the hygroscopic behavior of a complex network of fibres, a set of rectangular fibres having a length l_f and width $w_f = \frac{l_f}{10}$ is randomly generated in a unit cell of length $l = 5l_f/3$. The length of the periodic unit cell is $1500 \mu\text{m}$. Each of the fibres is generated with random coordinates for its centroid $[x,y] \in [0,l]$ as shown in fig. 5b. Fibre parts which extend beyond the boundary of the unit cell are periodically copied into the cell at the opposite edge. Now, depending on the number of fibres n generated in the unit cell, a coverage c is defined as the ratio of the total area occupied by all fibres and the area of unit cell. It is related to the grammage g via

$$g = c\rho_f t$$

where ρ_f is the density of fibres and t is the thickness of the fibres.

For example, considering a density of the fibres of $\rho_f = 1500 \text{kg/m}^3$ ([45]), a thickness $10 \mu\text{m}$ and a coverage of 0.9 as used in the results of section 2.4.2, the corresponding grammage is 13.5g/m^2 . As the coverage increases, with density and thickness remaining constant, the grammage scales linearly with the coverage. The orientations of the randomly generated fibres in the network satisfy a probability density function based on reference [17]:

$$f(\theta) = \frac{1}{\pi} \frac{1 - q^2}{1 + q^2 - 2q \cos(2\theta)} \quad (5)$$

where θ is the angle between the fibre and the machine direction, with $-\pi/2 < \theta < \pi/2$. Fig. 5a shows the probability density function for the orientation for two values of the anisotropy parameter q : for the isotropic case $q=0$ and an arbitrary degree of anisotropy $q=0.51$ [8].

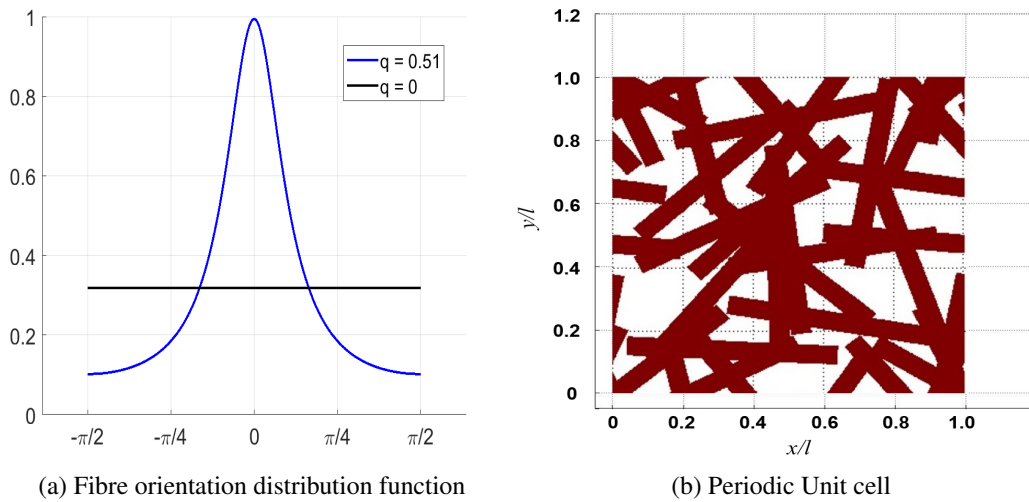


Figure 5: Anisotropic orientation function and a random network of fibres.

Once the fibres are generated and each of them is assigned a level-set function ($\phi_1(\vec{x})$, $\phi_2(\vec{x})$, $\phi_3(\vec{x})$, ..., $\phi_n(\vec{x})$), a periodicity condition is enforced on the unit cell. The level-set function that allows identifying the fibres and voids for the network, can be described as

$$\psi(\vec{x}) = \max(\phi_1(\vec{x}), \phi_2(\vec{x}), \phi_3(\vec{x}), \dots, \phi_n(\vec{x})) \quad (6)$$

where $\psi(\vec{x}) > 0$ in fibres and $\psi(\vec{x}) < 0$ in voids.

Here, we have assumed the same size for all the fibres, which renders the microstructure idealized in nature. The reason for the adoption of identical shape and size of fibres throughout the thesis is to understand the trends and qualitative relationships between the microstructural parameters and the effective hygroexpansivity of the network. With these simplifications, the relationships are better understood from the observed trends. In the current chapter, we are interested in assessing the numerical efficiency of a discretization scheme by comparison with standard FEM for some networks only, which is least affected by the choice of the geometrical parameters. The use of a plane stress assumption is justified due to a negligible thickness of the paper compared to its in-plane dimensions. One of the main advantages of the 2D framework is the reduced computational expense in obtaining the hygro-mechanical behaviour of the network compared with a full 3D model. Moreover, it is relatively straight forward to produce the microstructure and to mesh it. Also, the out of plane deformations and stresses are ignored. Finally, the assumption of full kinematic constraint between fibres in the bond in the current chapter has consequences on the overall behaviour of the network. This will be further relaxed in the final chapter of the thesis.

2.3 MODELING METHODOLOGY

2.3.1 XFEM methodology

The extended finite element method (XFEM) is a numerical discretization method developed to model material discontinuities, singularities and moving boundaries independently of the underlying finite element mesh. With the microstructures considered in this work, it is not feasible to produce a geometry conforming mesh for the free standing parts of fibres and even more in the

bonded regions where fibres partially overlap. Accurate local results cannot be obtained by the conventional finite element method (FEM) if the mesh does not conform to the boundaries of the fibres. XFEM can be used instead to capture the fibre boundaries both in free standing and bonded regions accurately even with a regular non-conforming mesh. In terms of accuracy, an adequate solution can be obtained by enriching the classical shape functions with special functions capturing the geometrical discontinuities in XFEM.

Depending on the nature of problem under consideration, a suitable enrichment function needs to be adopted in XFEM. To model the geometrical discontinuity between solid (fibres) and voids in a fibrous network with a regular mesh, a Heaviside function defined in terms of the level-set function ϕ is adopted (Sukumar, Chopp, Moes, and Belytschko [69]) as an enrichment function, since the geometry is already described by the level-set functions ϕ_i . The displacement interpolation on the solid domain reads

$$\vec{u}(\vec{x}) = \sum N_i(\vec{x}) \vec{u}_i H(\psi(\vec{x})) \quad (7)$$

in which, $H(\psi(\vec{x})) = 1$ for $\psi(\vec{x}) > 0$ inside fibres and $H(\psi(\vec{x})) = 0$ for $\psi(\vec{x}) \leq 0$ (inside void regions).

The interconnection between XFEM (to model discontinuities) and level-set (to capture the geometry) is achieved in the LS-XFEM approach which is discussed in detail in the next section. Therefore, a LS-XFEM formalism that makes use of the level-set information in this particular XFEM setting greatly simplifies the set up of the model under consideration.

2.3.2 Discretization with the level-set and XFEM formalism (LS-XFEM)

In the current thesis, the behavior of the fibres is assumed elastic and small strains and displacements are considered. The total potential energy in the unit cell consisting of network of fibres is given by

$$\pi = \frac{1}{2} \int_V \sum_{i=1}^n H(\phi_i(\vec{x})) (\underline{\epsilon}^f - {}^h \underline{\epsilon}_i^f) : \underline{D}_i^f : (\underline{\epsilon}^f - {}^h \underline{\epsilon}_i^f) t_i dA \quad (8)$$

where, n is the total number of fibres occupying the periodic cell area A , $\phi_i(\vec{x})$ is the signed distance function of the i^{th} fibre, $\underline{\epsilon}$ the strain tensor associated with Eq. (7), ${}^h \underline{\epsilon}_i^f$ the hygroscopic strain in fibre i and t_i its thickness. This expression may be written in matrix format as .

$$\begin{aligned} \pi &= \int_V \sum_{i=1}^n H(\phi_i(\vec{x})) \frac{1}{2} (\underline{\epsilon}^f - {}^h \underline{\epsilon}_i^f)^T \underline{D}_i^f (\underline{\epsilon}^f - {}^h \underline{\epsilon}_i^f) dV \\ &= \int_V \sum_{i=1}^n H(\phi_i(\vec{x})) \frac{1}{2} \left[(\underline{\epsilon}^f)^T \underline{D}_i^f \underline{\epsilon}^f - 2(\underline{\epsilon}^f)^T \underline{D}_i^f {}^h \underline{\epsilon}_i^f + ({}^h \underline{\epsilon}_i^f)^T \underline{D}_i^f {}^h \underline{\epsilon}_i^f \right] dV \end{aligned} \quad (9)$$

in which \underline{D}_i^f and ${}^h \underline{\epsilon}_i^f$ are the transformed elastic constitutive matrix and hygroscopic strain matrix, respectively, transformed to the global frame, for a particular fibre i aligned at an angle θ_i with respect to the global frame as discussed earlier.

Using the strain-displacement relationship for each finite element, $\underline{\epsilon}^f = \underline{B}_e \underline{u}_e$, where \underline{B}_e is the strain-displacement matrix and \underline{u}_e is the nodal displacement column of the finite element e , the

integration over the entire network of fibres in Eq (9) is carried out element wise. Swapping the summations over all m finite elements with areas A_e and the n fibres, the assembled potential energy is obtained as

$$\pi = \frac{1}{2} \sum_{e=1}^m \left[\underline{u}_e^T \int_{A_e} \sum_{i=1}^n H(\phi_i(\vec{x})) (\underline{B}_e^T \underline{D}_i^f \underline{B}_e) t_i dA \underline{u}_e - 2 \int_{A_e} \underline{u}_e^T \sum_{i=1}^n H(\phi_i(\vec{x})) (\underline{B}_e^T \underline{D}_i^f h \underline{\epsilon}_i^f) t_i dA + \int_{A_e} \sum_{i=1}^n H(\phi_i(\vec{x})) h \underline{\epsilon}_i^f \underline{D}_i^f h \underline{\epsilon}_i^f t_i dA \right] \quad (10)$$

Of all the possible displacements that satisfy the boundary conditions of an elastic structural system, the ones corresponding to the equilibrium configuration minimize the total potential energy, i.e.

$$\frac{\partial \pi}{\partial \underline{u}} = \underline{0}$$

or, using Eq.(10),

$$\sum_{e=1}^m \sum_{i=1}^n \int_{A_e} H(\phi_i(\vec{x})) \underline{B}_e^T \underline{D}_i^f \underline{B}_e t_i dA \underline{u}_e - \sum_{e=1}^m \sum_{i=1}^n \int_{A_e} H(\phi_i(\vec{x})) \underline{B}_e^T \underline{D}_i^f h \underline{\epsilon}_i^f t_i dA = \underline{0}$$

This equation is of the form of a linear system

$$\underline{K} \underline{u} - \underline{f} = \underline{0} \quad (11)$$

in which, \underline{u} collects all nodal displacements and stiffness matrix and the hygroscopic load vector are given by

$$\underline{K} = \sum_{e=1}^m \sum_{i=1}^n \int_{A_e} H(\phi_i(\vec{x})) \underline{B}_e^T \underline{D}_i^f \underline{B}_e t_i dA \quad (12)$$

$$\underline{f} = \sum_{e=1}^m \sum_{i=1}^n \int_{A_e} H(\phi_i(\vec{x})) \underline{B}_e^T \underline{D}_i^f h \underline{\epsilon}_i^f t_i dA \quad (13)$$

Linear triangular finite elements are used for the discretization. It is straight forward to implement such a formulation of linear triangular FE. Also, it is convenient to have constant strain within each element for the purpose of computing the respective fibre contributions to an element - see the next section. Finally, mesh of triangular elements can be easily adapted to represent a complex geometry. Three cases can be distinguished for mapping fibres onto a finite element. First, if the finite element lies entirely in a void, the Heaviside function in Eqs. (12) – (13) vanishes and the element does not contribute to the stiffness matrix and hygroscopic load vector. If the finite element lies entirely in one or more fibres, its full contribution is accounted for in the computation of the stiffness matrix and hygroscopic load vector. Finally, if the finite element is intersected by fibre boundaries, a specific integration technique needs to be used, as described next.

2.3.3 Numerical integration scheme

In this section, the integration scheme used for elements intersected by fibre boundaries is detailed. The integration over a particular finite element for all fibres passing in it is considered for the stiffness and force vector for an element in the Eqs. (14) and (15) respectively.

$$\underline{K}_e = \sum_{i=1}^n \underline{B}_e^T \underline{D}_i^f \underline{B}_e \int_{A_e} H(\phi_i(\vec{x})) t_i dA \quad (14)$$

$$\underline{f}_e = \sum_{i=1}^n \underline{B}_e^T \underline{D}_i^f h_{\underline{\epsilon}_i}^f \int_{A_e} H(\phi_i(\vec{x})) t_i dA \quad (15)$$

In the computation of the contribution of each fibre to the finite element, it is therefore only required to determine the area occupied by each fibre, i.e. A_1, \dots, A_n in this particular element, where $A_i = \int_{A_e} H(\phi_i(\vec{x})) dA$. The algorithm used to compute this area of each fibre in the finite element is illustrated by considering two fibres lying in the region occupied by a triangular element with vertices (A, B, C) as shown in Fig. 6.

Using the level-set function for a particular fibre i , if one of the vertices of the finite element triangle is identified to lie inside the fibre, then the element is considered to lie in the fibre. Therefore, the triangle is sub-divided along its longest edge. The sub-triangulation continues and stops only when a tolerance is met in terms of the smallest triangle area. This procedure is executed for all fibres lying partially inside the finite element.

The integration scheme can be summarized as follows:

Step 1: Check for first fibre if all element vertices lie in it (i.e. $\phi_1(A) > 0, \phi_1(B) > 0, \phi_1(C) > 0$). If the particular fibre lies partially in the element, then it is split into two new triangles as shown in Fig. 6.

Step 2: The subdivision continues for triangles intersected by the fibre's boundaries. If a triangle lies completely inside or outside the fibre, the subdivision is not performed.

Step 3: The sub-triangulation is terminated when a specified tolerance limit is achieved. In the examples below, we terminate it when the area of sub-triangulated element is one-hundredth the area of the coarsest finite element.

Step 4: After the termination of the sub-triangulation, the area occupied by the fibre in the finite element is determined as the sum of the areas of triangles lying completely in the fibre and the ones the centroid of which lies inside the fibre. Thereafter, the above steps are repeated for the next fibre.

2.3.4 Mesh Refinement

Considering a unit cell consisting of a network of fibres with complex topology, a coarse triangulation is naturally insufficient for an accurate description of the interfaces. Using a globally fine triangulation would however dramatically increase the computational cost. Therefore, a refinement strategy based on the backward longest edge bisection algorithm [54] is adopted here for elements intersected by boundaries. This approach preserves adequate accuracy at a lower cost, still allowing for large triangles in regions with little strain fluctuation within fibres and voids. This mesh refinement should not be confused with the sub-triangulation discussed in the previous section. The sub-triangulation is used to accurately capture the geometry, i.e. the volume of an element occupied by a particular fibre. Mesh refinement, on the other hand, improves the accuracy of the kinematics of the problem.

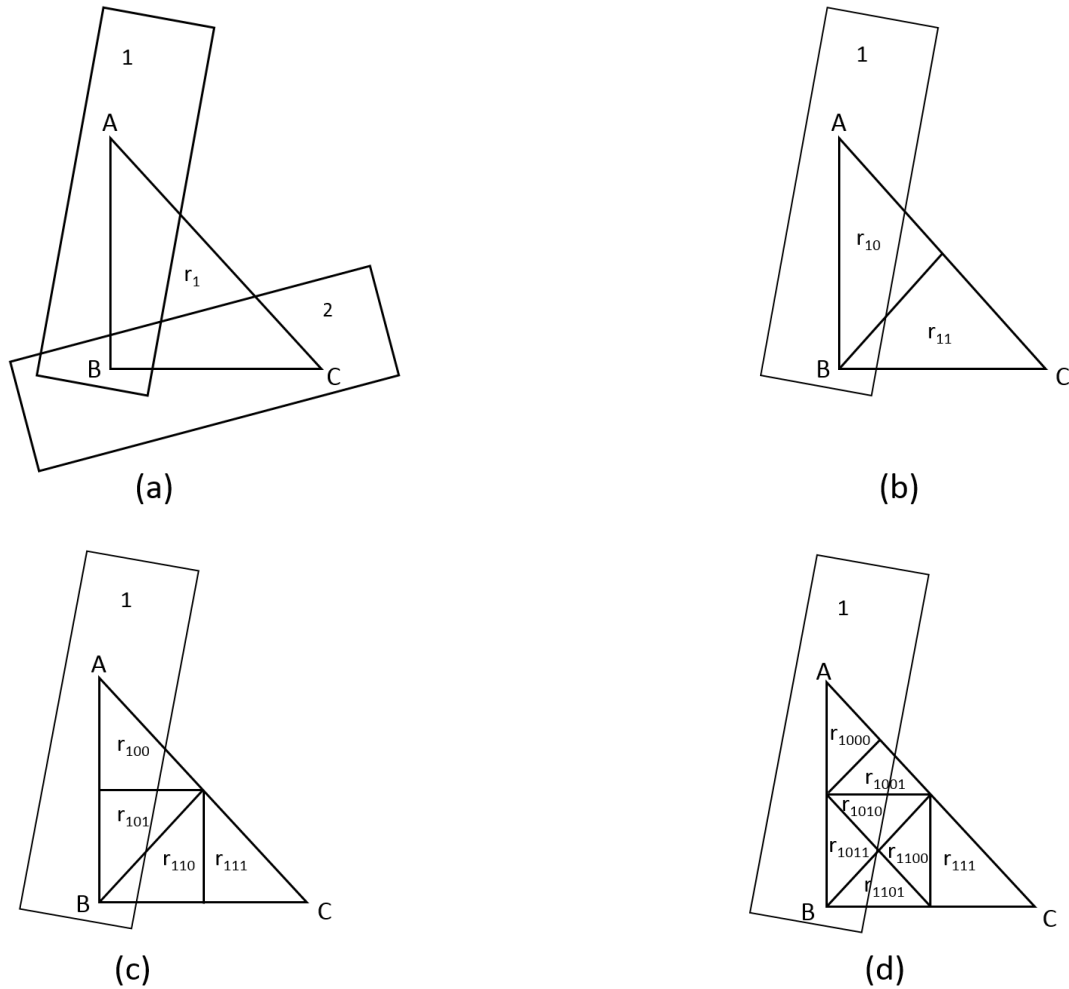


Figure 6: Partitioning of a triangular finite element intersected by the boundaries of two (rectangular fibres) for the area integration. (a) The finite element r_1 is partially covered by two fibres (b) As a first step, fibre 1 is considered. Since the finite element lies partially in the fibre (the level-set values at the vertices are not all of the same sign), it is bisected along the longest edge, resulting in triangles r_{10} and r_{11} . (c) Both of the newly formed triangles r_{10} and r_{11} are again lying partially in fibre 1. They are hence further bisected (d) Triangles r_{100} , r_{101} and r_{110} are further split; r_{111} remains unaffected as it is completely outside the fibre. The partitioning further continues until a certain tolerance is reached.

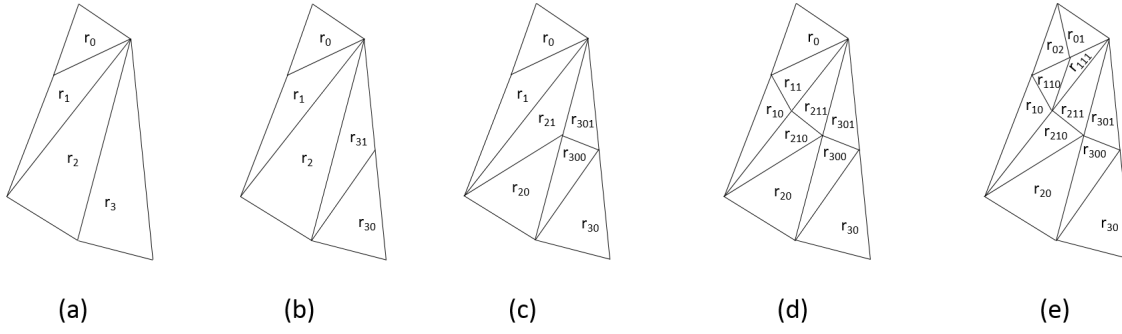


Figure 7: Illustration of the Longest Edge Propagation path (LEPP) refinement in a triangular mesh. (a) The LEPP is given by r_0, r_1, r_2, r_3 with r_3 being the terminal triangle. (b) r_3 is bisected along its longest edge and the new LEPP is r_0, r_1, r_2, r_{31} (c) r_{31} and r_2 , being the terminal triangles, are bisected along their longest edge. The LEPP is r_0, r_1, r_{21} . (d) r_{21} and r_1 are bisected along their longest edge. The LEPP is r_0 and r_1 . (e) r_{11} and r_0 are bisected. This concludes the refinement.

After the generation of the geometry of a network of fibres, the finite elements located at the boundaries of the fibres are revisited for mesh refinement. For each such element, the corresponding fibre signed distance functions are evaluated at all of its vertices of considered triangular finite element. When all three vertices are contained inside all fibres passing through it, or when none of them belong to the fibres, the element is not categorized as a boundary element. In all other cases, the element is identified as boundary element to be refined, for which a mesh refinement algorithm is applied.

As defined by [54], for a triangle r_0 of any triangulation T , the longest edge propagation path (LEPP) is an ordered list of triangles $r_0, r_1, r_2, \dots, r_n$ such that r_i is neighbor to r_{i-1} along its longest edge. The (LEPP) terminates with a) one triangle with its longest edge along the external boundary of the mesh, or b) a pair of triangles sharing the same longest edge. Now, based on the LEPP of triangle r_0 marked for refinement, a backward longest edge refinement algorithm is used in which the longest edge of r_n is bisected in the former case and both triangles r_{n-1} and r_n are bisected along longest edge for the later case. The LEPP is updated and the procedure is repeated until the initial triangle r_0 is bisected as well. In Fig. 7, the longest edge bisection algorithm is illustrated for a simple triangulation. In the current thesis, the elements at the interfaces between a free standing fibre segment and void, as well as at the boundaries of bonds are refined. The newly generated refined triangular elements at these locations also better capture multiple fibres passing through the finite elements. Therefore, the accuracy of the mesh improves in representing the fibre geometry and, more importantly, its kinematics in these complex networks. In addition, the boundary edges of the unit which is periodic in nature are also refined to maintain periodicity of the nodes.

However, the refined mesh, as seen in Fig. 8 will not be conforming to the fibre boundaries. As mentioned earlier, the high number of fibre interfaces particularly in the bonds, would render it difficult to capture with a conforming mesh at cheaper computational effort. This again emphasizes the motivation to use the proposed LS-XFEM formalism, which allows to decouple the mesh and fibre boundaries with a structured mesh that still captures the fibre edges adequately.

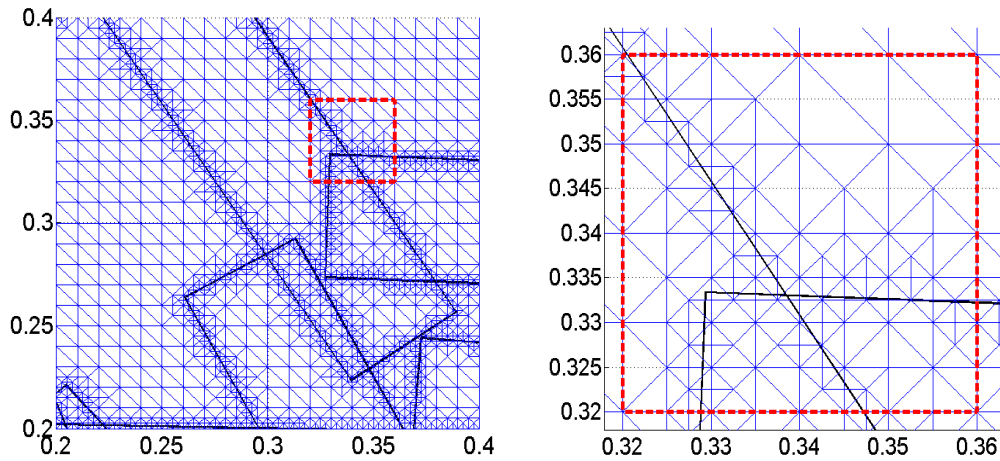


Figure 8: (a) A refined mesh. (b) Zoomed view depicting the non-conforming character of the mesh relative to fibre interfaces.

2.4 RESULTS AND DISCUSSION

To demonstrate the benefits of the LS-XFEM formalism for fibrous networks, simplified illustrations are first presented below. Subsequently, the formalism is used for a complex network to study the effect of microstructural features on the sheet-scale properties due to moisture infiltration.

2.4.1 Simplified networks

First, the stress level in a single family of parallel fibres subjected to a tensile load is assessed, followed by the study of the stress concentrations in the bond regions of an elementary network consisting of two families of fibres subjected to a macroscopic tensile load.

2.4.1.1 Parallel fibres subjected to uniaxial tension

In this problem, an infinite number of parallel, equispaced, infinitely long fibres is considered, as shown in Fig. 9b. The fibres are subjected to a horizontal stress, σ_0 . Using a square periodic unit cell of length l for this simple geometry, half of a fibre occurs at the top and the another half at the bottom of the cell, see Fig 9a. The chief reason to use this unit cell in the example because there are regions with fibre and voids which is also the case in the complex fibrous network considered later. Also, in the discretized unit cell, the mesh in this case is non-conforming and this is mainly for the purpose of illustrations of the benefit of the LS-XFEM formalism as compared to the standard FEM. The input parameters for the anisotropic fibres are an elastic modulus in longitudinal direction, E_l , and in transverse direction, $E_t = E_l/4$, shear modulus, $G_{lt} = 0.1E_l$, Poisson ratios $\nu_{lt} = 0.2$ and $\nu_{tl} = \nu_{lt}/4$. The fibre has a width $w = 0.43l$ and thickness t . The exact area of the fibre is $A_0 = 0.43l^2$.

The problem is formulated as a plane stress case and solved with a non-conforming fixed grid by the standard FEM and the LS-XFEM approach. In the standard finite element setting, a finite element is considered to be part of the fibre if the centroid of the finite element is located inside the fibre. Accordingly, these fibres contribute to the finite element stiffness in the FEM solutions. In the

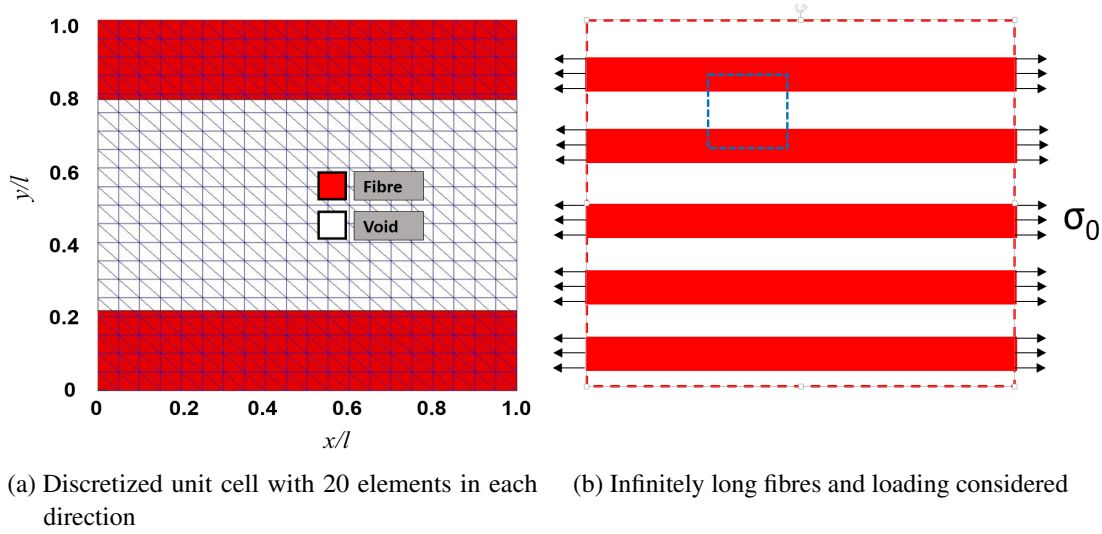


Figure 9: A single fibre in a periodic unit cell.

l/h (uniform mesh)	$\sigma_{xx}(\text{FEM})/\sigma_0$	$\sigma_{xx}(\text{LS-XFEM})/\sigma_0$	Area captured (FEM)/ A_0	Area captured (LS-XFEM)/ A_0
10	1.0750	1.0043	0.9302	0.9957
20	1.0750	0.9998	0.9302	1.0000
40	1.0117	0.9998	0.9883	1.0000

Table 1: Computed stresses and areas obtained by the standard FEM and LS-XFEM.

LS-XFEM formalism, a finite element partially covering a fibre still represents that fibre but the area of the fibre in that finite element is determined using the area integration method presented in earlier section and it contributes to the element stiffness accordingly. The results obtained by these two approaches for different grid spacings (element edge lengths) h are presented in Tab. 1 in terms of the (local) fibre stress component σ_{xx} as computed and the fibre area considered by the numerical model.

As expected, the standard FEM does not yield a good estimate of the stresses with a coarse non-conforming mesh of 10 elements along the cell edge. On the contrary, the LS-XFEM formalism yields an accurate stress distribution with the same mesh. As the mesh is refined, the standard FEM still struggles to yield the expected accuracy. However, the LS-XFEM formalism captures the geometry with a better accuracy, which also results in a more accurate prediction of the stress level.

2.4.1.2 Bonded elementary network under tension

The attention is next shifted towards the simplest fibre arrangement that involves bonds, between two orthogonal families of parallel fibres subjected to a stress σ_0 , as introduced in [8], see Fig. 10b. Because of periodicity, the unit cell depicted in Fig. 10a is used, with half fibres along the edges. The material parameters are identical to the those of the previous example. The LS-XFEM formalism, with a regular mesh with $h=l/50$, as shown in Fig. 10a, is used to predict the mechanical response

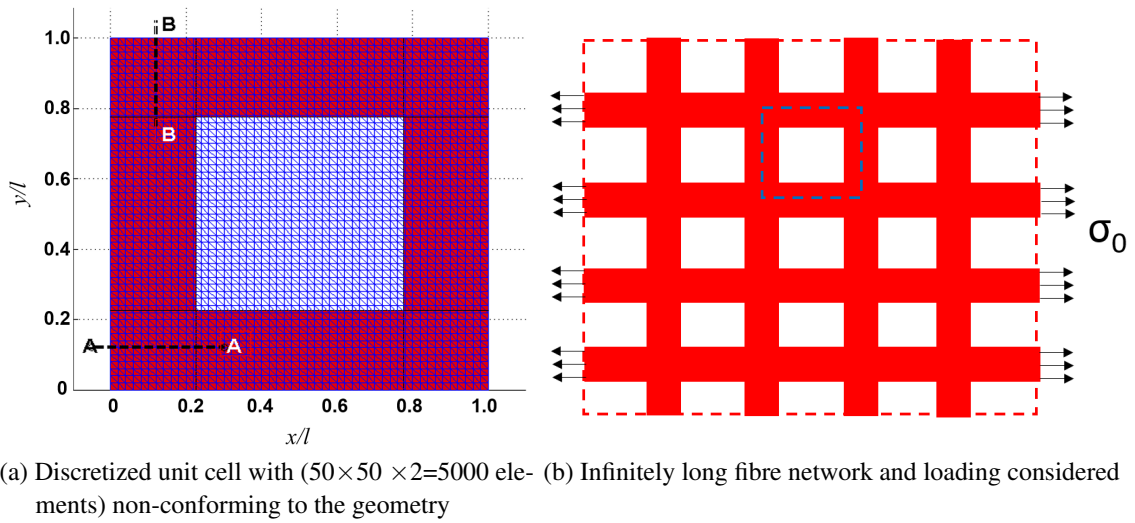


Figure 10: Fibre network with a regular mesh non-conforming to the geometry. The σ_{xx} profiles along the cross-sections A-A and B-B are depicted in Fig.13.

especially focusing on the stress distribution, in the bonded regions.

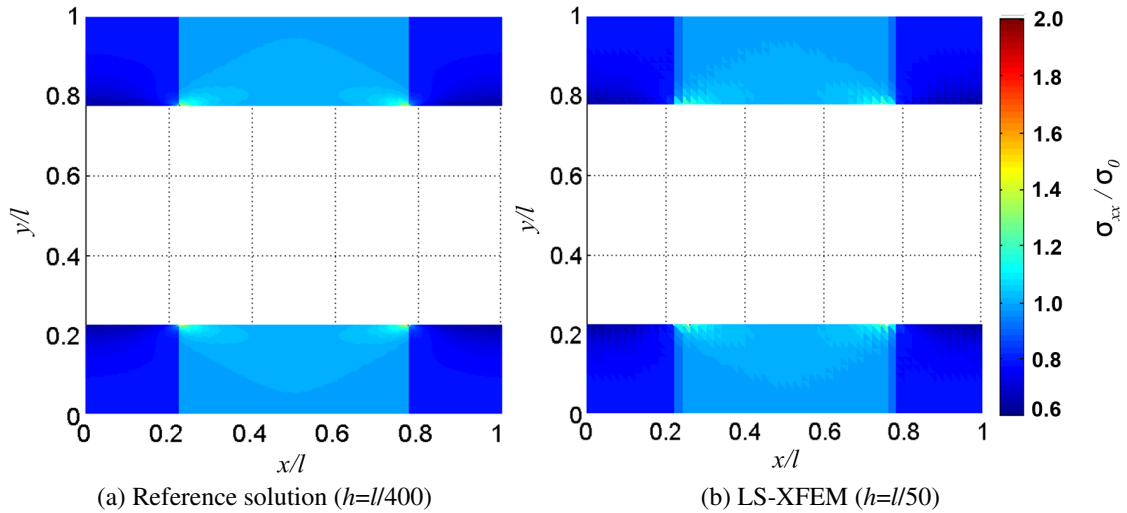


Figure 11: Stress distributions, σ_{xx}/σ_0 , in horizontal fibre.

This network is also modeled with a very fine FE mesh of size $400 \times 400 \times 2$ elements conforming to the geometry, serving as a reference solution. It is emphasized that such a conforming mesh is of course only achievable for simple configurations as considered in this example.

Figs. 11 and 12 show the normalized stress distribution σ_{xx} in the bonded regions for the horizontal and vertical fibres as computed by the LS-XFEM with a non-conforming mesh and the FEM reference solution. The coarse triangular mesh used for the LS-XFEM formalism is evident in the jagged normalized stress distribution in the free standing and bonded regions in Fig. 11b. Also,

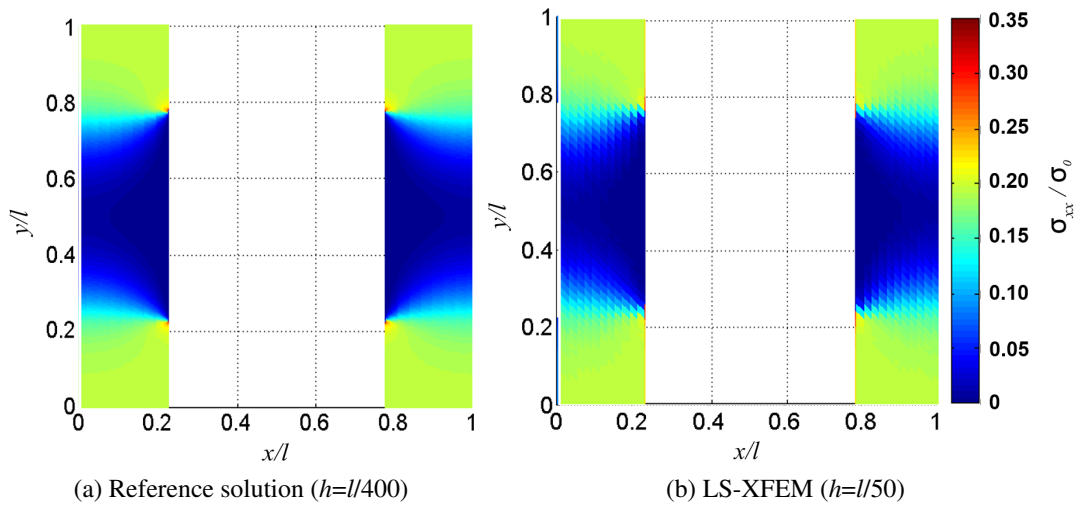


Figure 12: Stress distributions, σ_{xx}/σ_0 , in the vertical fibre.

these are noticed near the bonded region of the vertical fibres in Fig. 12.

Note that only at locations ($x/l = 0.2$), close to the edges of the bond, the stress distribution predicted by LS-XFEM differs from the reference solution with a deviation of $< 20\%$, as observed in Fig.13(a). This is because with the LS-XFEM formalism employing a geometry non-conforming coarse mesh, the finite element at this location lies in the bond as well as in the free standing fibre. Now, the stress distribution σ_{xx} is high in the free standing fibre resulting in the stress jumps obtained by LS-XFEM. However, in the geometry conforming the mesh employed by the FEM solution, the finite element (with a finer mesh) is still lying inside a bond at this location with low σ_{xx} . As $x/l > 0.2$, the finite element now lies in a free-standing fibre with a higher stress and therefore the stress distribution by the FEM also attains the same value as predicted by LS-XFEM formalism in the free-standing fibre areas. Most importantly, as noticed in these plots, the normalized stress distributions predicted by the LS-XFEM formalism are qualitatively and quantitatively similar to the reference solutions at other regions which is further ascertained in the cross-sectional plots through the bonds shown in Fig. 13.

In a fibrous network, the bonded regions are vital for an accurate prediction of the overall network response, as well as for the proper reproduction of the local behavior of the fibres [8]. Therefore, the ability of LS-XFEM formalism to make adequate predictions of the mechanical stress state inside the bond at a lower computational cost as compared to a fine FEM discretization, makes it a suitable tool for modeling the fibrous networks.

2.4.2 Complex networks

The attention is now focused on more complex (realistic) networks, to illustrate the ability of the proposed formalism to recover information at both the microstructural and macroscopic level.

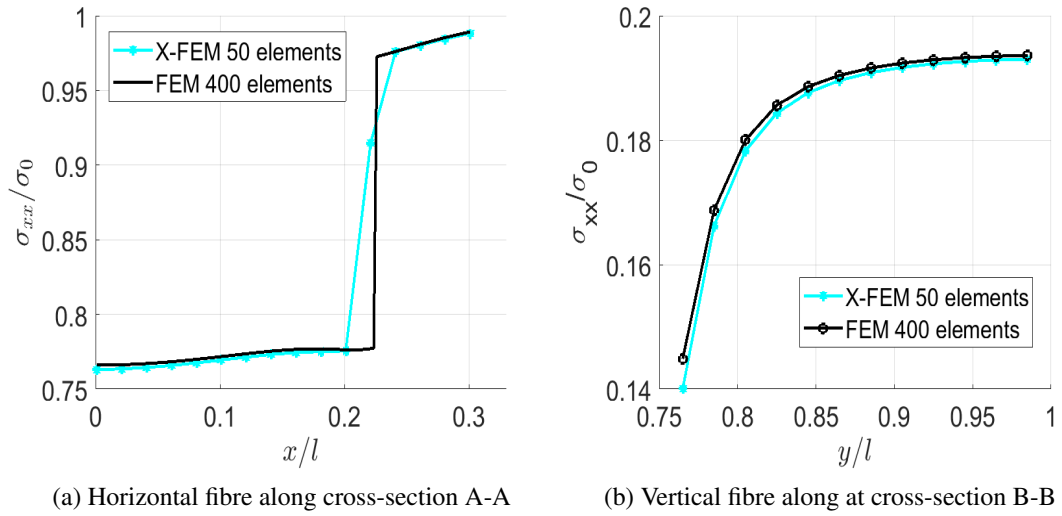


Figure 13: Stress, σ_{xx}/σ_0 , in cross-sections as defined in figure 10a.

2.4.2.1 Network parameters

Different network configurations are considered, with coverages of $c = 0.9$ and $c = 1.8$ (defined as the ratio of total area occupied by the fibres in the network to the area of the microstructural unit cell). The characteristic size of the finite elements used in the mesh to model the unit cell is chosen as $h_L = \frac{l}{100}$. After application of the refinement strategy at the fibre edges, the smallest finite element size reduces to $h_S = \frac{l}{400}$. For the anisotropic behavior of the fibres, the material parameters used are identical to that of the previous examples. The coefficients of hygroscopic expansion are taken according to $\beta_t = 20\beta_l$ for all cases. A unit change in moisture content, $\Delta\chi = 1$, is adopted which is assumed uniform over the entire unit cell.

2.4.2.2 Average expansivity and deformed geometry

The initial anisotropic network for coverage $c=0.9$ and anisotropy parameter $q=0.5$ is shown in Fig. 14a. The hygro-mechanical response of the unit cell is computed by solving the static equilibrium problem for a unit change in moisture content, $\Delta\chi$. This generates a hygroscopic load causing deformation in the network, which is computed by means of the LS-XFEM formalism on a discretization with 4 levels of refinements, see Fig. 14b). The response of the same network is computed as well using a regular mesh of size equal to the smallest element size of the refined mesh h_S with a standard finite element method.

It can be observed in Fig. 15 that the deformed geometry obtained by the LS-XFEM (with a relatively coarse mesh), in Fig. 15b, is similar to the deformed network obtained by standard FEM with a very fine mesh in Fig 15a. This result demonstrates the added value of LS-XFEM in terms of solving a network with a system of smaller size. This is further illustrated by the overall behavior on the basis of the computed overall hygroscopic coefficients of the network, as listed in Tab. 2. The anisotropic network fabric ($q = 0.5$) causes a pronounced overall anisotropy: the expansivity $\bar{\beta}_{yy}$ in the CD direction exceeds that of the MD direction, $\bar{\beta}_{xx}$, by more than a factor of three.

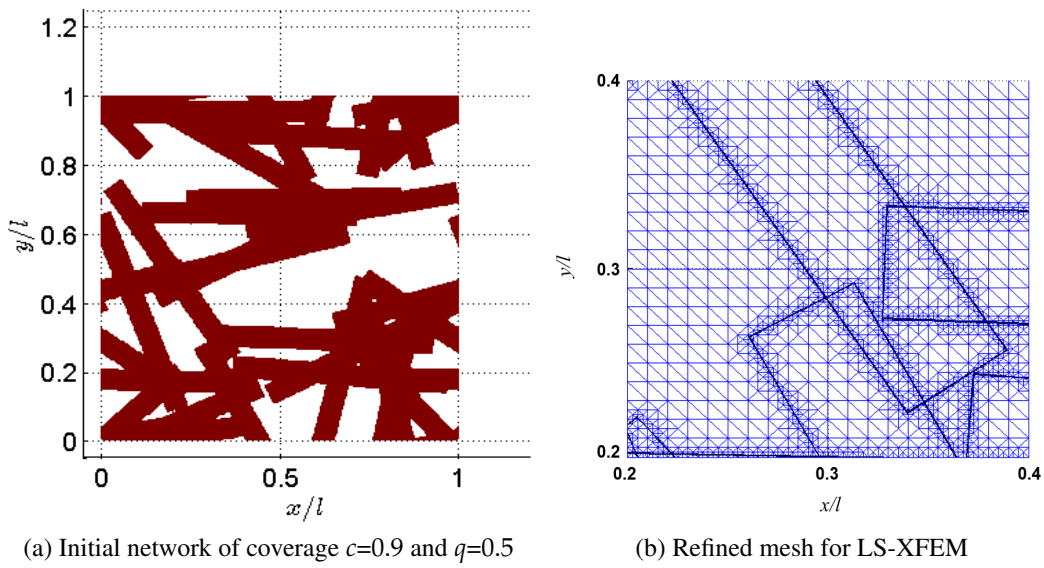


Figure 14: Geometry of the complex network and the zoom of mesh used.

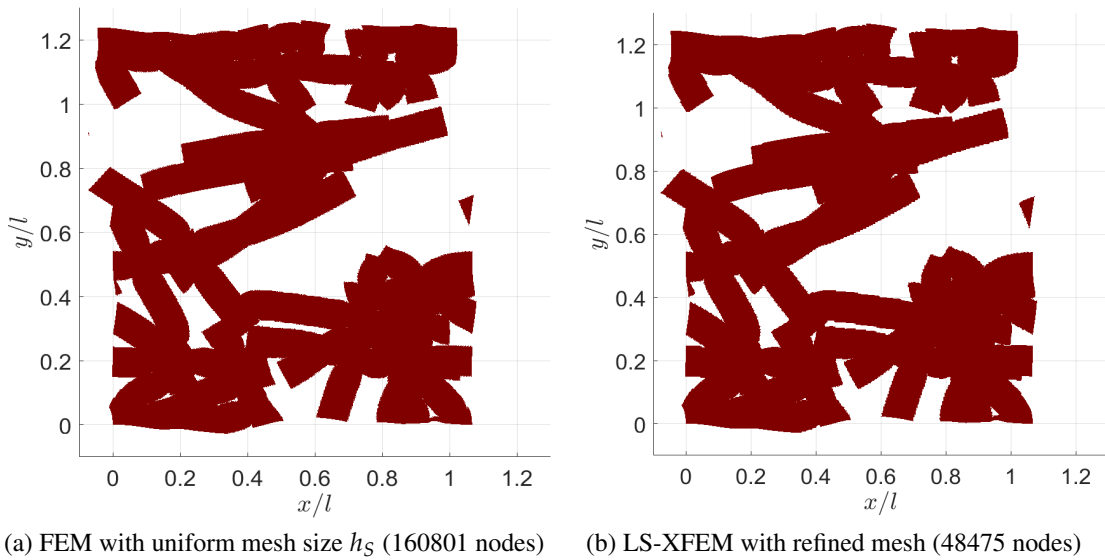


Figure 15: Deformed network as computed by FEM and LS-XFEM. The displacements have been magnified by a factor of 50.

Approach	$\bar{\beta}_{xx}/\beta_l$	$\bar{\beta}_{yy}/\beta_l$	$\bar{\beta}_{xy}/\beta_l$
LS-XFEM	2.4278	8.6910	-1.6682
FEM	2.4042	8.5020	-1.6380

Table 2: Computed effective hygro-expansive coefficients normalized with β_l for the anisotropic network ($c=0.9$ and $q=0.5$).

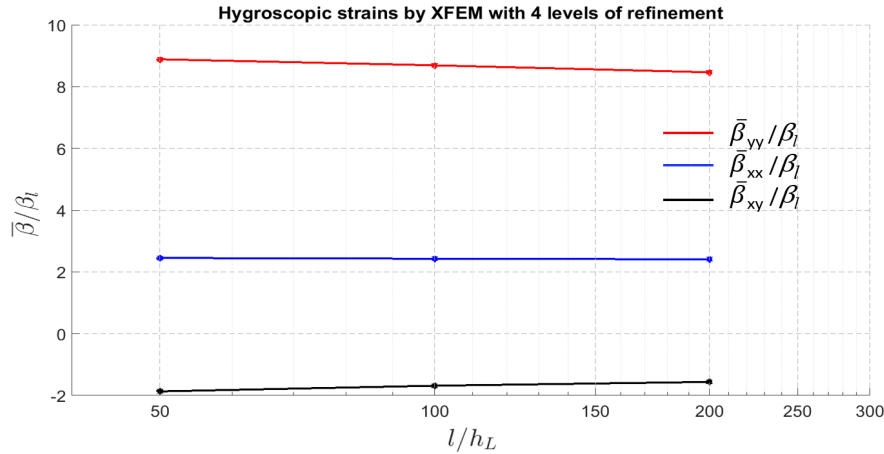


Figure 16: Convergence of the effective hygroscopic coefficients normalized with $\beta_l \Delta \chi$ obtained by the LS-XFEM as a function of the characteristic element size.

This is due to the fact that the fibres are on average more oriented in the MD direction, i.e. their expansion occurs predominantly in the CD direction. The values obtained by LS-XFEM have a relative deviation of less than 1% for $\bar{\beta}_{xx}$ and 2.2 % for $\bar{\beta}_{yy}$, when compared against the fine mesh FEM solution for the same network.

If we consider a curved shape of fibres instead of rectangular straight fibres, a single fibre will exhibit less stiffness comparatively. On a network scale at low coverages its difficult to predict the effect this would have on effective hygro-expansivity. However, at higher coverages the response is expected to be same because the spacing of bonds is small and the fibre segments in between them are practically straight at this scale.

In Fig. 16, convergence of the normalized effective hygro-expansivity of the network with an increasing number of elements in the mesh for the LS-XFEM formalism is shown. There is no significant change in the effective coefficients of the network with an increase in the number of elements. Even with the coarsest discretization considered, i.e. $h_L=l/50$, we obtain a response which is within 10% of the response obtained at $h_L=l/200$. This demonstrates the advantage of using the LS-XFEM formalism.

In Fig. 17, an anisotropic network with a higher coverage is considered ($c = 1.8$). For this case, the bonded area in the network is larger, resulting in a comparatively higher hygroscopic strain and overall deformation. As in the previous case, the anisotropic orientation of fibres in the network

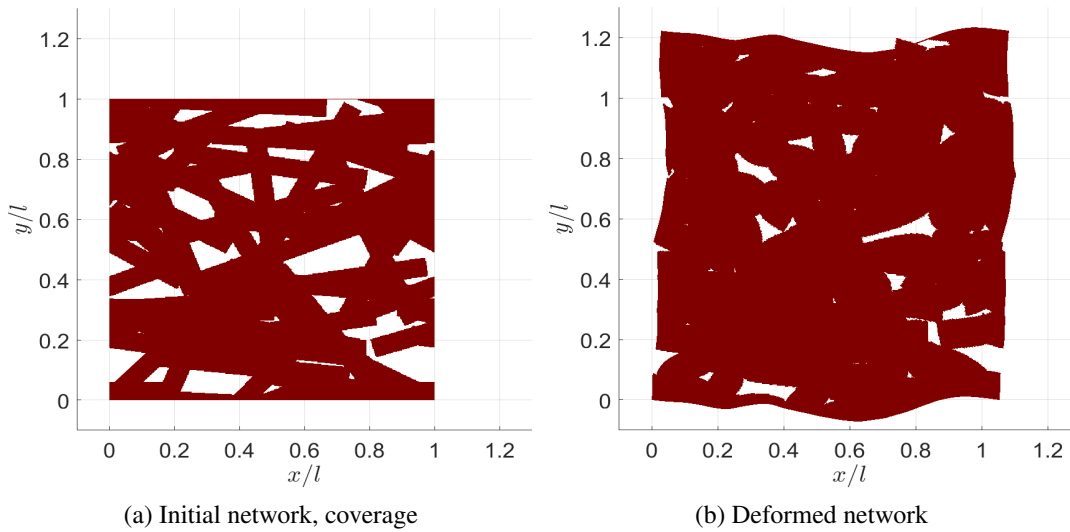


Figure 17: A high coverage network ($c=1.8$ and $q=0.5$). The displacements have been magnified by a factor of 50.

$\bar{\beta}_{xx}/\beta_l$	$\bar{\beta}_{yy}/\beta_l$	$\bar{\beta}_{xy}/\beta_l$
2.7989	3.1457	1.3573

Table 3: Computed effective hygro-expansive coefficients normalized with β_l for the isotropic network ($c=0.9$ and $q=0$).

results in a higher expansion along the cross-direction.

Hence, both the anisotropy and higher coverage contribute to a higher expansion in the cross-direction when compared with networks having low coverages. Let us emphasize again that the use of a conforming mesh with the finite element method for networks with a high coverage is computationally highly expensive, because meshes have to be very fine to capture such complex bonds with many overlapping fibres of different orientations.

Finally, an isotropic network ($q = 0$) with low coverage is also considered. The values of the expansivity in MD ($\bar{\beta}_{xx}/\beta_l$) and CD ($\bar{\beta}_{yy}/\beta_l$) are listed in Tab 3. Theoretically, the listed values should be identical, if the network would be truly isotropic. However, they differ by approximately 10% due to the sparsity and the statistically small size of the network used.

2.4.2.3 Local behaviour

Local strain distributions in the complex fibrous networks obtained by the LS-XFEM formalism are analyzed in this section by comparing them against the high resolution FEM solutions. In Fig. 18 & 19, the normalized strain distributions are plotted for, respectively, the LS-XFEM (48475 nodes) and standard FEM solution with a fine mesh (160801 nodes).

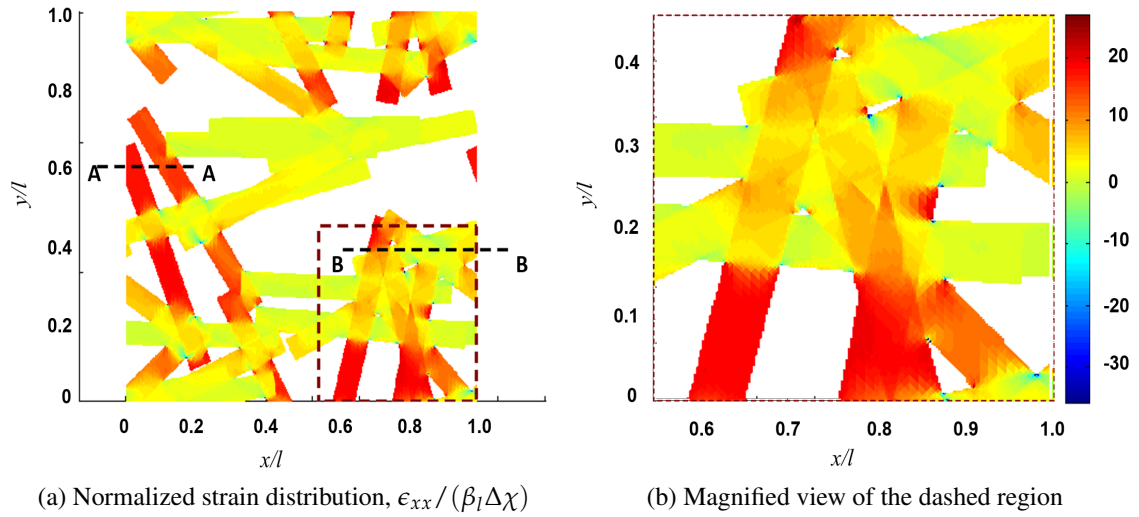


Figure 18: LS-XFEM solution obtained with refined mesh (48475 nodes, $c=0.9$ and $q=0.5$).

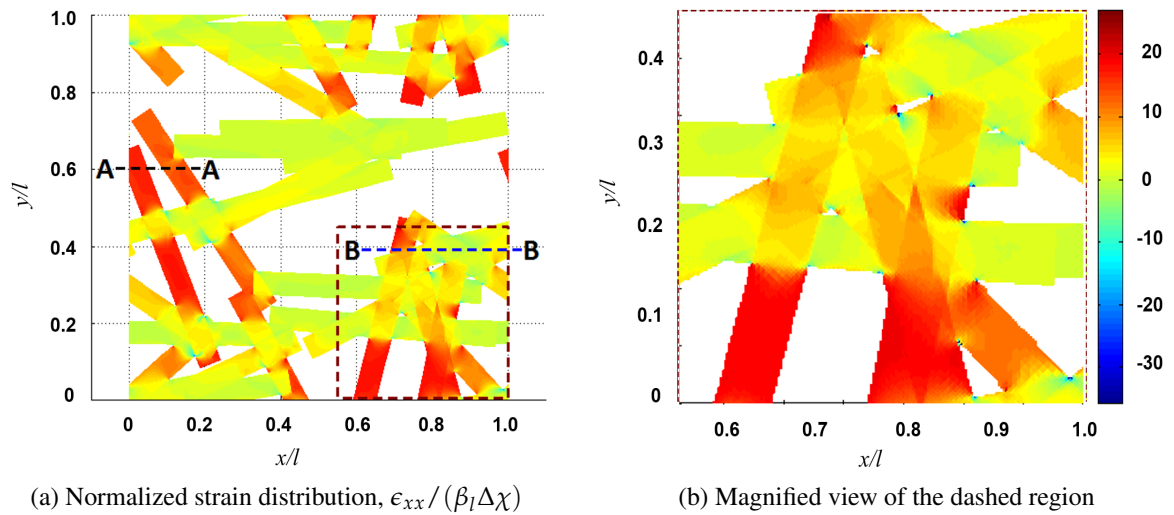


Figure 19: FEM with mesh size $h_S=l/400$ for the network ($c=0.9$ and $q=0.5$).

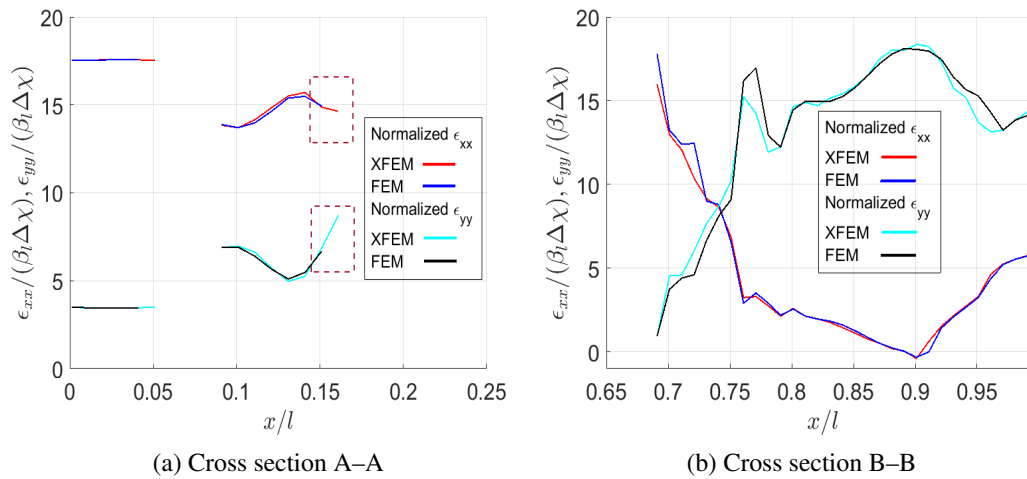


Figure 20: Normalized strain in the network at cross-sections A–A and B–B unresolved regions.

The strain distribution obtained by the LS-XFEM is accurately computed in the overall network as well as in the bonds. For a better comparison, the magnified views of the normalized strain distribution are plotted in Fig. 18b and 19b. The normalized strains along the cross-section A–A and B–B are further plotted in Fig. 20. At a few locations, e.g. at $x/l=0.16$ in the dashed box in Fig. 20a, a strain value is predicted by LS-XFEM, whereas there is no value for the reference FEM. This is because in the FEM this element is in a void whereas in the LS-XFEM solution, the corresponding finite element is identified as an interfacial element, as is noticeable in Fig. 21b. The area of fibre in the element is captured accurately by the element through the sub-triangulation stated earlier. However, there is no strain predicted at this location by the standard FEM employing the fine mesh used here. As the position of the centroid of the finite element inside the fibre is the sole criterion for modeling the fibres in standard FEM, it is observed in Fig. 21a that the corresponding finite element centroid lies outside the fibre thereby modeling it as a void with no strains. Similar effects would occur in bonded areas, with unresolved regions in FEM where it fails to capture the fibres despite its fine mesh. Therefore, the LS-XFEM results in a more accurate strain distribution in the cross-section A–A of the network with a smaller system size, even though the fibre geometry and the mesh are decoupled.

The results presented above demonstrate the ability of the proposed LS-XFEM formalism to resolve the effect of the network's geometry and fibre hygro-mechanical properties on the hygro-mechanical behavior at the sheet-scale, in spite of making use of a rather coarse discretization. This opens the possibility to systematically study the effect of different microstructural parameters at an affordable computational cost.

2.5 CONCLUSIONS

This chapter presented a computational methodology for analysis of the hygro-mechanical response of fibre networks using an XFEM framework with a level set based geometry description. A two-dimensional unit cell consisting of a network of fibres has been considered to this end. It was subjected to free expansion by a uniform field of hygroscopic loading caused by a change

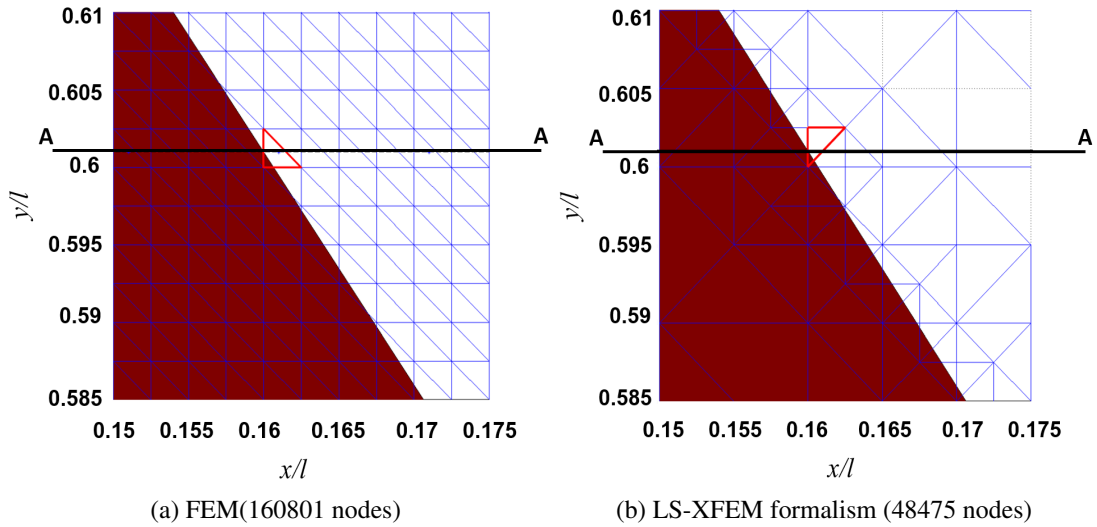


Figure 21: The discretized network with the finite element triangle at c/s A-A and $x=0.16$ are highlighted.

in moisture. Rectangular fibres were generated randomly to produce periodic cells representing complex networks. The initial geometry of each fibre was described using a level-set function. The coupling between level-sets and the XFEM was carried out by means of a Heaviside function enrichment based on the level-set function. The edges of the fibres were captured from the nodal values of the level-set function. In this manner, a connection was established between the finite element mesh and the internal fibre geometry using the level-set formalism, which simplifies and improves the efficiency of computations for complex geometries in XFEM.

An accurate tracking of the boundaries of the fibres in the network was achieved, especially in the bonded regions, which matter for the prediction of the hygro-mechanical response of the network subjected to moisture infiltration. Local fields in the network (stress, strains and displacements) could be evaluated accurately as compared to a reference finite element solution with a fine mesh. The LS-XFEM results were obtained with a relatively small system size. The LS-XFEM formalism is thus a suitable tool for modeling fibrous networks while capturing the interfaces with an adequate accuracy.

In the LS-XFEM formalism as we saw in 2D with a lower system size, it does good work in prediction of the hygro-mechanical response of complex fibrous network. Consequently in 3D, with a lower system size this may result in reduced computational efforts and therefore might be a big advantage. At the sametime, it has benefits of capturing the geometry accurately with this lower system size. In the subsequent chapters, the standard FEM approach was used for modelling because the simulations presented there are two-dimensional and the computational expenses were affordable. Also, we are interested in assessing certain hygro-mechanical behaviour of the networks qualitatively. The hygro-mechanical response of the networks does not undergo any significant changes qualitatively upon adoption of the standard FEM as compared to LS-XFEM.

Possible extensions of this work include the modeling of irreversible shrinkage behavior in paper like materials. During the manufacturing process of paper, internal stresses are developed when the paper is dried under tension. They are released when the paper is subjected to a moisture

cycle, resulting in irreversible shrinkage [7]. This behavior can be included by considering suitable constitutive models.

MICRO-MECHANICAL MODELING OF IRREVERSIBLE HYGROSCOPIC STRAIN IN PAPER SHEETS EXPOSED TO MOISTURE CYCLES

Paper is a complex material consisting of a network of cellulose fibres at the micro-level. During manufacturing, the network is dried under restraint conditions due to tension in the paper web in machine direction. This prevents it from shrinking and gives rise to internal strains that get stored in the produced sheet. Upon exposure to a moisture cycle, these strains may be released. This results in permanent shrinkage that may cause curls or waviness in the printed sheet. The prime objective of this chapter is to model this irreversible shrinkage and to link its magnitude to the properties of the fibres and the network. For this purpose, randomly generated isotropic fibrous networks of different coverages (ratio of the area occupied by fibres over the cell face) are modeled by means of a periodic representative volume element (RVE). Within such RVEs, a finite element method combined with a kinematic hardening model at the scale of the fibres is used to capture the irreversible response. Computational results obtained demonstrate that the irreversible strains increase until a certain coverage and thereafter subsequently decrease in magnitude. This phenomenon is explained by considering the area fraction of free-standing fibre segments relative to bonded fibre segments in the network. A structure-property dependency of irreversible strains at the sheet-level on the microstructural parameters of the network is thereby established.

Keywords: Fibrous network, restrained drying, irreversible strains, coverage

³ This chapter is based on: P. Samantray, R.H.J. Peerlings, T.J. Massart, M.G.D. Geers, 2019. *Micro-mechanical modelling of irreversible hygroscopic strain in paper sheets exposed to moisture cycles*. In preparation.

3.1 INTRODUCTION

Paper belongs to a category of materials that are composed of a network of fibres produced from wood pulp. At the micro-level, parts of fibres are bonded with each other at some locations while they are free standing elsewhere as seen in the two fibres periodic cell in Fig. 22b of a network of parallel fibres infinitely long as shown in Fig. 22c. This meso-scale network for paper was used earlier by Bosco, Peerlings, and Geers [7] to analyze the irreversible strains. During the manufacturing process, the paper fibres obtain a preferential orientation (in machine direction) which results in an anisotropic behavior of paper [56]. Upon exposure of a sheet of paper to a humid environment, anisotropic moisture induced swelling, or hygro-expansion takes place [37]. This swelling originates at the scale of fibres and gets propagated through the network by the inter-fibre bonds, where interactions between the hygroscopic and the mechanical properties of the fibres occur.

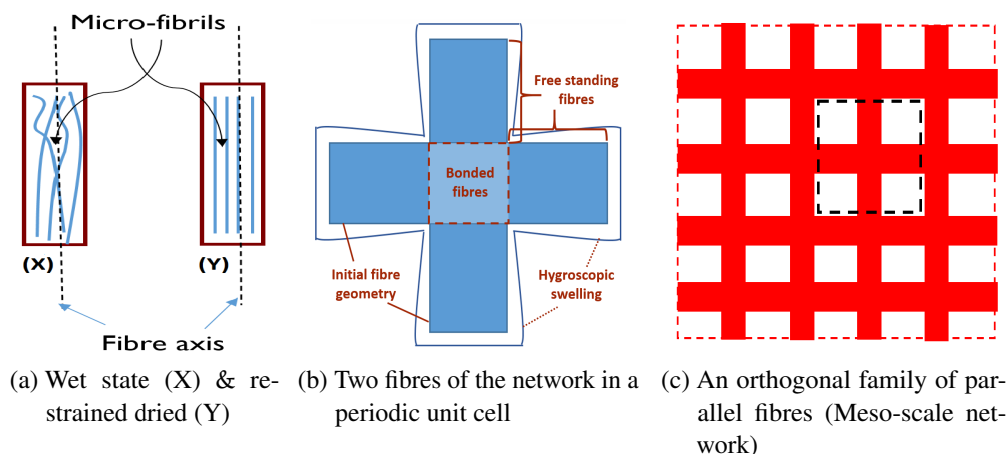


Figure 22: Fibre segment activation mechanism and Meso-scale network representation.

In applications like printing, the consequences of these deformations may be observed through curl, waviness and cockling at the macro-scale. Understanding these phenomena and their dependence on the properties of the fibres and the network is essential to predict the overall response of the material at the sheet-level.

The overall behavior of paper is dependent on the drying phase during its manufacturing process. In the case of restrained drying, an initial strain is generated in the paper fibres due to the fibre segment activation mechanism [74]. According to this mechanism, restrained drying of the paper fibres leads to a decrease in the orientation angle of the microfibrils with respect to the axis of the fibres, as sketched in Fig 22a. As a result, the fibres are stretched and develop an internal stress. This mechanism induces dried-in strains that remain in the paper after manufacturing. When the manufactured paper is exposed to a moisture cycle beyond a certain moisture content, the initial dried-in strains are released to some extent resulting in irreversible shrinkage. This effect was measured for instance by Mäkelä [43] as illustrated in the experimental data in Fig 23b. This is generally interpreted as a permanent or irreversible hygroscopic strain. However, these dried-in strains are absent if paper would be dried freely in the manufacturing process. Therefore, a reversible hygroscopic response is observed upon exposure to a moisture cycle as noticed in Fig. 23a. In

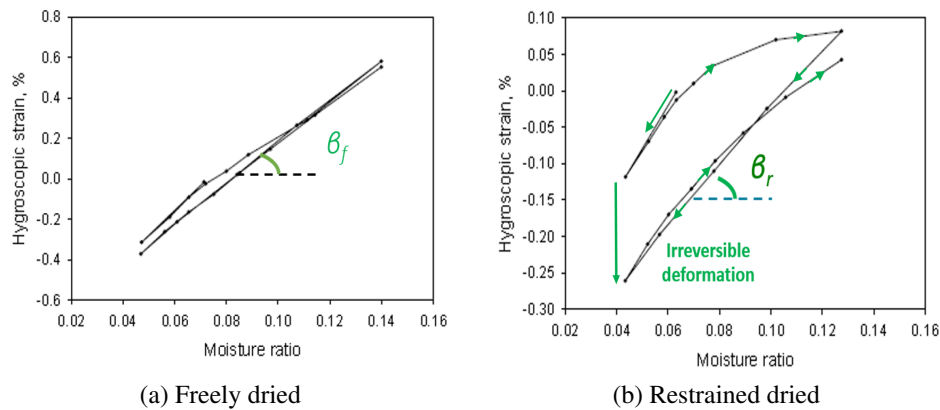


Figure 23: Experimental results for a hand sheet obtained by Mäkelä [43].

order to fully understand this characteristic behavior of paper and assess the microstructural factors affecting it, a model of the underlying complex fibrous network is essential.

Published works on the relationship between the macroscopic behavior of fibrous networks and the microstructural parameters include the dependence of stress transfer on the correlation length in a network [5]; fracture of the network dominated by fibres longer than the average length [2]; the mechanical response of fibrous networks depending on the curl ratio [77]; the magnetic and mechanical response of bonded networks of metal fibres due to filling in voids [15]; the influence of the aspect ratio and fibre concentration on the effective stiffness of planar fibre networks [76]. Early attempts at structure-property relations for fibrous networks specifically addressed the mechanical response. [1, 12, 17] studied the stiffness of fibre networks by taking into account i.e. the axial forces and transverse properties of fibres. Some of the papers considered the bonds in the networks enabling models to transmit axial and shear forces along with torsional and bending moments [53, 63, 67]. In Kulachenko and Uesaka [36], it was shown that the strength and the elastic modulus of the fibre network had little variation as long as the average number of fibres and degree of the orientations are kept constant. In Shahsavari and Picu [66], a simple relation was formulated which creates the least model size at which the size effect does not exist anymore. Dirrenberger, Forest, and Jeulin [20] determined RVE sizes after carrying out homogenization for thermal and elastic properties by FEM with mixed and uniform boundary conditions for many realizations.

Among the available studies, some focused on the hygro-expansion and dimensional stability of the paper, e.g. [47, 59, 71, 72]. In them, the hygro-expansivity of networks is studied by establishing a relation between the dimensional stability and different parameters that affect it, like the fibre-fibre contact ratio, relative humidity, wet pressing of sheets, density or exchange of heat and moisture between paper and surroundings. Considering the irreversible strains at sheet scale of paper as discussed a little earlier, several complex phenomena occur at different scales at the micro-level that may be responsible for such behavior. Therefore, it is difficult to associate a particular mechanism to the irreversible hygro-mechanical response. The mechanisms responsible for such behavior of paper sheets are still being discussed currently in the literature. However, the literature provided insight on the influence of fibre segment activation mechanism on the irreversible hygroscopic strains. Recently, Bosco, Peerlings, and Geers [7] studied the irreversible shrinkage response of a meso-scale

simplified network as shown in Fig. 22b that is subjected earlier to restrained drying. In order to gain insight into the irreversibility phenomenon occurring at the sheet scale, we have also described it by adopting the fibre segment activation mechanism. Our main goal is to understand the dependence of the results on the network by considering a random network model instead of meso-scale network.

The main objective of the present work is to gain a qualitative understanding of the irreversible hygroscopic response of a complex fibrous network of paper by modelling it numerically. For this purpose, a two-dimensional periodic random network model similar to that of Bosco, Peerlings, and Geers [7] is used, exploiting the kinematic hardening plasticity model with a moisture dependent yield strength. The use of plastic models as well as a yield strength for the fibres is currently under discussion in literature. One of the main features of the constitutive model is the occurrence of irreversible shrinkage in the longitudinal direction of fibres based on the fibre segment activation mechanism. This particular modeling aspect of irreversible shrinkage of complex paper fiber networks was not addressed so far.

Following earlier work by Bosco, Peerlings, and Geers [9], the fibre network is generated in a 2D framework with fibres being modeled as ribbon like rectangular domains. In the present contribution, an isotropic orientation distribution function of the fibres is used in the generation of the network, to resemble a hand sheet. A linear kinematic hardening model is used to represent the irreversible shrinkage in longitudinal direction of the fibres associated with the activation mechanism. The phenomenon of manufacturing induced dried-in strains is explicitly incorporated. The release of strains is represented as a quasi static phenomenon and therefore a rate-independent model is adopted. This is an adequate assumption for understanding the effects of network properties on the sheet-scale behavior.

This chapter is organized as follows. In Section 2, the modeling methodology for capturing the irreversible behavior of fibres is described, along with the details of the fibre constitutive model. Results highlighting the irreversible shrinkage of the complex network are presented in Section 3. Interactions between the activation mechanism and microstructural features (e.g. coverage) are also investigated in this section. Finally, in section 4, conclusions and perspectives are provided.

Throughout this contribution, the following notations are used. Scalars, vectors and (Cartesian) tensors are denoted by a , \vec{a} and A respectively; 4th order tensors are represented by 4A . For tensor and vector operations, the following equivalent notations are used with Einstein's summation convention on indices: $A:B=A_{ij}B_{ji}$ with $i = x,y,z$ for the global reference system and $i = 1,t,z$ for the local, fibre-reference system. The dyadic product between vectors is represented as $\vec{a}\vec{a}$. The Voigt notation used to represent tensors and tensor operations in a matrix format is as follows: \underline{a} and \underline{A} denote a column matrix and a matrix of scalars respectively. Matrix multiplication is denoted as $\underline{A} \underline{a} = A_{ij}a_j$.

3.2 MICROSTRUCTURAL MODELING BY KINEMATIC HARDENING PLASTICITY

3.2.1 *Random network creation*

In the current study, assuming the paper fibres to be ribbon shaped in nature, a set of rectangular shaped fibres are randomly generated. The length of the fibres is denoted by l_f and the width by, $w_f=l_f/50$. The centroids of the fibres are randomly generated in the domain $[x,y] \in [0,l] \times [0,l]$ within a periodic unit cell of edge length, $l=l_f$ as shown in Fig. 24.

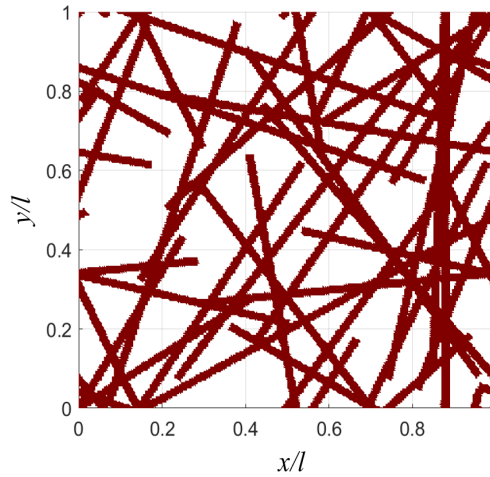


Figure 24: A periodic random fibrous network of coverage, $c=0.5$ represented by a periodic unit cell.

The orientation of the fibres are randomly generated. All the fibres have identical rectangular shape and dimensions. The entire network is periodic along its boundary edges. Fibre parts which extend beyond the boundary of the unit cell are periodically copied into the cell at the opposite edge. At the regions of overlap, the fibres are assumed to be perfectly bonded. In order to depict the denseness of the network, the coverage c (ratio of the total area occupied by all fibres and the area of the periodic unit cell) is defined, which will be used in the next section for analysis of results.

3.2.2 *Modeling fibre longitudinal and transverse behavior*

In order to describe the irreversibility phenomenon in the longitudinal direction of a fibre only due to tension, a plane stress plasticity model with linear kinematic hardening is adopted. After the paper is manufactured under restrained conditions, it is subjected to free expansion due to a moisture cycle representing the absorption of moisture from the environment as well as the evaporation of moisture. Accordingly, there is no externally applied stress responsible for the irreversible phenomenon as observed in the experiments described earlier [43]. However, the decreasing moisture content and the initially stored backstress during the restrained drying process determine when plasticity may occur in the re-wetting phase via the release of the initially dried-in strains or backstress. A kinematic hardening model will thus be used for modeling the release of strains in absence of an external stress, but triggered by the internal backstress only. We will assume that this phenomenon takes

place over a sufficiently long period of time so that time-dependent deformations can be ignored.

In this contribution, a two-dimensional generalization of the fibre constitutive model proposed by Bosco, Peerlings, and Geers [8] is adopted. The general constitutive law for a fibre makes use of a plane stress assumption in the thickness (z) direction.

In the kinematic hardening plasticity model with linear hardening used, the total strain in a fibre has an additional component of plastic strain in addition to the elastic and hygroscopic strains so as to model the irreversible hygroscopic strains.

$$\epsilon^f = {}^e\epsilon^f + {}^p\epsilon^f + {}^h\epsilon^f \tag{16}$$

where ϵ^f , ${}^e\epsilon^f$, ${}^p\epsilon^f$ and ${}^h\epsilon^f$ are the strain tensor, the elastic strain tensor, plastic strain tensor and hygroscopic strain tensor of the fibre respectively.

When subjected to a moisture change $\Delta\chi$, the fibres develop a hygroscopic strains ${}^h\epsilon^f$ given by.

$${}^h\epsilon^f = \beta^f \Delta\chi \tag{17}$$

where β^f is the hygro-expansivity tensor.

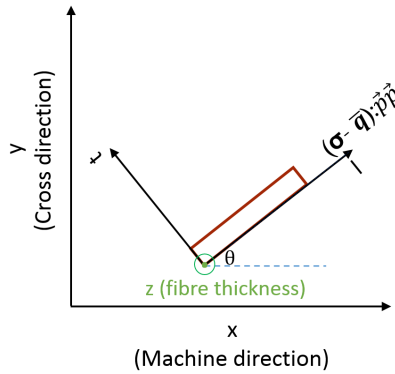


Figure 25: The local and global coordinate axes.

The stress in the fibre is given by

$$\sigma^f = {}^4D^f : {}^e\epsilon^f, \tag{18}$$

$$= {}^4D^f : (\epsilon^f - {}^p\epsilon^f - {}^h\epsilon^f) \tag{19}$$

Here, where ${}^4D^f$, is the elastic constitutive tensor. In Voigt matrix notation, ${}^4D^f$ and β^f are represented as

$$\underline{D}^f = \begin{pmatrix} \frac{E_l}{(1-\nu_{lt}\nu_{tl})} & \frac{E_l\nu_{tl}}{(1-\nu_{lt}\nu_{tl})} & 0 \\ \frac{E_t\nu_{lt}}{(1-\nu_{lt}\nu_{tl})} & \frac{E_t}{(1-\nu_{lt}\nu_{tl})} & 0 \\ 0 & 0 & G_{lt} \end{pmatrix}, \underline{\beta}^f = \begin{pmatrix} \beta_l \\ \beta_t \\ 0 \end{pmatrix} \tag{20}$$

where E_l and E_t are the elastic moduli in the longitudinal and transverse direction with respect to the fibre axis, G_{lt} is the in-plane shear modulus, ν_{lt} and ν_{tl} are the in-plane Poisson's ratios. β_l and

β_t denote the coefficients of hygroscopic expansion in the longitudinal and transverse direction of the fibre axis respectively. These material parameters are assumed to be independent of χ . This will give a better picture of the sole qualitative effect of the microstructural parameters like coverage, free-standing fibres etc on the irreversible strains, while keeping the model relatively simple and the number of parameters manageable.

The local reference system (l,t,z), of a fibre m is oriented at an angle $\theta^{(m)}$ with respect to the global reference system (x,y,z), see Fig. 25. Therefore, it is important to transform the above expression from the local frame of the fibre to the global frame for each fibre in the network. The rotated elastic constitutive tensor and effective hygroscopic coefficient, as described (Roylance [55]), are thereby obtained.

In the kinematic hardening model, an associative flow rule is used to determine the plastic strain rate tensor, ${}^p\dot{\epsilon}^f$ and kinematic strain hardening tensor, $\dot{\bar{\zeta}}^f$.

$${}^p\dot{\epsilon}^f = \dot{\gamma}N, \quad \dot{\bar{\zeta}}^f = -\dot{\gamma}N \quad (21)$$

where $\dot{\gamma}$ is the plastic multiplier and N gives the direction of plastic flow. The plastic strain tensor ${}^p\epsilon^f$, contains only one non-zero component i.e. in the longitudinal direction.

$${}^p\epsilon^f = \begin{bmatrix} {}^p\epsilon_l^f \\ 0 \\ 0 \end{bmatrix}, \quad \bar{\zeta}^f = \begin{bmatrix} \bar{\zeta}_l^f \\ 0 \\ 0 \end{bmatrix} \quad (22)$$

$$\bar{q}^f = -{}^4H^f : \bar{\zeta}^f \quad (23)$$

$$F^f = |(\sigma^f - \bar{q}^f) : \vec{p}\vec{p}| - \sigma_y \quad (24)$$

The Kuhn Tucker consistency conditions must be satisfied $\dot{\gamma} \geq 0$, $\dot{\gamma}\dot{F}^f = 0$, $F^f \leq 0$,

$$\begin{aligned} N &= \frac{\partial F^f}{\partial \sigma^f} = -\frac{\partial F^f}{\partial \bar{q}^f} \\ &= \text{sign}((\sigma - \bar{q}) : \vec{p}\vec{p})\vec{p}\vec{p} \end{aligned} \quad (25)$$

${}^4H^f$ is the kinematic hardening tensor and ${}^4\bar{q}^f$ is the backstress for the fibre respectively in Eq. (23). The tensor N denotes the direction of the plastic flow as given in the (25).

In Voigt matrix notation, ${}^4H^f$ is represented as

$$\underline{H}^f = \begin{pmatrix} H & 0 & 0 \\ 0 & H & 0 \\ 0 & 0 & H/2 \end{pmatrix} \quad (26)$$

where H is the kinematic hardening modulus of the fibre. The yield function F^f for the fibre is expressed as (24). In this expression, the first term gives the difference of the mechanical stress σ^f and the backstress \bar{q}^f in the longitudinal direction of the fibre with the help of the longitudinal projection vector \vec{p} which is defined as $\vec{p} = \cos\theta\vec{e}_x + \sin\theta\vec{e}_y$, with θ representing the angle between the fibre direction and the machine direction of the paper. In this way, only the plastic deformation caused by the stresses in the longitudinal direction of the fibres is taken in account.

The yield function in (24) also depends on the yield stress for the particular fibre. To simulate the hygroscopic response, the yield stress is postulated as a piece wise linear function of the moisture content such that it decreases with an increase of the moisture content.

$$\sigma_y = \begin{cases} \sigma_{y0}(1 - \frac{\chi}{\chi_w}), & \text{if } \chi < \chi_w \\ 0 & \text{if } \chi \geq \chi_w. \end{cases} \quad (27)$$

Here, σ_{y0} is the maximum yield stress corresponding to a vanishing moisture content. χ_w is the moisture content at which the yield stress vanishes.

In the bonded regions, the hygro-elasto plastic response of each fibre is computed individually and the resulting force vector and stiffness contribution from each of the fibres is added for the particular finite element. The periodic unit cell containing the fibrous network is discretized with a regular finite elements mesh and solved with a non linear incremental-iterative standard finite element method using the Newton-Raphson scheme. In order to update the stresses in the linear kinematic hardening model, a return mapping algorithm based on trial states is adopted. For the solution procedure, the expressions for the plastic multiplier and the consistent tangent operators are required which are derived in the appendix ((71) and (73)).

The longitudinal behavior in compression and the transverse behavior of the fibres both in tension and compression are assumed to follow a hygro-elastic constitutive behavior. This is justified by the fact that the irreversibility is attributed to tensile stresses in the longitudinal direction of the fibres according to the fibre segment activation mechanism explained before.

3.3 RESULTS AND DISCUSSIONS

In this section, the different phases of the manufacturing process of paper followed by its exposure to a wetting-drying cycle is described. This entails the irreversible shrinkage of the simplified and complex fibrous networks, which is investigated as a function of the micro-structural properties of the fibres and the overall properties of the network. For this purpose, the constitutive model discussed in the previous section is used at the fibre level within a finite element context.

3.3.1 Modeling the effects of manufacturing constraints

During the manufacturing process of paper especially the hand sheets, the wet pulp is initially dried under tension and then the restraints are removed. This is followed by free drying. In the current work, this sequential drying process in manufacturing, followed by the subsequent moisture cycle on the paper sheets can be represented schematically for a paper sheet by the diagram given in Fig. 26. Here χ_{low} is the lowest moisture content reached, in the as-manufactured sheet as well as at the end of the moisture cycle, χ_{high} is the highest moisture content at the start of fibre bonding and also during the moisture cycle, χ_{cons} is the moisture content until which the fibre is dried under restraint, which is subsequently removed for lower moisture contents. The moisture content range is chosen in accordance with the work performed by Larsson and Wagberg [37] with $\chi_{low}=0.038$, $\chi_{cons}=0.08$, $\chi_{high}=0.12$ and $\chi_w=0.13$.

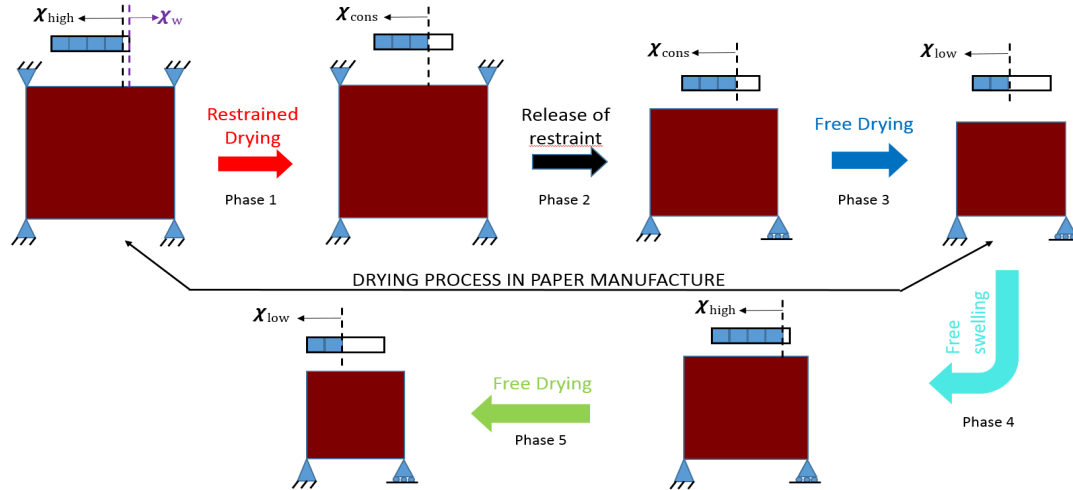


Figure 26: Schematic diagram of the entire paper making process and subsequent exposure to a wetting-drying cycle.

The paper sheet initially is restrained dried leading to the development of plastic strains in the fibres. Next, the stress is gradually released by removing the restraints in the second phase (release of restraint - phase 2). This causes the paper to shrink in the direction in which it was previously restrained. Thereafter, it is dried freely (phase 3) which results in more shrinkage of the fibres thereby concluding the manufacturing process (free drying). In the manufacturing process, even though there is no application of external stress on the paper sheet, internal stress (back stress) exists in the fibres due to the plastic deformation undergone by them in restraint drying.

Thereafter, the paper sheet is subjected to a moisture cycle ($\chi_{low} - \chi_{high}$ and vice-versa). This corresponds to a uniform increase of moisture without any restraint upon exposure to a humid environment (free swelling/Rewetting - phase 4). As the moisture content is increased, the yield stress decreases, the backstresses are sufficient enough to drive plastic yielding (back flow) even if there is no externally applied stress. Subsequently, it is dried freely causing again shrinkage (Free drying/Re-drying - phase 5).

3.3.2 Input parameters for fibres and networks

In this study, the periodic unit cells (as described earlier) with coverages $c=0.25, 0.5, 1, 1.5, 2.0$ and 5.0 will be analyzed. Here, the material parameters chosen are different in comparison to the previous chapter because a different model is adopted to gain insight into the sheet-scale irreversible strains. Following the work performed by Bosco, Peerlings, and Geers [7] and adopting its values for all the mentioned parameters, the longitudinal elastic stiffness of the fibre is taken as $E_l=5.176 \times 10^2 \sigma_{y0}$, whereas in the transverse direction, $E_t=E_l/6$ (Strömbro and Gudmundson [68]). The shear modulus is taken as, $G=E_l/10$. The hygro-expansive coefficients along the longitudinal and transverse directions are given by $\beta_l=0.03$, $\beta_t=20\beta_l=0.6$ (Niskanen [45]). The in-plane Poisson ratios are, $\nu_{lt}=0.3$ and $\nu_{tl}=0.05$ (Schulgasser and Page [63]). The kinematic hardening modulus adopted in the plasticity model presented earlier is $H=100\sigma_{y0}$. All of the above quantities are assumed to be constant irrespective of the moisture content. The numerical simulations are performed

with a uniform mesh size $h=l/200$.

Now, depending on the number of fibres n generated in the unit cell, a coverage c is defined as the ratio of the total area occupied by all fibres and the area of unit cell. It is related to the grammage g via

$$g = c\rho_f t$$

where ρ_f is the density of fibres and t is the thickness of the fibres. For example, considering a density of the fibres $\rho_f=1500\text{kg/m}^3$ ([45]), a thickness $t=10\mu\text{m}$ and a coverage $c=1.0$ as used in the results section, the corresponding grammage is 15g/m^2 . As the coverage increases, with density and thickness remaining constant, the grammage scales linearly with the coverage as indicated by the above relation.

3.3.3 Simplified meso-scale network

The fibrous network is first modeled using a periodic network consisting of two perpendicular families of equidistant fibres as seen in Fig. 22c using a plane stress model, see also (Bosco, Peerlings, and Geers [7]). This is the same network model as used by Bosco, Peerlings, and Geers [7] but solved numerically. The irreversible behavior of a meso-scale network with coverage $c=0.5$,

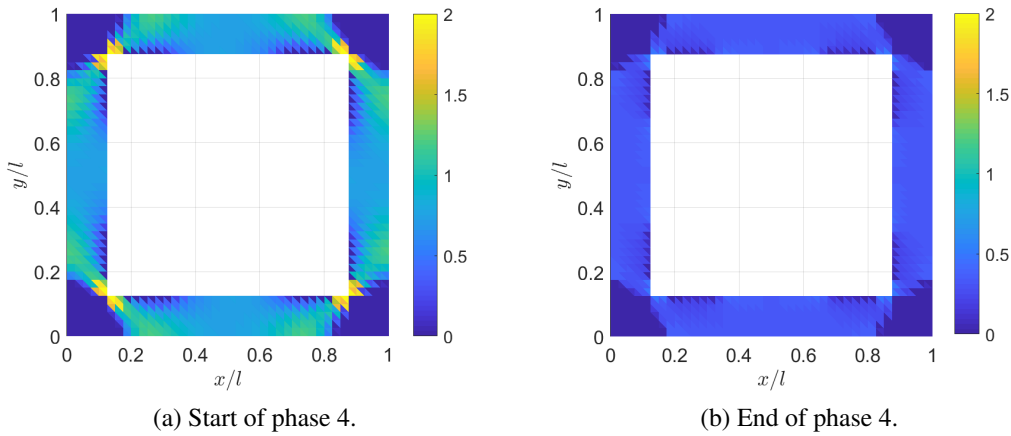


Figure 27: Normalized local plastic strain (longitudinal component) distribution ${}^p e_l / (\beta_l \Delta\chi)$, in meso-scale network of coverage, $c=0.5$.

consisting of two perpendicular fibres, when subjected to the papermaking and subsequent moisture cycle, is computed numerically using the kinematic hardening model described previously. In Fig. 27a, it can be noticed that at the end of the paper manufacturing process, the dried-in strains or plastic strains, ${}^p e_l^f$ (normalized by $\beta_l \Delta\chi$, where $\Delta\chi = \chi_{high} - \chi_{low}$, have developed in the idealized paper network. After subjecting it subsequently to an increase in moisture content, these dried-in strains (normalized by $\beta_l \Delta\chi$) are largely released as depicted in Fig. 27b. Note that these plastic strains do not develop in (and are not subsequently released from) the bonded regions but rather in the free-standing parts of the fibres. In these free standing fibre regions, the dried-in strains (plastic strains) or corresponding backstresses are initially developed at the end of restrained drying

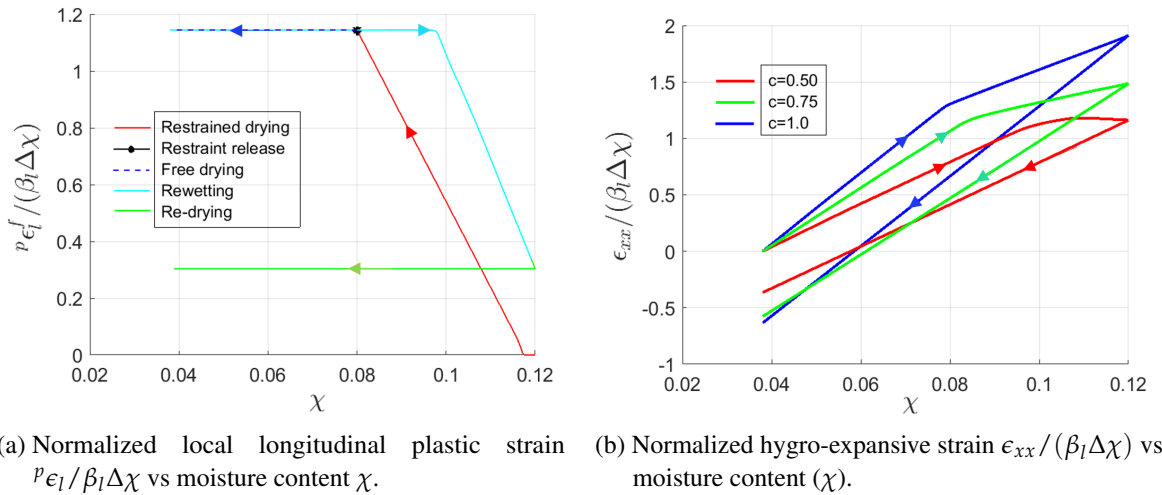


Figure 28: History of the normalized local plastic strain (longitudinal component) in the free standing fibre region of the network and the normalized macroscopic hygro-expansive strain $\epsilon_{xx} / (\beta_l \Delta\chi)$ during the moisture cycle ($\chi_{low} - \chi_{high}$ and vice-versa) for different coverages of the meso-scale network. Note: Curves have been shifted such that $\epsilon_{xx}=0$ corresponds to as-produced sheet in (b)

as can be seen in Fig. 28a. Thereafter, the restraint is released at a constant moisture content and then it is dried freely. In both of these phase, the dried -in or plastic strains remain constant as there is no restraint to produce stress to cause plastic yielding. As the network is subjected to a moisture increase (in the moisture cycle), the yield stress decreases but the back stresses cause yielding in reverse direction leading to release of these dried-in strains. Finally, when the moisture is decreased, the yield stress increases and there is no plasticity evolution. Therefore, the plastic strain remains constant.

At the macro-scale, this local behavior of the fibres results in a global release of strain or permanent strain as depicted in Fig. 28b for the three values of the coverage. In the initial phase of moisture cycle when the moisture content increases, there is a change in the slope (a kink is observed) after a certain moisture content. At this point, the plastic strains start to get released until the moisture content starts to decrease. This occurs for the meso-scale network of all coverages. Also, we can notice, that as the coverage increases, the irreversible shrinkage also increases in magnitude. This computed response is in agreement with the findings by Bosco, Peerlings, and Geers [7] if not quantitatively.

However, in reality the networks are complex and have high coverage (more bonded regions). Therefore, they have different magnitudes of irreversible strains which are discussed in the next subsection.

3.3.4 Complex networks

In this section, the numerical model is exploited for more complex 2D fibrous networks. Random isotropic fibrous networks are generated for coverages $c = 0.5, 1.0, 2.0$ and 5.0 . The local plastic strains in the networks are computed at the end of the manufacturing process. Fig. 29 illustrates the corresponding distribution of plastic strains normalized with $\beta_l \Delta\chi$. When these networks are next

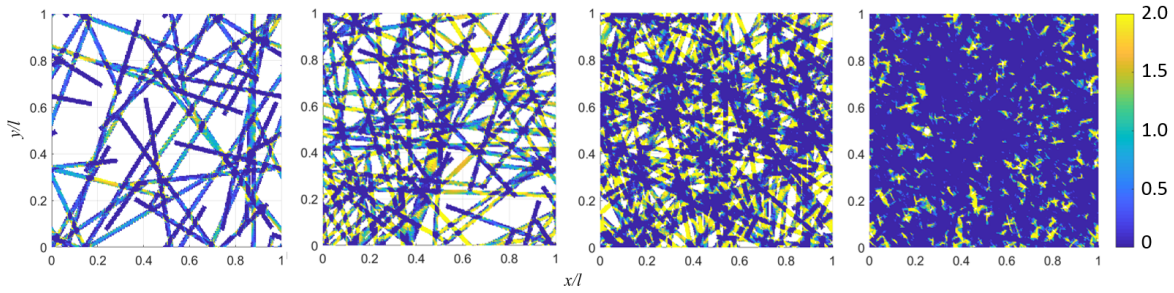


Figure 29: Normalized local longitudinal plastic strain distribution ${}^p\epsilon_1^f / (\beta_l \Delta\chi)$ in networks with coverage, $c=0.5, 1.0, 2.0$ and 5.0 (left to right) after paper is manufactured.

subjected to a moisture cycle χ_{low} to χ_{high} and vice-versa, the plastic strains are partly released as can be observed in Fig. 30. At the macroscopic scale, this release in the networks is observed as an overall irreversible shrinkage as illustrated in Fig. 31. Fig. 29 reveals that the area of plastically

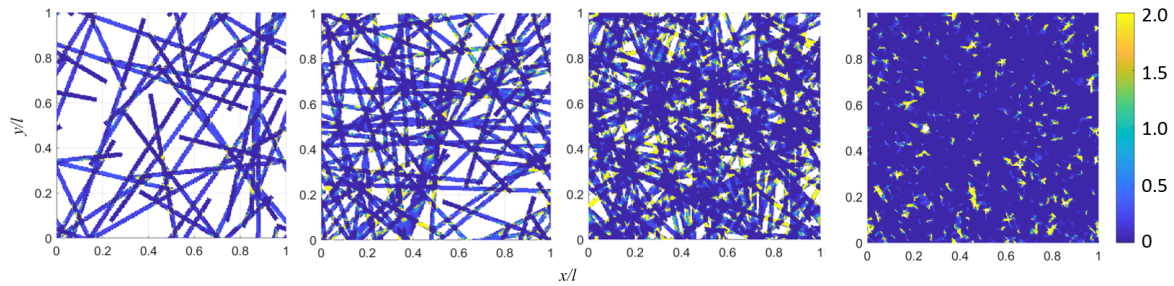


Figure 30: Normalized local longitudinal plastic strain distribution ${}^p\epsilon_1^f / (\beta_l \Delta\chi)$ in networks with coverage, $c=0.5, 1.0, 2.0$ and 5.0 (left to right) after release of strains.

deformed fibre segments increase as the coverage increases from $c=0.5$ to $c=2.0$, followed by a decrease for higher coverages, e.g. $c=5.0$. At the macro-level, the irreversible shrinkage also increases from $c=0.5$ to $c=1.0$ and decreases thereafter as noticed in the hygro-expansive strain plots (normalized with $\beta_l \Delta\chi$) in Fig. 31. Additionally, at the macro-scale, the release of these irreversible strains in the moisture cycle are not observed as a kink anymore like in the meso-scale networks but as a smoother transition. Despite the fact that a linear hardening law was used, which in the highly idealized model of Bosco, Peerlings, and Geers [7] resulted in a bi-linear hygroscopic network response, the response of the present random network is nonlinear, as is also observed in experiments. This is due to the heterogeneity of the network, as a result of which the plastic strain release is initiated at different moisture contents in different fibre segments. As reported in the experiments [43], the irreversible strains in MD for paper of grammage $g=149\text{g/m}^2$ (paper ID-4) of around $\epsilon_{irr} = 1.4 \times 10^{-3}$. In comparison, the value of irreversible deformations predicted by the numerical model at $c=1.0$ is around 9.2×10^{-4} but at $c=5.0$ it reduces to 1.1×10^{-4} . One of the possible reasons could be that the model does not take into account the plasticity in compression which occurs more at higher coverage like $c=5.0$, thereby leading to negligible irreversible strains.

To establish that the irreversible strain is stemming from the free standing fibre parts, the hygro-mechanical response of networks with a low coverage $c=0.5$ and $c=1.0$ is computed by allowing for plasticity only in the free standing part of the fibres or conversely only in the bonded part of fibres.

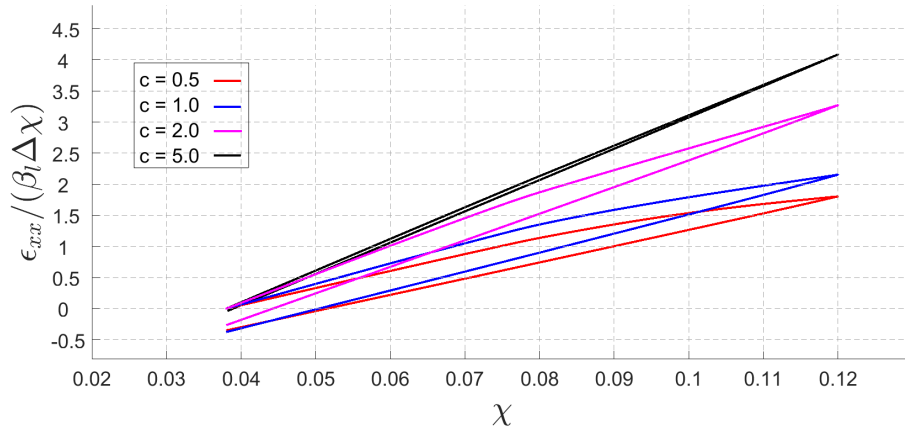


Figure 31: Normalized macroscopic strains $\epsilon_{xx}/(\beta_l\Delta\chi)$ in the networks subjected to a moisture cycle after manufacturing.

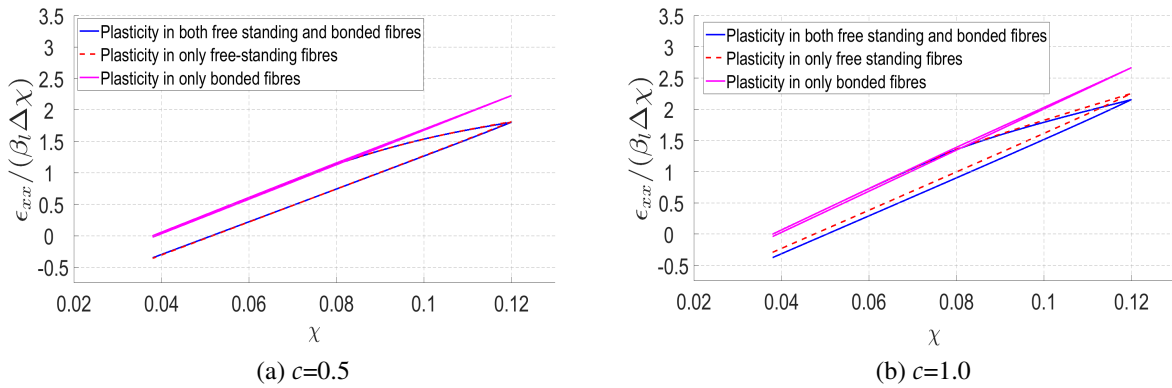


Figure 32: Hygro-expansive strain, ϵ_{xx} normalized with $\beta_l\Delta\chi$ in the fibrous network 1 obtained by numerical model.

The corresponding results for the normalized macro-level hygro-expansive strain, highlighting the irreversible strains, are provided in Fig. 32. Clearly, at the sheet-level, the irreversible shrinkage depends on plasticity occurring in the free-standing part of fibres in the network, as the response obtained with plasticity only in the free standing parts is virtually identical to that of the reference network.

On the other hand, when only the bonded parts of fibres in the network are subjected to plasticity, the irreversible shrinkage at the sheet-level becomes negligible. This further confirms the finding that the observed irreversibility phenomenon is essentially due to dried-in strains in the free standing fibre regions.

So far, we showed results for a single network with coverage $c=0.5, 1.0, 2.0$ and 5.0 . The simulations have been repeated for five realizations at each coverage, still using randomly generated isotropic complex networks. The irreversible shrinkage is defined as difference of the hygro-expansive strain, ϵ_{xx} at the beginning of moisture cycle and end of moisture cycle. The magnitude

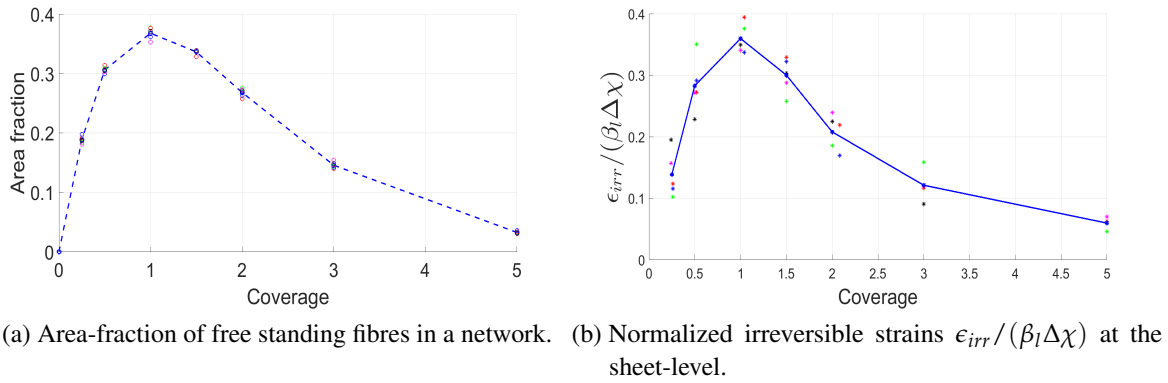


Figure 33: Plots of area fractions and irreversible shrinkage for five network realizations of different coverages.

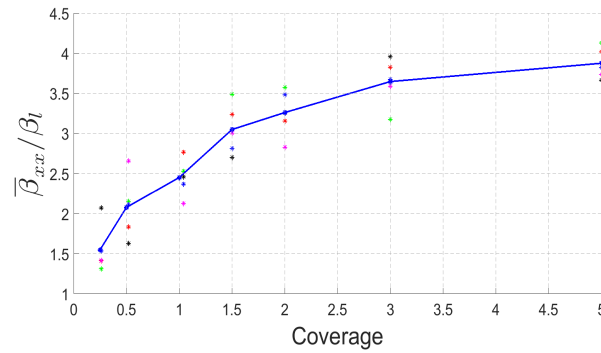


Figure 34: Coefficient of effective hygro-expansion normalized with β_l at the sheet-level for different coverages of complex networks.

of the irreversible shrinkage ϵ_{irr} normalized with $(\beta_l \Delta\chi)$ observed at the sheet-level for each of these networks and the area fraction distribution of free-standing fibre parts are depicted in Fig 33. It is observed in Fig. 33b that as the coverage increases, the irreversible shrinkage increases until a coverage $c=1$ with a subsequent decrease until coverage, $c=5.0$. This dependency is closely related to the area fraction of the free standing part of fibres which peaks in Fig. 33a at $c=1.0$. This confirms that the free standing fibre parts in the network are responsible for the irreversible behavior of the networks upon exposure to a moisture cycle. In the restrained drying, the bonded segments of the fibres subjected to a mutual compression from the its constituting fibres, do not develop sufficient stress to generate dried-in strains.

With higher coverages ($c > 2.0$), the bonds also increase in area fraction while the fraction of free standing fibre parts decreases, resulting in less plastic strains as already noticed in Fig. 29. Upon exposure to a moisture cycle, this causes a lower irreversible shrinkage.

Additionally, as the fraction of bonded regions increases with the coverage, there is also more expansion of the network for a given change in moisture content. Therefore, the effective macroscopic coefficient of hygroscopic expansion also increases in magnitude with an increase in coverage as

observed in Fig. 34.

The average time taken for a single simulation of network of each coverage $c=0.25-5.0$ are in the range of 16-85 hrs.

3.4 CONCLUSIONS

In the present chapter, the dependency of the (experimentally observed) irreversible shrinkage at the sheet-level on the microstructural parameters in a fibrous network of paper is studied. The irreversible shrinkage is associated with microstructural dried-in strains caused by the restrained drying during the manufacturing process. Such dried-in strains get subsequently released upon wetting, e.g. during printing operations. For this study, ribbon shaped fibres are randomly generated. Using a standard homogenization approach, the paper consisting of a fibrous network is represented as a periodic RVE. Relying on the hypothesis that the fibre segment activation mechanism is the physical cause of these permanent deformations in paper, it is assumed that the irreversible shrinkage occurs in the longitudinal direction of the fibres.

A constitutive model implementing kinematic hardening plasticity is adopted to model the irreversibility in the longitudinal direction of the fibres in the network. This allows modeling the irreversible deformation in paper subjected to moisture change with no applied external stresses, reflecting the real conditions to which the paper is subjected during manufacturing with restraint. The key findings of the current chapter are:

1. The magnitude of the irreversible shrinkage at the macro-scale in the fibrous network model is a function of the coverage, i.e. density, of the network. Initially it increases with coverage until $c=1.0$ but subsequently decreases to small values at higher coverages, $c=5.0$.
2. The irreversible phenomenon directly relates to the area fraction of the free standing parts of fibres in the network. A higher coverage in network causes a reduction in free standing fibres, which further results in a decrease of irreversible shrinkage.
3. The non-linear response at the macro-scale of the network during the moisture cycle is captured even with a linear kinematic hardening model.

One of the limitations of the present work is the assumption of full kinematical bonding of fibres in the bonded regions. This may influence the observed decrease of irreversible shrinkage predicted by the model at higher coverages. The present work may be extended by the relaxing the kinematic constraints at the bonds.

In the future, the material parameters E_l, E_t, G_{lt} could be modelled as a non-linear functions of the moisture content of the fibres. Also, the model does not predict irreversible strains for coverages beyond 5.0. In our current formulation, the rate independent model generates plastic strains only in tension which can be extended to compression in a future task. This would entail generation of different magnitude of plastic strains at the local fibre level and further permanent deformation. Additionally, incorporating relaxation of the assumption of the rigid bonds (allowing relative displacements between fibres in bond) in the model would be interesting to further compute the

irreversible strains at higher coverage too.

Experimentally, the moisture cycles do not lead to total release of the initially dried in strains. There may be other phenomena responsible for such irreversible strains observed at the macroscale which may be further explored.

Furthermore, in the current study, the release of the dried-in strains is represented as quasi-static phenomenon. As a next step, a suitable rate-dependent model can be adopted to study the influence of time on the irreversible shrinkage in fibrous networks.

MODELING THE EFFECT OF CREEP IN PAPER FIBRES UNDER THE INFLUENCE OF EXTERNAL LOADING AND CHANGES IN MOISTURE

Paper is composed of a network of fibres at the micro-scale. When subjected to external loading or variations in moisture over different time scales, changes in strain that are non-linear with respect to time are observed at the sheet level. In order to investigate this time-dependent behavior of paper, a creep power law model is implemented within a finite element approach at the level of single paper fibres. The rate-dependent model for single fibres adequately captures experimental results taken from the literature. With the identified model at the level of single fibres, the time-dependent hygro-mechanical response is upscaled towards the paper network-scale. To this end, ribbon shaped fibres are generated randomly to form a periodic network represented by a unit cell. The network-scale response, emerging from the rate-dependent fibre model, demonstrate the ability to predict the response of networks subjected to relaxation at a constant moisture level. The model also reproduces the release of irreversible strains upon exposure of a previously constrained dried paper to a moisture cycle. Based on the study of these computational results, a better understanding is achieved regarding the influence of mechanical and rate-dependent properties of single fibres on the hygro-expansion of complete fibre networks and in particular of paper sheets.

Keywords: Fibrous network, creep hygro-mechanics

4 This chapter is based on: P. Samantray, R.H.J. Peerlings, T.J. Massart, M.G.D. Geers, 2019. *Studying the effect of creep in paper fibres under the influence of an external loading and changes in moisture*. In preparation.

4.1 INTRODUCTION

Paper is a complex material consisting of elongated, ribbon-shaped fibres exhibiting an anisotropic behavior in nature. Exposure to changes in moisture content causes changes in the shape of fibres leading to the development of hygroscopic strains. Such hygroscopic strains in individual fibres are 20 times higher in the transverse direction as compared to the longitudinal direction [45]. More importantly, it has been also observed that deformations in paper present a time-dependent character.

As observed earlier [43], paper dried under restraint, develops semi-permanent dried in strain that gets released upon subjecting the paper to a moisture cycle. In view of the rate-dependent response of paper, the magnitude of the dried-in strains generated in the manufacturing process and their subsequent release become time-dependent as well. This for instance affects printing operations, during which the printed paper may develop waviness or deformations, depending on the rates of absorption and evaporation of the water contained in water based inks. Rate dependency may also affect subsequent stages after printing, when the paper is exposed to ambient conditions, during which the humidity varies over a period of time, possibly entailing macroscopic curls at the sheet-level.

Investigations of the rate-dependent behavior of paper at different scales have been reported in the literature. Some of the early experiments were performed on single fibres, allowing to analyze creep at a constant moisture content under tensile loading [28, 32, 64]. It was observed in these experiments that as single fibres are dried under tension, an increase in the strains occurs. This behavior was explained by Page and Tydemann [50]. At the micro-level, the microfibrils in the fibres form a helical structure. During drying, a reduction in the diameter of a fibre occurs, but the length of the microfibrils and the number of revolutions along the fibre are preserved. This results in a slight increase of the fibre length. Hence, an increasing in strain was reported in experiments performed on single fibres after removal of water, subjected to a constant load. Later, this behavior was also observed for single fibres subjected to cyclic humidity [64]. Moreover, single fibres were also found to exhibit creep recovery upon removal of the load [64]. The influence of the presence of hemicellulose on creep was also investigated.

At a much larger scale, tensile experiments performed on hand sheets revealed creep as well [11]. The time-dependent response of sheets of paper was also investigated to find high creep strain rates in cyclic humidity compared to constant humidity [13], and by developing a method for quantifying mechano-sorptive creep [51]. It was observed that the creep strain rate in single fibres is significantly higher than in paper sheets [16]. Furthermore, inter-fibre breaking of bonds was also observed during paper creep [50]. A linear relation was found between the creep strain rate under cyclic humidity and constant humidity for both fibres and paper sheets [57].

For an increase in moisture content of paper, the creep is accelerated to a higher value, often known as mechanosorptive creep or accelerated creep [13]. This is detrimental to the dimensional stability of paper, either used in packaging or other applications. Many works have been performed to establish a physical understanding for the occurrence of this phenomenon in paper sheets, fiberboards and wood [4, 16, 19, 23, 29–31, 42, 58, 73]). These works focused in identifying the parameters that cause the mechanosorptive creep like humidity cycling, bonding of fibres, redistribution of the stresses in the network, fibril angle and slip planes and obtaining a mechanosorptive

creep limit as well as developing constitutive models for it.

Several mechanisms were invoked to explain the creep behavior of paper. A moisture induced stress concentration mechanism [23] as well as physical mechanisms at all structural levels of paper, i.e. creation of free volume, microcompressions in inter-fibre bonds, anisotropic swelling and change in fibril angle [24] and [25] were all used to explain mechanosorptive creep.

In order to gain insight into the rate-dependent response of paper, it is essential to capture the main physical processes at play in a model. Earlier computational attempts were made based on Cox's network model [17], further extended to account for hygro-expansion, creep and bonds (Alfthan [3]). Later, fibre kinks were incorporated allowing the model to capture the experimental response in compression and tension (Strömbro and Gudmundson [68]). These models also considered anisotropic fibre distributions and moisture dependent material properties (Strömbro and Gudmundson [68]). Other works performed earlier were concerned with establishing a relationship between the micro-structural and the macroscopic responses of fibrous network [2, 5, 15, 70, 76].

Some of the recent works on modeling fibrous materials described the mechanical and thermal response of the network [20, 36, 66]. Some contributions addressing the mechanical response of paper, incorporated the role of the bonds [53, 63, 67]. Recent work focussed on the modeling of hygro-mechanical response of paper (Bosco, Peerlings, and Geers [8]).

Our main interest in this chapter is in rate and creep effects in the irreversible hygro-mechanics of paper sheets and in identifying the fibre and network properties that affect the creep response at sheet-scale. The present contribution extends recent work by Bosco, Peerlings, and Geers [8] by incorporating the creep response in two-dimensional models of random fibre networks using a rate-dependent plasticity model at the fibre-scale. This allows to investigate to which extent microstructural parameters like fibre properties and coverage influence the macroscopic creep response, i.e. the creep strain rates at the network-level. Also, the effect of rate dependency on the release of irreversible strains upon moisture cycling of restrained dried paper is studied.

To achieve these goals, a rate-dependent creep model based on a power law is formulated at the fibre-scale. One of the main features of the model is the implementation of the creep behavior in the longitudinal direction of the fibre as suggested by the fibre segment activation mechanism, as reported earlier in chapter 3 (Samantray, Peerlings, Massart, and Geers [62]). First, the response is computed for single fibres and compared with available experimental results. The identification of the creep parameters of the model is based on single fibre results taken from the literature. Thereafter, the fibre-scale numerical model is used to obtain the rate-dependent response of the fibre networks subjected to constant moisture and cyclic moisture conditions under the presence of tensile loads. Using a random fibre network contained in a periodic cell and incorporating the rate-dependent constitutive model in a finite element discretization of the network, the overall creep response is determined.

The chapter is organized as follows: In Section 2, the constitutive model used at the scale of the single fibres is described. The selected rate-dependent model is explained in Section 3. The calibration of the single fibre constitutive model parameters is performed in this section based on the results of single fibres tests presented in the literature. These results are next extended to the

fibrous network-scale in Section 4. Finally, the conclusions are given in Section 5.

Throughout this contribution, the following notations are used. Scalars, vectors and tensors are denoted by a , \vec{a} and \mathbf{A} respectively. For Cartesian tensor and vector products, the following equivalent notations are used, with Einstein's summation convention on indices: $\mathbf{A}:\mathbf{B}=A_{ij}B_{ji}$ with $i=x,y,z$ for the global reference system and $i=l,t,z$ for the local reference system. The Voigt notation used to represent tensors and tensor operations in a matrix format is as follows: \underline{a} and $\underline{\mathbf{A}}$ denote a column matrix and a matrix of scalars respectively. Matrix multiplication is denoted as $(\underline{\mathbf{A}} \underline{a} = A_{ij}a_j)$.

4.2 FIBRE SCALE CONSTITUTIVE MODEL

4.2.1 Fibre model

A single fibre-scale model is proposed to incorporate plastic strain rate effects when a fibre is subjected to a tensile stress under a given moisture content. A partition of the total strain tensor \mathbf{e}^f is considered according to

$$\mathbf{e}^f = {}^e\mathbf{e}^f + {}^c\mathbf{e}^f + {}^h\mathbf{e}^f \quad (28)$$

with ${}^e\mathbf{e}^f$, ${}^c\mathbf{e}^f$ and ${}^h\mathbf{e}^f$ representing the elastic, creep and hygroscopic contribution respectively.

The hygroscopic strain tensor in the fibre, ${}^h\mathbf{e}^f$ is expressed as

$${}^h\mathbf{e}^f = \underline{\boldsymbol{\beta}}^f \Delta\chi \quad (29)$$

where χ is the current moisture content, $\Delta\chi = \chi - \chi_{ref}$ is the change of moisture content with respect to the reference moisture content, χ_{ref} and $\underline{\boldsymbol{\beta}}^f$ is the fibre hygro-expansivity tensor; in Voigt notation relative to the local frame of reference (l,t,z) as shown in Fig. 35, it is given by

$$\underline{\boldsymbol{\beta}}^f = \begin{pmatrix} \beta_l \\ \beta_t \\ 0 \end{pmatrix} \quad (30)$$

For the mechanical response of the fibre, a plane stress condition in the z-direction (out of plane direction, along fibre thickness) is assumed. The elasticity law for the fibre is expressed as

$$\boldsymbol{\sigma}^f = {}^e\mathbf{e}^f = {}^4\mathbf{D}^f : (\mathbf{e}^f - {}^c\mathbf{e}^f - \underline{\boldsymbol{\beta}}^f \Delta\chi)$$

where $\boldsymbol{\sigma}^f$, ${}^4\mathbf{D}^f$ are the stress tensor and the elasticity tensor of the fibre respectively. In Voigt notation (with respect to the local basis), the latter is represented as

$$\underline{\mathbf{D}}^f = \begin{pmatrix} \frac{E_l}{(1-\nu_{lt}\nu_{tl})} & \frac{E_l\nu_{tl}}{(1-\nu_{lt}\nu_{tl})} & 0 \\ \frac{E_t\nu_{lt}}{(1-\nu_{lt}\nu_{tl})} & \frac{E_t}{(1-\nu_{lt}\nu_{tl})} & 0 \\ 0 & 0 & G_{lt} \end{pmatrix} \quad (31)$$

The fibre elasticity being anisotropic in Eq. (31), E_l and E_t denote the elastic moduli in the longitudinal and transverse direction respectively. G_{lt} represents the in-plane shear modulus, ν_{lt} and ν_{tl} are

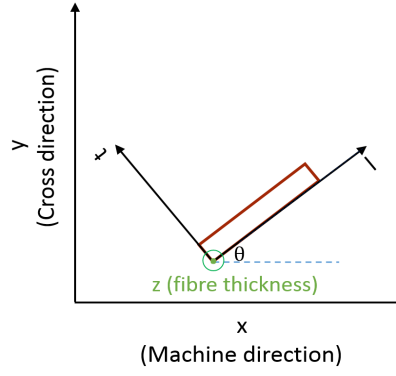


Figure 35: The local and global coordinate axes.

the in-plane Poisson ratios.

In order to describe the time-dependent plasticity effects associated with mechanical loading or changes in moisture content, a non-linear creep law is adopted. The underlying mechanism which we envision is the fibre segment activation mechanism: the microfibrils in the fibre wall tend to align themselves towards the fibre axis upon application of a tensile load or restrained drying of fibres. Internal stresses or strains thereby develop in the fibres, which may later be released upon exposure to a moisture cycle. The plastic deformation and internal stress due to the realignment of microfibrils was modeled by Samantray, Peerlings, Massart, and Geers [62] by a kinematically hardening rate-independent plasticity model. Here, we extend this modeling with a rate dependence. The rate-dependent plasticity model is based on a power law and defines the creep strain rate tensor ${}^c\dot{\epsilon}^f$ according to the flow rule

$${}^c\dot{\epsilon}^f = \dot{\gamma} \mathbf{N} \quad (32)$$

where $\dot{\gamma}$ determines the magnitude and \mathbf{N} the direction of the plastic flow. The former is given in terms of the stress tensor σ^f and the backstress \bar{q}^f by the power law

$$\dot{\gamma} = \frac{\gamma_0}{\tau} \left\{ \frac{(\sigma^f - \bar{q}^f) : \vec{p}\vec{p}}{\sigma_y} \right\}^{\frac{1}{m}} \quad (33)$$

where γ_0 is a constant characteristic strain, τ is a characteristics time, \vec{p} a unit vector parallel to the fibre's longitudinal axis, σ_y the moisture dependent yield stress and m the rate sensitivity exponent. In the limit of $m \rightarrow 0$, the model reduces to a rate-independent plasticity model. The projection on the longitudinal vector \vec{p} implies that only normal stress in longitudinal direction drives the evolution of creep strain. Consistent with that, the direction of plastic flow, given by the tensor \mathbf{N} which is defined as

$$\mathbf{N} = \text{sign}((\sigma^f - \bar{q}^f) : \vec{p}\vec{p}) \vec{p}\vec{p} \quad (34)$$

The double product with $\vec{p}\vec{p}$ allows projecting the stress and backstress on longitudinal direction in consideration to enforce the rate-dependent model. These are defined as $\vec{p} = \cos\theta \vec{e}_x + \sin\theta \vec{e}_y$ where θ is the angle between the longitudinal fibre direction and the machine direction of the paper.

The backstress \bar{q}^f which models the internal stresses in the fibre due to fibre activation, evolves with plastic straining according to the evolution law

$$\bar{q}^f = -{}^4\mathbf{H}^f : \bar{\xi}^f \quad (35)$$

where ${}^4\mathbf{H}^f$ is the 4th order kinematic hardening moduli which we define in Voigt notation as

$$\underline{\underline{H}}^f = \begin{pmatrix} H & 0 & 0 \\ 0 & H & 0 \\ 0 & 0 & H/2 \end{pmatrix} \quad (36)$$

and $\bar{\xi}^f$ is the strain like internal variable which follows the evolution law

$$\bar{\xi}^f = -\gamma \mathbf{N} \quad (37)$$

Both quantities are equal to zero in the initial, relaxed state of the fibre.

The yield stress σ_y , finally, which appears in the denominator in the power law Eq. (33), depends solely on the moisture content χ , according to the bilinear law

$$\sigma_y = \begin{cases} \sigma_{y0} \left(1 - \frac{\chi}{\chi_w}\right), & \text{if } \chi < \chi_w \\ 0 & \text{if } \chi \geq \chi_w. \end{cases} \quad (38)$$

where σ_{y0} is the yield stress in the fully dry state ($\chi = 0$) and χ_w represents a moisture content at which the strength of the fibre is fully gone and no energy can hence be stored in it anymore.

4.2.2 Implementation aspects

A return mapping algorithm is used to solve the rate-dependent creep model at the fibre-level. It is represented as

$$\sigma^{f,t+\Delta t} = \sigma_{trial}^{f,t+\Delta t} - \Delta\gamma {}^4\mathbf{D}^f : \mathbf{N} \quad (39)$$

$$\bar{q}^{f,t+\Delta t} = \bar{q}_{trial}^{f,t+\Delta t} + \Delta\gamma {}^4\mathbf{H}^f : \mathbf{N}, \quad (40)$$

$$F_{trial}^{f,t+\Delta t} = \left(\frac{\sigma_{trial}^{f,t+\Delta t} - \bar{q}_{trial}^{f,t+\Delta t} : \vec{p}\vec{p}}{\sigma_y} \right) \text{sign} \left(\frac{(\sigma_{trial}^{f,t+\Delta t} - \bar{q}_{trial}^{f,t+\Delta t}) : \vec{p}\vec{p}}{\sigma_y} \right) \quad (41)$$

$$\Delta^c \epsilon^f = \Delta\gamma \mathbf{N} \quad (42)$$

$$\Delta \bar{\xi}^f = -\Delta\gamma \mathbf{N} \quad (43)$$

where $\sigma_{trial}^{f,t+\Delta t}$ and $\bar{q}_{trial}^{f,t+\Delta t}$ are the trial stress and trial back stress tensors in the fibres respectively. Upon further derivation (see Appendix (87)), the equation allowing to compute the plastic multiplier is derived as

$$G(\gamma) = \Delta\gamma - \frac{\gamma_0 \Delta t}{\tau} [F_{trial}^{f,t+\Delta t} - \vec{p}\vec{p} : ({}^4\mathbf{D}^f + {}^4\mathbf{H}^f) : \vec{p}\vec{p} \Delta\gamma]^{\frac{1}{m}} = 0 \quad (44)$$

Since the creep strain evolution is based on a power law, a non-linear equation is obtained for the computation of the plastic multiplier at the local fibre-level. A Newton-Raphson scheme is therefore used to solve the above equation.

The return mapping scheme is implemented at the local level of fibres in the fibrous network. The discretized set of equilibrium equations for the complex unit cell is solved within a non-linear incremental-iterative (global) Newton-Raphson scheme by means of the standard finite element method for the current work. This requires deriving the material tangent modulus at the fibre Gauss points. The material tangent modulus is also computed after derivation (see Appendix (93)) as

$${}^4D_{ep}^{f,t+\Delta t} = {}^4D^f - \frac{AA}{1 + AA \mathbf{N}_{trial} : ({}^4D^f + {}^4H^f) : \mathbf{N}_{trial}} {}^4D^f : \vec{p}\vec{p} \vec{p}\vec{p} : {}^4D^f \quad (45)$$

$$AA = \frac{\gamma_0 \Delta t}{m \tau \sigma_y} \left[\frac{(\sigma_{trial}^{f,t+\Delta t} - \bar{q}_{trial}^{f,t+\Delta t}) : \mathbf{N}_{trial} - \Delta \gamma \mathbf{N}_{trial} : ({}^4D^f + {}^4H^f) : \mathbf{N}_{trial}}{\sigma_y} \right]^{\frac{1}{m}-1}$$

4.3 IDENTIFICATION OF SINGLE FIBRE PARAMETERS FROM EXPERIMENTAL TESTS

Various experimental tests on single fibres were reported in the literature. Creep tests were performed on single, wetted fibres subjected to external tensile loads by Jentzen [32]. Other creep tests were carried out by Sedlachek [64] with changes in moisture content on loaded specimens (cyclic humidity test), and also by removing the applied tensile load (creep recovery tests). The parameters in the creep model proposed here, are now identified using these experimental results, yielding $\gamma_0, m, \tau, H, \sigma_{y0}$ and the longitudinal elastic modulus E_l . The experimental tests are briefly described, and the parameter identification is discussed next.

4.3.1 Jentzen's creep tests on wetted single fibres

Among the early experiments performed on single fibres of wood, Jentzen [32] tested the creep response of longleaf pine fibres. After subjecting the freshly cut wood to the pulping procedure and chemical treatment, single fibres were separated. For drying the single fibre under load, a mass of 1gm was initially applied to keep the fibre straight while submerged in water and a reading of the elongation of the fibre was taken. The reference of the elongation reading was now set to this value. Thereafter, the desired mass (3gm and 5gm) was gradually applied in 1.5 minutes (Stage 1). The fibre elongation was measured at this point and after 3, 6, 9 and 15 minutes. Next, the water was removed from the tank stage (Stage 2) and finally the load was reduced gradually to the initial 1gm mass in 1.5 minutes (Stage 3) with readings taken.

The results of the tests are reproduced as the blue curves in Fig. 36.

Stage (1) corresponds to the increase of the strain up to point A and the subsequent strain evolution at constant load until point B in Fig. 36.

In Stage 2, the removal of water and subsequent drying of the fibre results in a steep increase of the elongation (right after point B in Fig. 36), followed by a mild decrease of the elongation until Point C (Fig. 36).

In Stage 3, the mass is finally reduced to 1gm which results in a decrease in the elongation further

followed by shrinkage.

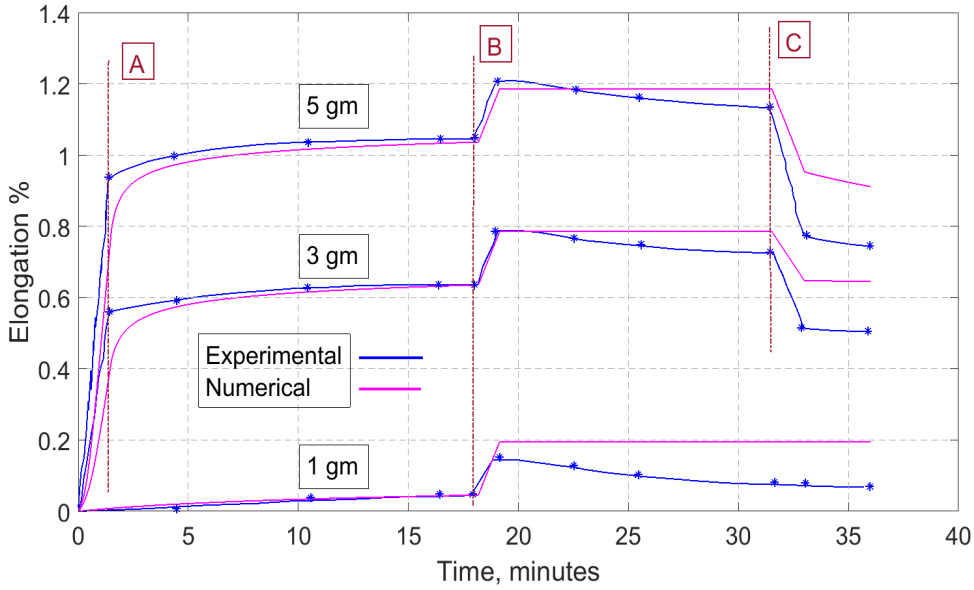


Figure 36: Results of Jentzen's experimental tests (overall strain vs time) reproduced from Jentzen [32], and comparison with simulated response.

Now, using the identical sequence of events for the moisture conditions and load application (1gm, 3gm and 5 gm), the numerical model is used to reproduce the strains in the fibre, from which the parameters are identified. The applied tensile stresses corresponding to the 1, 3 and 5gm loads are 24.7MPa, 98.9MPa and 148.5MPa respectively. The values of the parameters are $H=16\text{GPa}$, $\tau=100\text{s}$, $m=0.2$, $\gamma_0=10^{-5}$, $E_l=53.7\text{GPa}$, $E_t=E_l/6$, $G_{lt}=0.1E_l$, $\nu_{lt}=0.3$, $\nu_{tl}=0.05$ (the ratios of E_t being computed from Strömbro and Gudmundson [68] and ν_{lt} and ν_{tl} Schulgasser and Page [63]), $\sigma_{y0}=100\text{MPa}$ and $\beta_t=0.6$, $\beta_l=-0.03$ (coefficients of hygro-expansion by Niskanen [45]). The moisture contents are assumed to be $\chi = 0.11$ in the wet state and 0.06 in the dry state, $\chi_w=0.13$ and $\chi_{ref}=0.11$.

As shown in Jentzen's experimental result, just a few minutes after the water is removed, the fibre gets completely dried, and there is a sharp increase in the strain. This was further explained by Page and Tydemann [50] arguing that a reduction in moisture content leads to a decrease in the fibre diameter. This entails an elongation of the fibre, given the fact that the number of fibrils remains constant. In order to capture this behavior in the numerical model, a negative value of β_l was assumed, giving rise to a positive hygroscopic strain, ($\epsilon_l^h=\beta_l\Delta\chi$) when the moisture content is reduced as observed in the test. This occurrence of negative values of β_l has been further observed in the first moisture cycle in experiments on single paper fibres subjected to cyclic humidity [75].

Fig. 36 illustrates that the simulated results are in close agreement with the experimental results for the three different loading cases with the identified parameters for the viscoplastic behavior (γ_0 , σ_{y0} , m , H , β_l , β_t and τ) and the elastic properties of the fibre (E_l , E_t). Only the contraction in the stage 2 is not captured accurately by the adopted creep model. Therefore, these values can be

regarded as a calibrated set of parameters for the rate-dependent model for this test, as the model is rich enough to capture the experimental results. Later, this calibrated set of parameters is used for each fibre in a network model to compute their relaxation response.

4.3.2 Sedlachek's creep recovery and cyclic humidity tests on single fibres

One of the most popular sets of experimental results obtained on single fibres was reported by Sedlachek [64] on loblolly pine wood. Sedlachek performed two types of experiments, i.e. consisting of creep recovery tests and cyclic humidity tests.

In the creep recovery tests, the single fibres were loaded with a mass of 20 grams in 20 seconds at a constant moisture content of 50%. The mass was held for 20 minutes and then reduced suddenly to 1 gram. The mechanical responses measured under these conditions for 5 fibres are reproduced as the blue curves in Fig. 37. The total strain response of different single fibres of the same wood was measured in the experiments. The scatter due to the natural inhomogeneity in the material properties of wood. In order to reproduce these experimental results, the model parameters have been

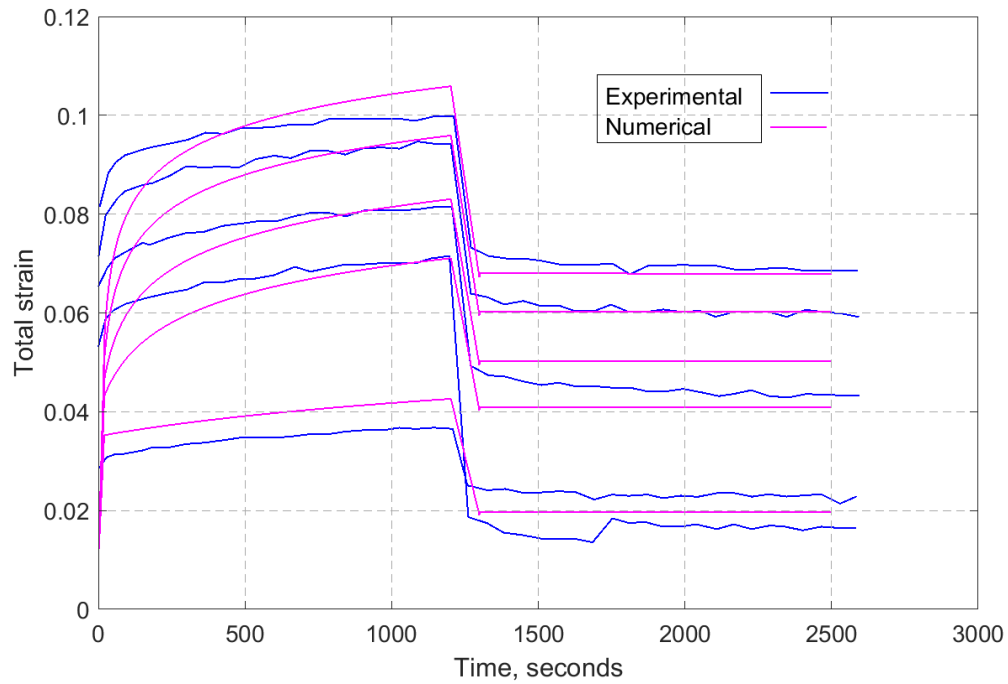


Figure 37: Results of Sedlachek's experimental creep recovery test (overall strain vs time) reproduced from Sedlachek [64], and comparison with simulated results.

identified as, $H=2.415\text{GPa}$, $\tau=100\text{s}$, $\gamma_0=10^{-5}$, $E_l=8\text{GPa}$, $E_t=E_l/6$, $G_{lt}=0.1E_l$, $\nu_{lt}=0.3$, $\nu_{tl}=0.05$, $\sigma_{y0}=155\text{MPa}$, $\beta_t=0.6$, $\beta_l=-0.12$, $m=0.1$. The moisture content is assumed to be, $\chi=0.028$ (adopted after calibration of the creep model to obtain the best match with experimental results), reference moisture content, $\chi_{ref}=0.12$ and $\chi_w=0.13$. The applied tensile stress, σ_0 equals 309MPa . From this reference set of parameters the numerical model captures the scatter in the experimental results by multiplying each of the parameters E_l , E_t , σ_{y0} and H by a factor f , where $f=0.97, 1.03, 1.12, 1.22$

and 1.60 for the 5 considered fibres, while keeping all other parameters constant.

Generally, the moisture content in manufactured paper sheets varies from 4% to 6% for a relative humidity of around 50% at 22.22°C (72°F). As the relative humidity increases, the moisture content in the paper exposed to this environment also increases. In this test, the moisture content of extracted hollocellulose fibre samples at 50%RH and at 90%RH was 8.7% and 14.3% respectively.

Due to the natural scatter in properties of the fibres, it is relevant to consider for each of the fibres slightly different material properties. The simplest way to do so is to modify all stress-like parameters with the same factor for a given fibre to capture the varying strain response of the different fibres taken from same wood. The results show that the model adequately captures the response of single fibres in the non-homogeneous wood under creep recovery conditions. Considering an individual variation of each of the parameters comprising f , the experimental response can be captured even more accurately. But, the main idea to vary them together is to highlight the strength of the model, which can capture the experimental response without having to vary each of them separately.

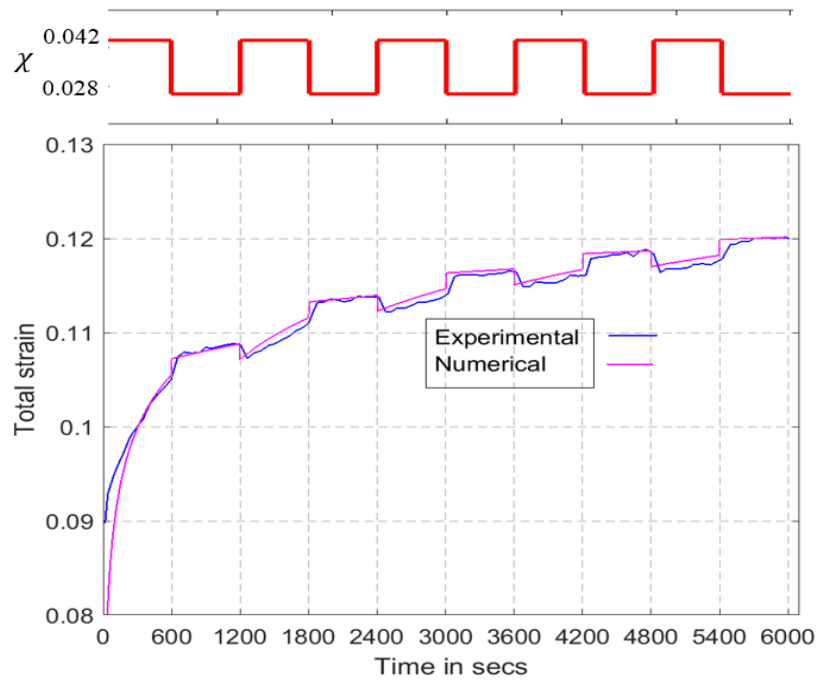
Finally, cyclic humidity tests were conducted by Sedlachek [64] on single fibres using humidity cycles (high (90%) to low (50%) and vice-versa) for 10 cycles under an applied tensile stress, σ_0 . The time duration of each of the cycles is 10 minutes. Fig. 38a reports both the experimental and the rate-dependent model responses. It is observed that the rate-dependent model reproduces the experimental results accurately for the cyclic humidity conditions using the previously identified fibre parameters matching the creep recovery tests.

With this set of identified parameters, the reverse cyclic humidity test within the moisture content range (0.028-0.042) (again adopted after calibration of the creep model to obtain the best match with experimental results) is simulated and compared with the experimental results. The model results are hence true predictions. Even though some quantitative differences between the numerical and experimental results can be observed in Fig. 38b a good prediction is obtained. Therefore, the model is considered to be validated. Modifying the hardening modulus H for the reverse cyclic test, would allow to capture this test with a higher accuracy as well. However, since out interest follows is in qualitative trends, we refrain from such fine-tuning of the parameters.

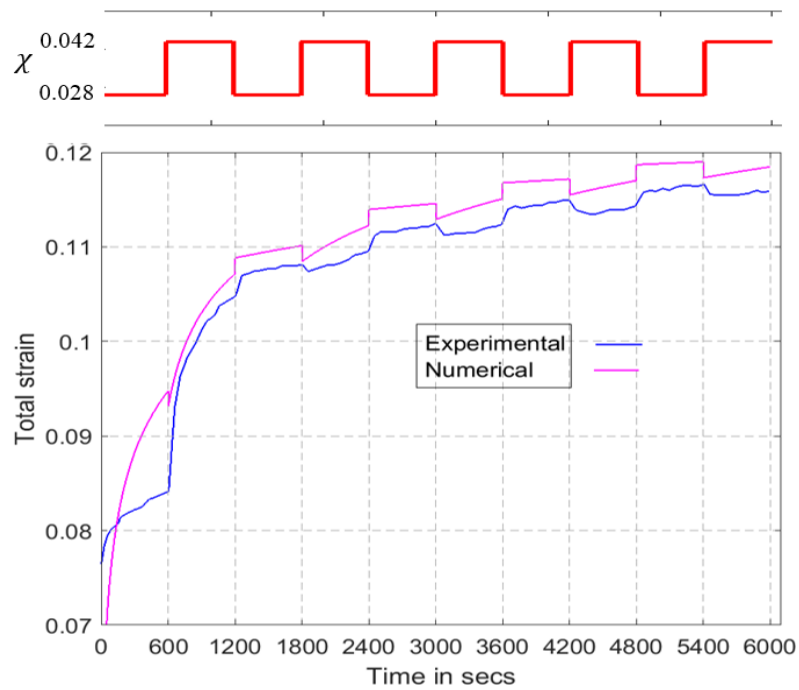
With this comparison with experimental results it can be ascertained that the numerical model is robust enough to capture the main experimental trends on single fibres. The identified model can be further used to analyze the time-dependent hygro-mechanical response of the fibre network in paper sheets.

4.4 RATE DEPENDENT FIBRE NETWORK RESPONSE

In this section, the response of a two-dimensional fibre network model under creep loading conditions is investigated. Modeling at the network-level is essential to understand the macroscopic response of paper at the sheet-scale by upscaling the fibre-scale behavior. Several aspects of the time-dependent behavior of paper at the sheet-level can be explained with the results obtained by such an upscaling procedure.



(a) Cyclic humidity test



(b) Reverse cyclic humidity test

Figure 38: Sedlachek’s single fibre cyclic humidity tests (overall strain vs time), reproduced from Sedlachek [64] and comparison with numerical model.

4.4.1 Random fibre network generation

In the model, the paper fibres are represented as long rectangles. They are randomly generated with a length l_f , width, $w_f=l_f/50$ with centroids in $(x,y) \in [0,l] \times [0,l]$ and orientation θ within a periodic unit cell Samantray, Peerlings, Massart, and Geers [62] as can be seen in Fig.39. Fibre parts which extend beyond the boundary of the unit cell are periodically copied into the cell at the opposite edge. The centroid coordinates x,y as well as the angles θ are generated according to a uniform probability distribution function, i.e. the networks are nominally uniform and isotropic. To characterize, the density of the network, we define the coverage c as as,

$$c = \frac{A_f}{A_c}, \quad (46)$$

where A_f is the area occupied by all fibres and A_{cell} is the total area of the unit cell. Typical values

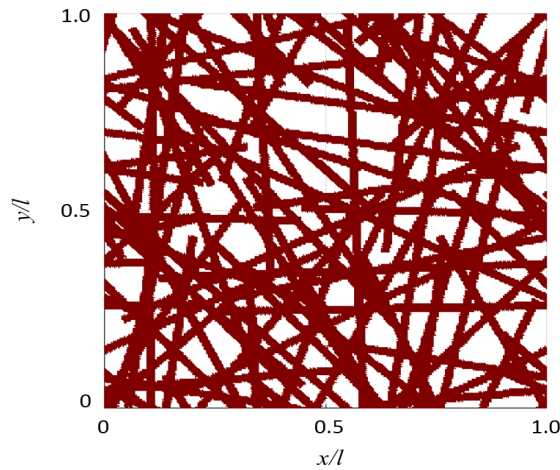


Figure 39: A periodic unit cell representing an infinite random network of coverage $c=1.0$.

of c for paper are on the order of 10. However, in the current analysis we have also considered lower coverages.

4.4.2 Hygro-mechanical model

As discussed in earlier Section, a hygroscopic strain is triggered at the fibre-level when the fibre is subjected to a change in moisture content. This fibre expansion ultimately causes deformation at the sheet-level in the network. The hygro-expansive strain at the macro-level of a network due to a uniform change in moisture content $\Delta\chi$ in the absence of external stress can be represented as

$${}^h\bar{\epsilon} = \bar{\beta}\Delta\chi \quad (47)$$

where $\bar{\beta}$ is the effective hygro-expansive coefficient tensor. This is a measure of the overall hygroscopic response of the network at the macro-level as a result of the hygro-expansion of the fibres in the network and their mutual interaction. Considering the occurrence of internal stresses within the

network, the total macroscopic strain is represented as an additive decomposition of elastic strain, creep strain and hygroscopic strain tensors

$$\bar{\epsilon} = {}^e\bar{\epsilon} + {}^c\bar{\epsilon} + {}^h\bar{\epsilon} \quad (48)$$

In the current study, the average stress response of the network is determined to analyze the stress relaxation of the networks. It is computed from the reaction forces at the control nodes of the periodic network.

4.4.3 Bond constitutive model

In the present contribution, the fibres are assumed to be perfectly bonded wherever they (partially) overlap. This implies, as described earlier (Samantray, Peerlings, Massart, and Geers [60]), that the total stiffness of the bond is the sum of the stiffnesses of the individual fibres constituting the bond. Likewise, the hygro-expansive behavior of all fibres involved in the bonds is taken into account and the fibres compete against each other via the mechanics.

The creep strain in each point of each fibre is computed by the return mapping algorithm discussed in Section 3. The creep model and the modeling methodology adopted for the single fibre discussed earlier is adopted for all the fibres in the network.

4.4.4 Moisture cycle simulation on networks

In our previous work [62], network models were subjected to a moisture cycle after the modeling of the irreversible strains associated with the papermaking process. It was shown that a fibre-level kinematic hardening plasticity model is able to reproduce the macroscopic irreversible strain release occurring during the first moisture cycle after production. Here, this effort is extended to capture the time-dependent response of the networks. For this purpose, five realizations each of coverages, $c=0.25, 0.5, 1.0, 1.5, 2.0, 3, 5.0$ and 10.0 with isotropic fibre orientations are considered. These networks are subjected to five different stages of moisture development and loading. The papermaking process is modeled by three stages, i.e. (1) Restrained drying (χ reduces from 0.11 to 0.055); (2) Stress release at a constant moisture level; (3) free drying (χ reduces to 0.038). Thereafter, the networks are subjected to a moisture cycle consisting of free wetting (χ increases to 0.11) and free drying (χ reduces again to 0.038).

The values of $\sigma_{y0}, \gamma_0, \chi_w, E_l, E_t, G, \nu_{lt}, \nu_{tl}, \beta_t, H, \chi_{ref}, m$ and τ for the individual fibres are the same as obtained by the calibration on Jentzen's single fibre experimental results. In view of the identification performed in the earlier section on single fibre tests, we have adopted a negative value of $\beta_l = -\frac{\beta_t}{20}$. The numerical simulations are performed with a uniform mesh of size, $h=l/200$. The average time taken for a single simulations of network for each coverage $c=0.25-10.0$ is in the range of 25-125 hrs.

Fig. 40 depicts the irreversible strain release during the first moisture cycle after production as a function of the network coverage. Fig. 40 reveals that the irreversible strains, normalized with $|\beta_l|\Delta\chi$, where $\Delta\chi=0.072$, increases initially until approximately $c=3.0$ and thereafter decreases again. The local creep strains develop mostly in the free standing parts of the fibres within the networks in the constrained drying phase of the manufacturing stage. They later get released in the moisture cycle comparable to the rate-independent plastic strains in our earlier work [62]. As the

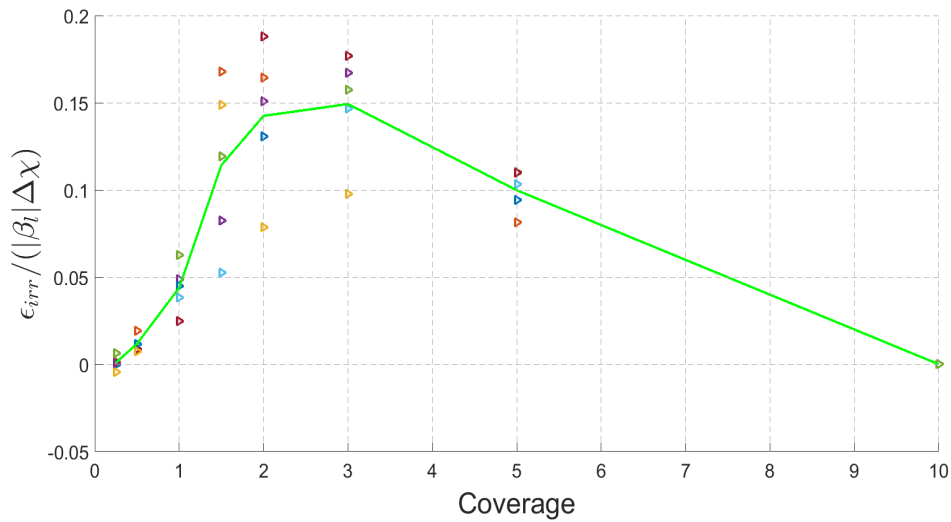


Figure 40: Macroscopic irreversible strain release during first wetting-drying cycle, normalized with $|\beta_l|\Delta\chi$, as a function of the network coverage.

coverage increases, the area fraction of the free standing parts of fibres initially increases but later decreases [62] resulting in the development of lower creep strains at higher coverage. Therefore, a trend emerges in which an increase of the irreversible strain release is observed until a certain coverage, followed by a reduction at higher coverage. This explains the limit appearing at $c=10.0$ where there is no irreversible strain. This is in contrast with the experimental findings of [43], showing a considerable amount of irreversible strains at the sheet-scale. Note that a quantitative comparison cannot be made with the earlier study of irreversible strains (in networks subjected to moisture cycles) modeled with a rate independent kinematic hardening model, in chapter 3, because the material parameters and the model parameters are not identical. Also, the sign of β_l values considered in both studies is different. Now, with the adoption of a negative value of β_l in the rate-dependent model, an effect does exist in the magnitude of the irreversible strains quantitatively in comparison with the rate-independent model but qualitatively, the trend remains unaffected. The model fails to capture irreversible strains at coverages higher than $c=5.0$. Certain assumptions in the model including the generation of the creep strains under only tension and the fibres being fully bonded in the regions of overlap may be the cause of this lack of irreversible strain at the sheet scale.

4.4.5 Influence of moisture content and coverage on the network relaxation

In this section, the relaxation response of a network at different moisture contents is analyzed. For this purpose, a network with coverage, $c = 1.0$ as shown in Fig. 41 is considered. A global strain of $1/50$ is applied to the network in the horizontal level direction and kept constant over the entire duration of the simulation. Three different constant moisture contents ($\chi = 0.06, \chi = 0.09, \chi = 0.12$) are considered. The elastic and creep properties of the fibres are the same as in the previous section. Also, to understand the relaxation response of the networks, the same problem set up is applied to a single fibre and its results are compared with the network response. The paper networks are conditioned to the moisture contents ($\chi = 0.06, \chi = 0.09, \chi = 0.12$) and thereafter the global strain

is applied as mentioned above. The average time taken for the simulations of networks for all moisture contents is 14 hrs.

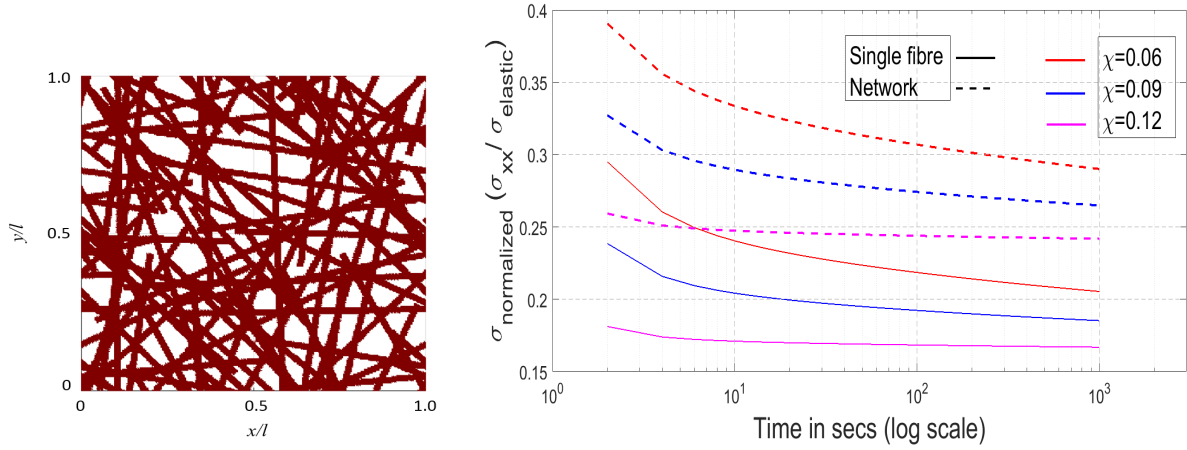


Figure 41: Relaxation of a network of coverage, $c=1.0$ and single fibre at different moisture content.

The relaxation response of the network over the considered period of time can be a consequence of both the fibre creeping behavior and the network complexity. In order to distinguish both effects, the average σ_{xx} stress response of the networks normalized with respect to the elastic response is computed for the relaxation tests. Fig. 41b shows that as the moisture content decreases, the stress level in the network increases, i.e less stress is released from the network. This can be explained by the fact that a lower moisture content leads to a higher yield stress and therefore to less creep strains, thereby producing more elastic strain and stress as the total mechanical strain is constant in a relaxation test.

Interestingly, the relaxation of the single fibres occurs faster as compared to the network. This is in agreement with the experimental observation made by [16] that the creep strain rates in single fibres under a constant humidity is very high as compared to paper handsheets. In a single fibre, there is only a free standing fibre which is less constrained leading to development of high creep strains. However, in a network with same coverage $c=1$ as of a single fibre, due to occurrence of bonds, the area fraction of free standing fibres responsible for creep strain is relatively lower. Therefore, the model is strong enough to capture this experimentally observed behavior qualitatively at the sheet-level too.

There is similarity between the stress relaxation observed in the current simulations and the stress relaxation response in cross-direction in reference [33], with the wetter network relaxing faster as compared to dry networks. However, the curves have different shapes. A cause could be that the networks considered for the simulations are isotropic as compared to the kraft paper having a preferential fibre orientation direction, different material properties comparatively and the non-linear rate dependent model in consideration.

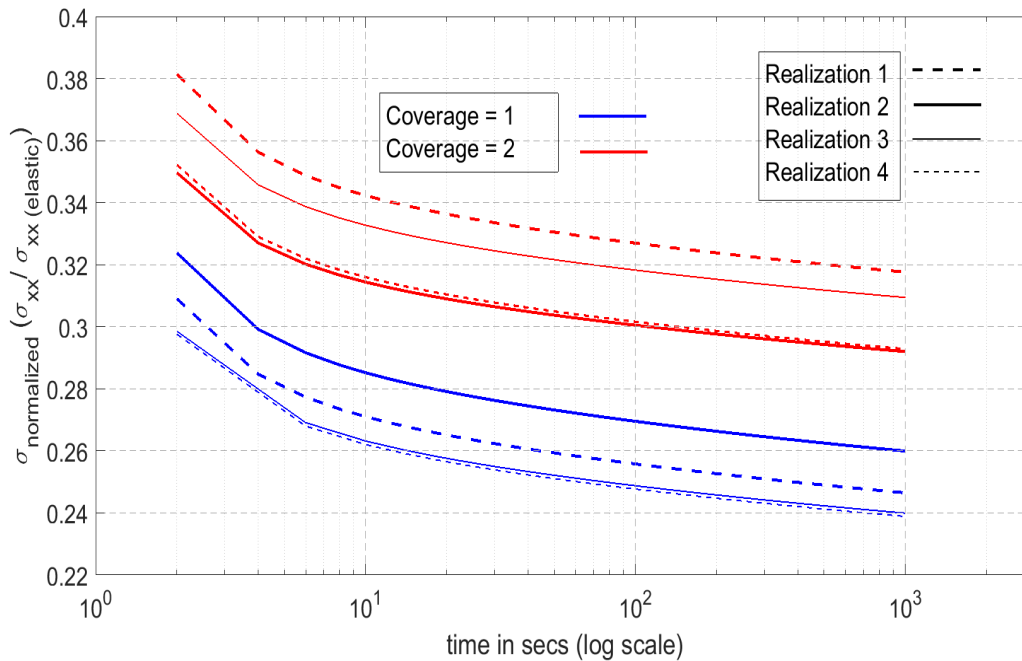


Figure 42: The stress relaxation response of a network with creep (normalized with the elastic response) at different coverages (4 different realizations of each).

In order to assess the dependency on the network coverage, relaxation tests were simulated for four realizations of each coverage, $c=1.0$ and $c=2.0$. The simulation times for networks of coverage $c=1.0$ and $c=2.0$ are on order of 18 and 32 hrs respectively. Identical global strains were applied on the network conditioned at moisture content $\Delta\chi=0.09$. Fig. 42 reveals that the average stress response (normalized with the stress obtained with only elastic response) at a network coverage $c=2.0$ is higher compared to its value at a network coverage, $c=1.0$. Also, it is observed that the relaxation is faster for a coverage, $c=1.0$ in comparison with $c=2.0$. This is due to the higher area fraction of free-standing fibres in networks with $c=1.0$ as compared with $c=2.0$. Higher creep strains are generated in the free standing regions of the networks as a function of time. This results in lower values of elastic strains in the fibres with the applied mechanical strain being constant. This leads to a relative reduction in stress. It can be observed in these stress relaxation plots that there is less change in stress for $t > 10s$, with most of the relaxation already happening before. A cause could be that the applied strain is large, that the yield stress considered, that is moisture dependent, has low values and that the rate sensitivity parameter is high.

4.5 CONCLUSIONS

In this chapter, the time dependent hygro-mechanical response of a single fibre and of a fibre network was studied under an external loading and under changes in moisture content. Paper fibres, during papermaking process and printing, are subjected to different rates of drying and wetting, which cause time-dependent deformations. Additionally, when they are subjected to varying levels of moisture in environmental conditions over long periods of time, macro-level curls or waviness may occur.

In order to understand such behavior, a rate dependent creep model is adopted at the scale of fibres. Assuming that the fibre segment activation mechanism governs this behavior (Bosco, Peerlings, and Geers [7]), the creep strains are incorporated in the longitudinal fibre response only. A backstress plasticity creep model was formulated in order to capture the rate dependent deformation, even in the absence of an externally applied stress. The model was used to reproduce the hygro-mechanical response of single fibres, which was compared with the results of experimental tests Jentzen [32] and Sedlachek [64]. The results obtained by the rate dependent model demonstrate an adequate match with the experimental results, which allowed to identify the material parameters (hygroelastic and creep) for the model. It has been shown that the rate-dependent model is robust enough to capture the time dependent response of single fibres. Furthermore, a validation was performed to capture the experimental test on reverse cyclic humidity test with the identified parameters obtained for the reference cyclic humidity test.

The numerical simulations exploiting this rate dependent model were next extended to the relaxation of networks subjected to externally applied strains at different moisture contents. The results were also compared with single fibres. It is observed that single fibres relax faster than the networks, which stems from the fact that the single fibres consist completely of free standing regions thereby generating more creep strains and resulting in a faster relaxation. This observation was also made by experiments conducted by Coffin and Boese [16] and the adopted rate-dependent model was able to capture this creep behavior successfully. Therefore, it can be concluded that the adopted creep model is very good in capturing this experimentally observed behavior qualitatively at the sheet-scale of the network in addition to the good match obtained with the experimental results (as illustrated earlier) of single fibres with the same set of the identified parameters for both of them.

Also, relaxation tests were performed for four network realizations with coverages $c=1.0$ and $c=2.0$. The networks with coverage $c=1.0$ relaxed faster than the networks of coverage $c=2.0$ due to presence of more free-standing parts. Also, relatively high stress levels were observed in networks with coverage $c=2.0$ as expected. With the incorporation of the time-dependent response of individual fibres, the irreversible strain release at the first moisture cycle after manufacturing was shown to gradually increase with the coverage, until a coverage of about $c=3.0$, followed by a steady decline for coverages higher than 3.0. The latter was due to the increase of the area of bonded fibres relative to the free-standing fibre parts.

There is currently a discussion in the literature on the material parameters of fibres and the corresponding experimental hygro-mechanical response. There is a lack of comprehensive experimental characterization of the material parameters for the fibres. Therefore, we have adopted only certain values from the experiments and not the rest of them. We are interested in the trends of the hygro-mechanical response of the network rather than in quantitative predictions. For this, we consider the current parameter set to be adequate.

Earlier in the thesis, a positive value was assumed for β_l but with the progress of studies on paper fibres in this thesis, a negative value of beta was found to be necessary to match the experimental responses. However, the results obtained in the previous chapters are still relevant because even with a negative value of β_l the trends do not change qualitatively.

One of the strong assumptions in the present contribution is the assumption of perfect bonding between the fibres in the regions of overlap in the network. This can be mitigated by relaxing the kinematic constraints in the bonds, which forms the basis for future work. An investigation can be carried out to understand the exact role of such kinematic constraints in the generation of the creep strains in bonds and their impact on the macroscale behavior of the network.

EFFECT OF KINEMATIC CONSTRAINTS IN THE BONDED REGIONS OF PAPER FIBRE NETWORKS AT THE SHEET-SCALE.

In fibrous paper materials, an exposure to a variation in moisture content causes changes in the geometrical and mechanical properties. Such changes are strongly affected by the inter-fibre bonds, i.e. the places where the fibres overlap, which are responsible for the transfer of the hygro-mechanical response from one fibre to its neighbors in the network, resulting in macro-scale deformations. Most models developed in literature simply assume perfect bonding between fibres. Using a homogenization approach, a random network of fibres is generated with different coverages and modeled using finite elements. In order to understand the role of bonding between fibres in the hygro-expansive behavior of network, a bond model is developed. Fibres are modeled using regular bulk finite elements. Bonds are represented by interfacial elements of finite stiffness introduced between each couple of fibres bonded in the network. These embedded interfacial elements form a connection between two respective fibres, allowing relative displacements between them. The hygro-elastic response of networks obtained with this bond model is investigated by varying the bond stiffness and the network coverage under the application of mechanical loading and changes in moisture. Further, the bond model is used to analyze the influence of inter-fibre bonds on the anisotropic response of the paper fibre network.

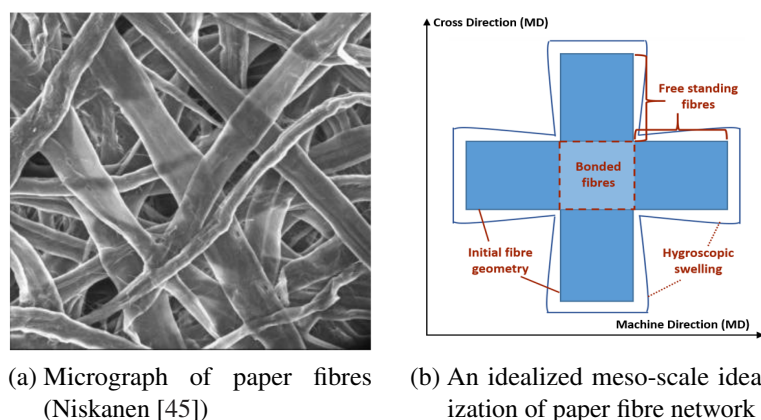
Keywords: Fibrous network, hygro-expansion, irreversible strains, coverage, interfacial elements

⁴ This chapter is based on: P. Samantray, R.H.J. Peerlings, T.J. Massart, M.G.D. Geers, 2019. *Effect of kinematic constraints in the bonded regions of paper network at the sheet-scale*. In preparation.

5.1 INTRODUCTION

Fibrous materials like paper consist of natural fibres that are bonded in overlapping regions, as observed in the microstructure in Fig. 43a. During manufacturing of paper, the fibres are preferentially oriented in the machine direction, which entails anisotropy in the mechanical behavior of the paper network [37]. The principal directions of the paper material are denoted as the machine direction (MD) and cross direction (CD) as used in the two dimensional meso-scale idealization of the paper network in Fig. 43b by [8]. In paper, the fibres are interconnected to each other in overlapping regions, i.e. the bonds as shown in Fig 43b. The coefficient of hygro-expansion of fibres in the lateral direction was found to be nearly 20 times the corresponding value in the longitudinal direction [45] of a paper fibre.

This can be observed experimentally from the swelling of the free standing parts of fibres in the lateral and longitudinal direction as exploited in idealized representations, see Fig. 43b. The fibres in these inter-fibre bonds are connected together by hydrogen bonding and van der Waal's forces [26]. The anisotropic behavior originating at the scale of individual fibre gets transferred from one



(a) Micrograph of paper fibres (Niskanen [45])

(b) An idealized meso-scale idealization of paper fibre network

Figure 43: A two fibre meso-scale idealized network subjected to hygroscopic strain.

region to another in the network through these inter-fibre bonds.

It is emphasized that the degree of bonding between fibres and their quantity in the network have a crucial influence on the hygro-mechanical response of the network. Earlier studies demonstrated that the effective stiffness of the network is mainly dependent on the density of the network, the fibre orientations, fibre properties and the inter-fibre connectivity resulting from the bonds [6, 17, 27, 34, 41]). Also, when subjected to moisture changes, it was noticed that the effective hygro-expansivity of the paper network is influenced by the bonded regions of the network as discussed in Chapter 2 and in references [7, 21, 37, 45, 59, 62, 71, 72]. These hygro-mechanical properties of the paper which are dependent on the inter-fibre connectivity hold significance in understanding the dimensional stability of paper products like packaging materials, printed papers, corrugated boxes, tissue papers or paper boards. Instabilities appear as curls or waviness at the paper sheet-scale. Therefore, the main objective of the present study is to examine the effects of the inter-fibre bonds on the behavior at the sheet-scale level and on the anisotropy of paper, subjected to tensile loading and a uniform

moisture gradient.

In some earlier works, fibrous networks were modeled in 2D and 3D configurations as trusses or beam elements with the bonds between the fibres assumed to be rigid [9, 12, 38, 41, 67]. A limitation of such a bond description is its inability to describe the influence of inter-fibre connectivity on the sheet-scale deformations, as well as the extent to which certain fibre network properties (e.g. bond area, bonding strength) affect the macro-scale response that can be modified in the manufacturing process. On the other hand, some other works describing the bonds as not rigid e.g. model the bonds as springs ([27];). The fibres were partially bonded in regions of overlap ([35]). They were modeled based on a non-linear contact law with bond failure in ([36]), and as two node line elements in ([39]).

In a relevant recent paper [44], beam elements were used to model the network in 3D and the change in hygro-expansion as well as effective stiffness of the network were studied by a variation of density or deactivating the bonds. This approach was found to model the hygro-expansion of networks of large sizes and capture the experimental results also successfully. It was found that the usage of a 2D bond model in the simulation of the hygro-expansion, results in an underestimation of the out of plane deformations and overestimation of the effect of the transverse shrinkage on the overall inplane hygroexpansivity. Most of the literature that incorporates the deformation in bonds did not address the effect of bond stiffness on the anisotropic response of the network. The analysis of the modeling of hygro-mechanical behavior in 3D with non-perfect bonds entails costly computational efforts, preventing parametric variations of the bond effect. Therefore, there is a need to understand the hygro-mechanical response of the networks due to varying bonding properties (stiffness) connecting the fibres, along with its influence on the anisotropy of the network using a 2D modeling framework with cheaper computational efforts. This serves as a motivation for the current chapter. Here, these issues are addressed by describing the inter-fibre connectivity through an appropriate bond model.

Initially, the fibrous network is represented with a 2D periodic unit cell [52] of randomly generated rectangular strips [60] that represent ribbon-shaped paper fibres. Each fibre in the unit cell network is discretized with standard triangular finite elements. At the regions of inter-fibre bonds, an additional triangular interfacial element with a suitable stiffness, connecting two successive fibres (in thickness direction) is inserted in the model. These finite stiffness elements render the bonds to be no longer rigid and the connected fibre can therefore have relative displacements. With this model, the macroscopic behavior of the paper network with different values for the bond stiffness, can be computed when subjected to an external mechanical load and a uniform moisture gradient. This provides clear insights in the sheet-level response using a 2D network model with moderate computational efforts only. Furthermore, the influence of connectivity between fibres at the bonds on the anisotropy of the paper network at the sheet-scale will also be assessed. The main idea of this chapter is the development and application of the bond model to study the effect of the inter-fibre bonding quality on the hygro-elastic response of the network. Therefore, the irreversible and rate effects are not included in this study.

In Section 2, the hygro-mechanical model for the fibre and the network is described. The generation of random networks, the bond model and the numerical discretization adopted are explained in Section 2 together with the considered stacking of fibres in the network. The results illustrating the influence of the bond stiffness at the sheet-level response of the network along with its anisotropy

are detailed in Section 3. Finally the conclusions are drawn in the Section 4.

Throughout this contribution, the following notations are used for operations on Cartesian tensors and tensor products. Scalars, vectors and tensors are denoted by a , \vec{a} and A respectively. For tensor and vector operations, the following equivalent notations are used with Einstein's summation convention on indices: $A:B=A_{ij}B_{ji}$ with ($i=x,y,z$ for the global reference system and $i=1,t,z$ for the fibre local reference system). The Voigt notation used to represent tensors and tensor operations in a matrix format is depicted as follows: \underline{a} and \underline{A} denote a column matrix and a matrix of scalars respectively. The matrix multiplication is denoted as $(\underline{A} \underline{a} = A_{ij}a_j)$.

5.2 HYGRO-MECHANICAL CONSTITUTIVE MODEL AND NUMERICAL DISCRETIZATION

5.2.1 Fibre model

Lets consider a 2D configuration with plane stress in the z -direction (with z normal to the paper sheet). The hygroscopic strain tensor ${}^h\epsilon^f$ and the stress tensor in a fibre upon exposure to a unit change in the moisture content $\Delta\chi$ are given by the constitutive relation

$${}^h\epsilon^f = \beta^f \Delta\chi \quad (49)$$

$$\sigma^f = {}^4D^f : (\epsilon^f - \beta^f \Delta\chi) \quad (50)$$

where σ^f , ${}^4D^f$ and β^f are the stress tensor, the elastic stiffness tensor and the hygroscopic expansion tensor of the fibre respectively. In the Voigt matrix notation, the stiffness and hygro-expansion coefficients are represented as

$$\underline{D}^f = \begin{pmatrix} \frac{E_l}{(1-\nu_{lt}\nu_{tl})} & \frac{E_l\nu_{tl}}{(1-\nu_{lt}\nu_{tl})} & 0 \\ \frac{E_t\nu_{lt}}{(1-\nu_{lt}\nu_{tl})} & \frac{E_t}{(1-\nu_{lt}\nu_{tl})} & 0 \\ 0 & 0 & G_{lt} \end{pmatrix}, \underline{\beta}^f = \begin{pmatrix} \beta_l \\ \beta_t \\ 0 \end{pmatrix} \quad (51)$$

where E_l and E_t are the elastic moduli in the longitudinal and transverse direction with respect to the fibre material axes. β_l and β_t represent the coefficients of hygroscopic expansion in the longitudinal and transverse directions associated to the fibre axis. ν_{lt} and ν_{tl} are the in-plane Poisson's ratios and G_{lt} is the in-plane shear modulus. The constitutive relationships Eq. (49) - Eq. (51) are expressed in the local reference system (1,t,z) attached to the fibre as described in Fig. 44 for a fibre m oriented at an angle $\theta^{(m)}$. This relationship can be transformed to the global reference system (x,y,z) yielding the global elastic constitutive tensor and hygroscopic coefficient tensor (Roylance [55]).

5.2.2 Bond model

In the network, regions in which the fibres overlap are called inter-fibre bonds, as shown in Fig. 46a. In the 2D models discussed so far, the bonds are assumed to be fully rigid with no relative displacements between the fibres in the bond. The interface model is developed to represent the exact behaviour of the fibres in the bonded region in 3D as shown in Fig. 45 with the shear forces acting between fibres allowing relative displacements between them. The corresponding representation of

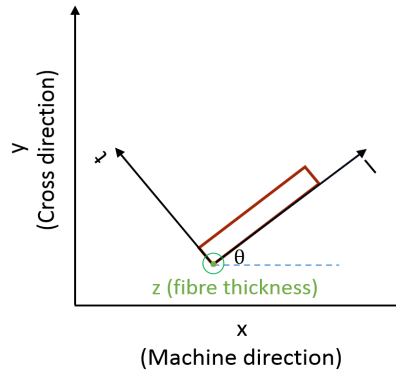


Figure 44: The local and global coordinate axes.

these fibres in 2D plane stress setting by the bond model is depicted with the mid-planes of fibres in the figure.

The nature of the bond between fibres can be represented with three interconnect models as depicted in the cross-section A-A in Fig. 46b. In the fully uncoupled case, the transverse and longitudinal regions of the fibres involved in the bond are completely detached from each other, which results in free swelling across the mid-planes. In the fully coupled case, both fibres are connected by a rigid bond between the fibres. This entails compatible displacements in the bond plane, as often used in the literature [8].

In the partially coupled case, the fibres are constrained to some extent but may exhibit relative displacements. This closely resembles the case where the springs interconnect the fibres to enforce a kinematic coupling. In this case, the fibres are partially tied to each other and do not exhibit free swelling.

This is implemented by adding an elastic interfacial element of thickness t between the midplanes of fibres. Interface elements thus connect two fibres in the bond, allowing them to deform with respect to each other, and thereby relaxing the rigid constraints often used in the literature as mentioned in the introduction. The extent to which the stacked fibres may have relative displacements depends on the stiffness of the interfacial element adopted. Let us consider a bond which is governed by the following constitutive law

$$\vec{\tau} = \frac{k_h}{t} \Delta \vec{g}$$

$$\Delta \vec{g} = \begin{bmatrix} \Delta u & \Delta v \end{bmatrix} \begin{bmatrix} e_x \\ e_y \end{bmatrix}$$

where $\vec{\tau}$ is the shear stress vector acting in the plane of the interface, k_h is the interfacial stiffness modulus of the bond between both fibres, that has same units as the shear modulus G of a fibre, $\Delta \vec{g}$ is the differential displacement vector, Δu and Δv are the differential displacements in x and y direction between the fibres in the inter-fibre bonds and t is the thickness of a fibre.

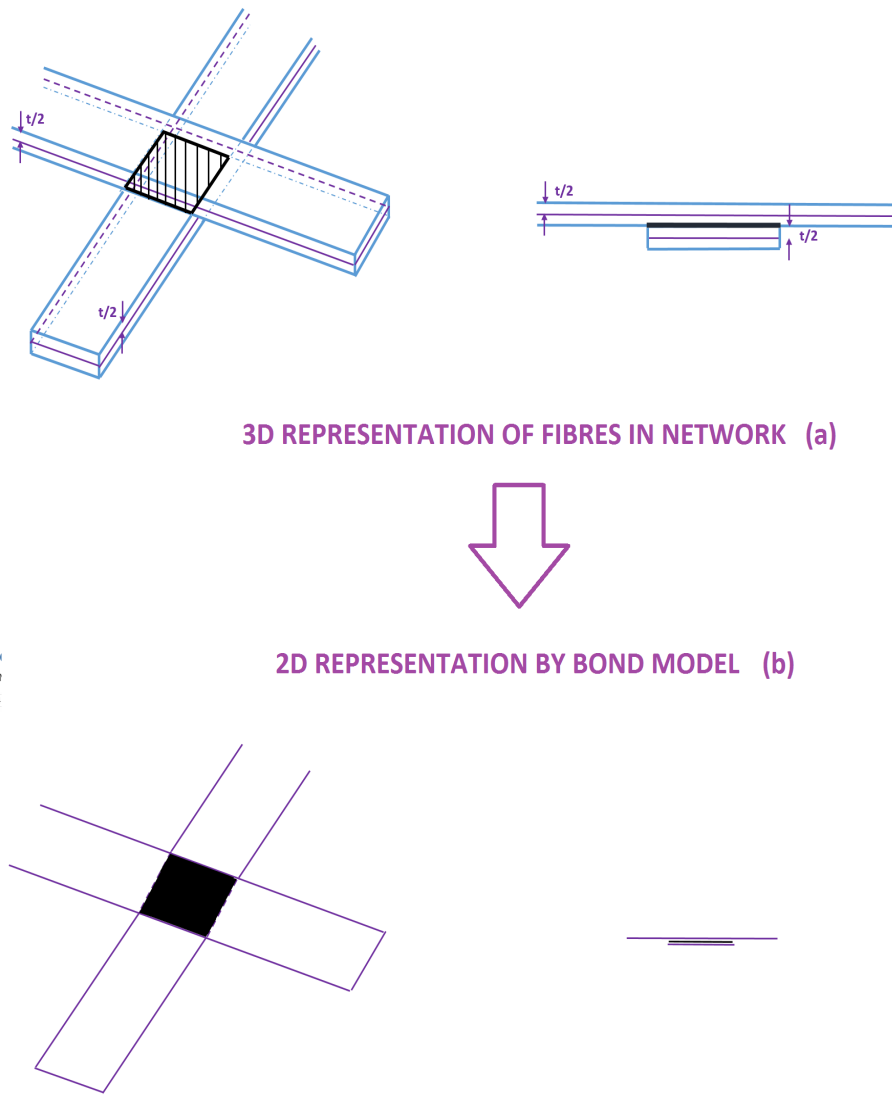
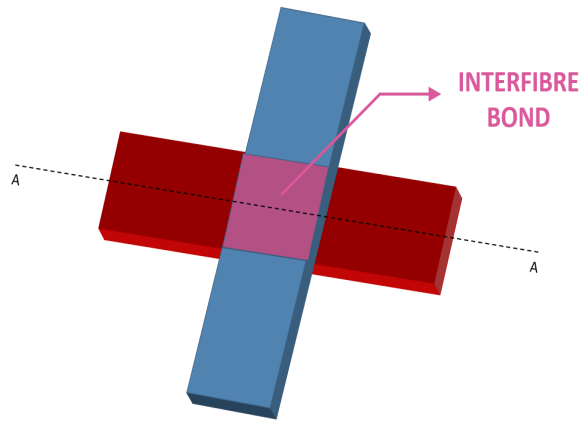
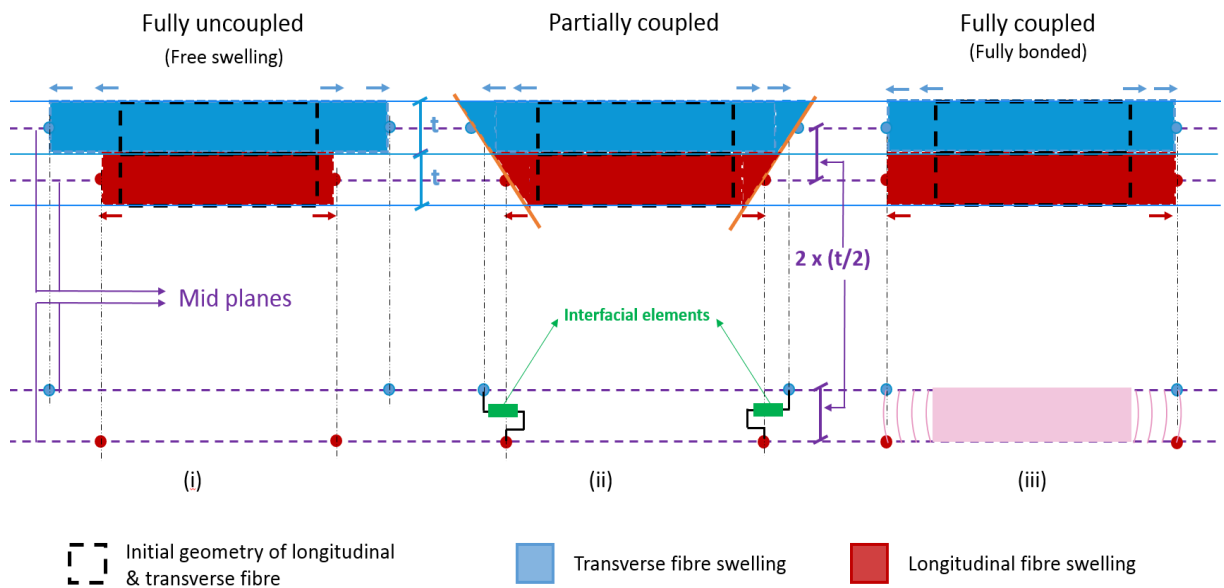


Figure 45: Representation of the fibres in 3D by the bond model in 2D.



(a) 3D representation of two fibres



(b) Cross-section A-A

Figure 46: The mechanism of the bond model interconnecting overlapping fibres.

When $k_h=G$, the bond represents the physical shear between the mid-planes of both fibres, taking their thickness into account for this 2D setting. Hence, it is a potential value of k_h , representing a rigid bond in a 3D setting. However, the hygro-mechanical response of the networks at different values of interfacial stiffness, k_h is illustrated later in the results section to render a complete picture in this regard.

5.2.3 Network Model

In a 2D representation, the paper fibres are assumed to be ribbon-shaped elements. Hence, networks are represented by a set of randomly generated rectangular shaped fibres. The fibre length is denoted l_f , the fibre width $w_f=l_f/50$ and the thickness is assumed to be $t=l_f/150$. The positions of the centroids of the rectangular fibres are randomly generated within the domain $[x,y] \in [0,l]$ of the periodic unit cell of length $l=l_f$ as shown in Fig. 47a.

During the generation of fibres, they are numbered and stacked in the corresponding sequence. The orientation of the fibres in the network can be random, which makes the corresponding networks isotropic. Reflecting the amount of fibres added to a given RVE, the coverage c is defined as the ratio of the area of all fibres with that of the unit cell, a number that will be used later in this study. The coverage is a measure of the density of fibres in the network.

Stacking of fibres

The randomly generated fibres in the network are assigned a number. The fibres are deposited

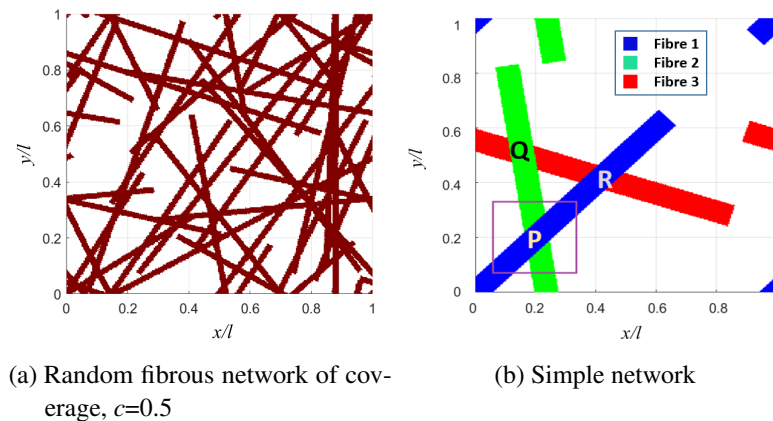


Figure 47: Periodic unit cell of a random fibrous network and a simple sparse network.

subsequently with the highest numbered fibre lying below the lower ones as shown in Fig. 47b.

Layers for each fibres

Each of the fibres in the network is assumed to occupy a particular layer pertaining to the fibre number as shown in Fig. 49. In order to compute the hygro-mechanical response of such RVE, we have adopted a finite element based method. With this method and using a structured triangular mesh, the finite elements and nodes are created to represent only the fibres in each of the layers. They are numbered in a sequential manner with each fibre i.e. fibre after fibre or equivalently layer

by layer in the mesh. Therefore, a stack of elements are created representing the stack of overlapping fibres.

Overlapping of fibres

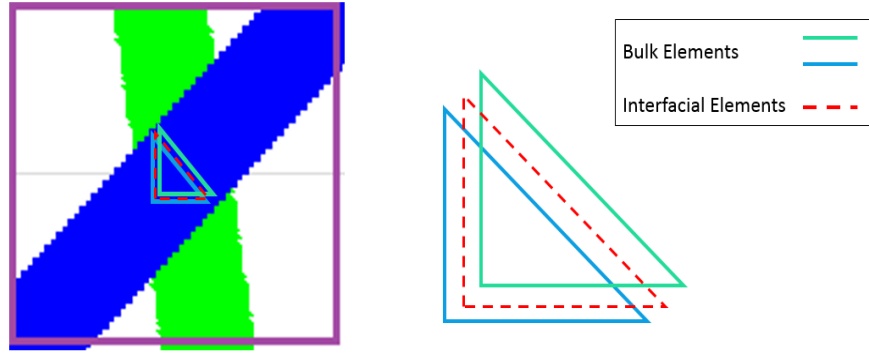


Figure 48: Interfacial elements at the bonds

The fibres that overlap a fibre immediately below them are assumed to be bonded to it, and an interfacial element is introduced accordingly see Fig. 48. Such interfacial elements at the inter-fibre bonds between fibres are thus defined between stacked fibres at a point of the RVE, linking fibres two by two in ascending sequence of their layer number. For example in the Fig. 47b, it can be seen that fibre 1 and fibre 2 have a bond at region P. Also, fibre 1 and fibre 3 (which is in a layer not immediately below) are also connected through an inter-fibre bond at R in the model. In similar manner, the pair of fibres that are touching each other or on top of each other in the bonded regions are linked by an interfacial element. Only the pairs closest to each other in the thickness direction are connected by an interface.

Implementation of periodicity

Each of the layers is periodic and modeled accordingly. The 1st layer contains the control nodes 1, 2 and 3 see Fig. 49. Nodes are assigned at the boundary of the layers, whenever a fibre crosses the boundary.

The periodic implementation for layer 2 and layer 3 is given by

$$\text{Periodicity for Layer 2: } \vec{g}_{23} - \vec{g}_{21} = \vec{g}_3 - \vec{g}_1 \quad (52)$$

$$\vec{g}_{24} - \vec{g}_{22} = \vec{g}_3 - \vec{g}_1 \quad (53)$$

$$\text{Periodicity for Layer 3: } \vec{g}_{33} - \vec{g}_{31} = \vec{g}_2 - \vec{g}_1 \quad (54)$$

$$\vec{g}_{34} - \vec{g}_{32} = \vec{g}_2 - \vec{g}_1 \quad (55)$$

5.2.4 *Macroscopic Response*

The overall hygro-mechanical response of a network can be assessed by its effective macroscopic properties. These depend on the material and geometrical properties of the individual fibres interact-

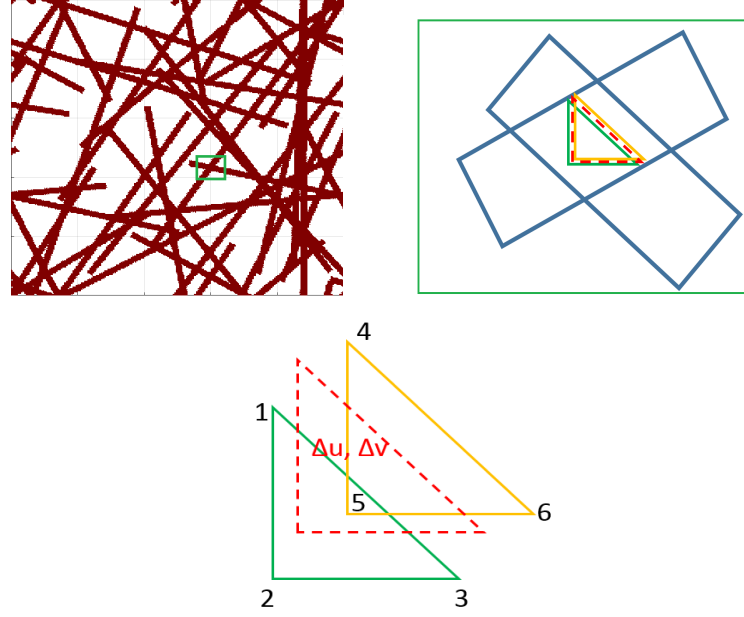


Figure 50: (a) A randomly generated fibrous network of paper(top left) (b) Bond region (top right) (c) Interfacial element(bottom center)

In Voigt matrix notation, the total energy of the periodic unit cell reads

$$E = \frac{1}{2} \int_V \sum_{i=1}^n (\underline{\epsilon}_i^f - {}^h \underline{\epsilon}_i^f)^T \underline{\mathbf{D}}_i^f (\underline{\epsilon}_i^f - {}^h \underline{\epsilon}_i^f) dV + \frac{1}{2} \int_A \sum_{j=1}^s (\Delta \underline{g}) \frac{k_h}{t} (\Delta \underline{g}) dA \quad (60)$$

In Fig. 50, part of the bonded region of two fibres in the network is considered, in which there are two triangular finite elements. These are connected through an interfacial element at their nodes. The components of the relative displacement $\Delta \underline{g}$ for an interfacial element can be represented by

$$\Delta u = \zeta(u_1 - u_4) + \eta(u_2 - u_5) + (1 - \zeta - \eta)(u_3 - u_6)$$

$$\Delta v = \zeta(v_1 - v_4) + \eta(v_2 - v_5) + (1 - \zeta - \eta)(v_3 - v_6)$$

where ζ and η are the shape functions associated with the interfacial element. This can be further represented in matrix form as

$$\Delta \underline{g} = \begin{bmatrix} \Delta u \\ \Delta v \end{bmatrix} = \underline{\mathbf{B}}^c \underline{w}$$

$$\underline{\mathbf{B}}^c = \begin{bmatrix} \zeta & 0 & \eta & 0 & (1 - \zeta - \eta) & 0 & -\zeta & 0 & -\eta & 0 & -(1 - \zeta - \eta) & 0 \\ 0 & \zeta & 0 & \eta & 0 & (1 - \zeta - \eta) & 0 & -\zeta & 0 & -\eta & 0 & -(1 - \zeta - \eta) \end{bmatrix}$$

The nodal displacements at the nodes of both the connected bulk finite elements is represented by a column matrix $\underline{w} = [u_1 \ v_1 \ u_2 \ v_2 \ u_3 \ v_3 \ u_4 \ v_4 \ u_5 \ v_5 \ u_6 \ v_6]^T$.

Upon substituting $\Delta \underline{g}$ in the 2nd term of Eq. 60, the expression for the energy of all interfacial elements over all the bonds is obtained, as is further discussed below. A standard finite element method is used in the bond model to compute the hygro-mechanical response of the network. The

stiffness computation for each of the interfacial element is carried out by a six point Gauss-legendre quadrature rule for triangular finite elements.

Discretizing the entire network domain with m finite elements and s interfacial elements, Eq. 60 reduces to

$$\frac{1}{2} \sum_{e=1}^m \sum_{i=1}^n \int \mathbf{B}_e^T \mathbf{D}_i^f \mathbf{B}_e t dA \underline{u} + \frac{1}{2} \sum_{j=1}^s \int (\mathbf{B}_j^c)^T \frac{k_h}{t} \mathbf{B}_j^c dA \underline{u} = \frac{1}{2} \sum_{e=1}^m \sum_{i=1}^n \int \mathbf{B}_e^T \mathbf{D}_i^f h \underline{\epsilon}_i^f t dA \quad (61)$$

$$\mathbf{K} \underline{u} + \mathbf{K}_c \underline{u} = \underline{F}_h \quad (62)$$

where t is the thickness of the fibre and the interfacial elements, \mathbf{K} is the stiffness of the bulk finite elements representing the fibres, \mathbf{K}_c is the stiffness of the s interfacial elements in the bonded regions and \underline{F}_h is the hygroscopic load column vector of the fibres lying in the bulk finite elements. Finally, the linear system of Eq. 62 is solved to determine the response of the network to changes in moisture content. The load column vector can also be load vector pertaining to external loads applied on network. This is illustrated in the results section where the effective stiffness response of the network is evaluated under tensile loading.

One of the main motivation of using interfacial elements is that the \mathbf{K}_c changes with mesh in such a way that the stiffness enforced in the bonded region remains the same. However, in the case of springs, the number of springs changes with discretization (may be more or less nodes in a particular bonded region) but individual spring stiffness remains same thereby leading to different stiffness in the bonded regions.

5.3 RESULTS AND DISCUSSIONS

In this section, the influence of inter-fibre bonding on the macro-scale properties of the network is assessed through the numerical results obtained using the proposed bond model. Initially, the simplified case of a two fibre network [8] is analyzed to illustrate the behavior of the bond model at a local level. Thereafter, complex networks of different coverages subjected to hygroscopic strains and tensile loading are analyzed to evaluate the relation between the sheet-level network response and the fibre bonding.

5.3.1 Simplified two fibre network (A meso-scale model)

In this case, a simple two fibre network is considered with a single bond between them. Due to periodicity, the unit cell shown in Fig. 51a only contains half fibres near the edges of the RVE. The mechanical behavior of the fibres is assumed transversely anisotropic with the elastic modulus in longitudinal direction E_l , the elastic modulus in transverse direction $E_t=E_l/6$ [68], shear modulus, $G_{lt}=E_l/10$, in-plane Poisson's ratios, $\nu_{lt}=0.3$, $\nu_{tl}=0.05$ [63] and a thickness, $t=l_f/50$. The coefficient of hygro-expansion adopted for the fibres is also anisotropic with, $\beta_l=-0.03$ (based on Jentzen creep tests on single fibres Samantray, Peerlings, Massart, and Geers [61], $\beta_t=20|\beta_l|=0.6$). The network is subjected to a unit change $\Delta\chi=1$ in moisture content, for different values of the bond interface element modulus k_h in the inter-fibre bonds. The periodic unit cell is fixed in both directions at the left bottom corner and fixed in vertical direction at the right bottom corner, allowing

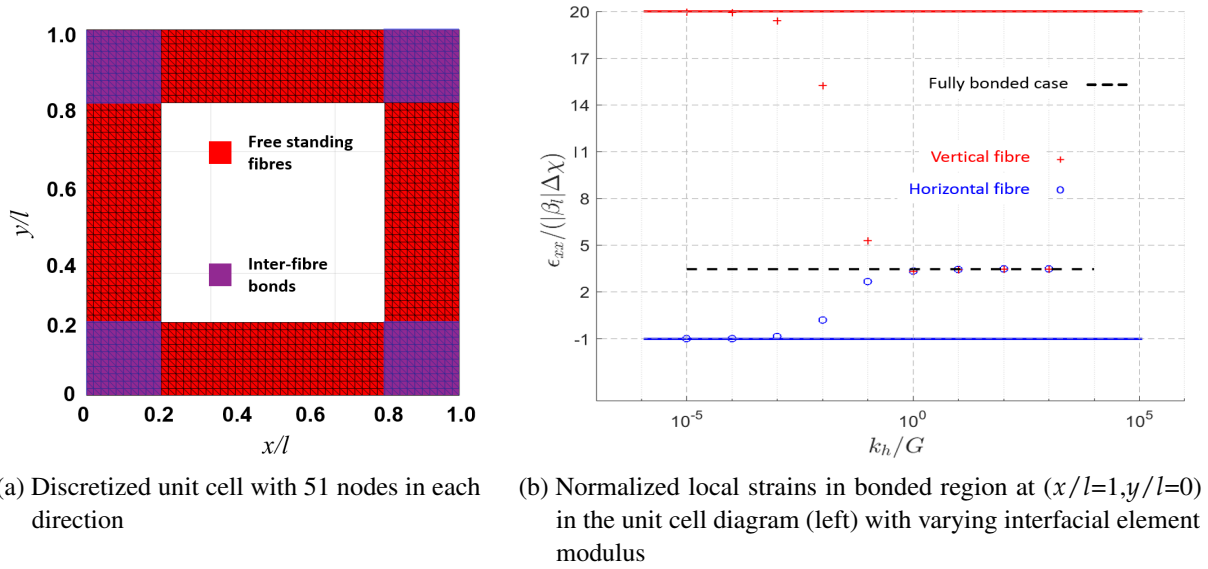


Figure 51: A two fibre meso-scale idealized network subjected to hygroscopic strain.

expansion in both directions.

In the bond region located at the right corner of the unit cell in Fig. 51a, the horizontal fibre has a low hygro-expansivity in the horizontal direction as compared to the vertical fibre. When the fibres are loosely bonded with a low value of k_h , they behave independently, which leads to the development of negative local strains in the horizontal fibre, corresponding to -1 when normalized with $|\beta_l|\Delta\chi$ as shown in Fig. 51b. Similarly, a positive local strain (normalized) with a higher value corresponding to the $\frac{\beta_t}{\beta_l}=20$ is reached in the horizontal direction for the vertical fibre.

As the bonding between the fibres becomes stiffer (k_h increases), an interaction occurs between the fibres due to their different directional expansion coefficients. This induces an increase of the local strains ϵ_{xx} (normalized with $|\beta_l|$ as $\Delta\chi=1$) of the horizontal fibre and a decrease in the local strains ϵ_{xx} in the vertical fibre. When the interfacial element modulus k_h , is equal to the shear modulus of the fibres (representing the 3D case with perfect bonding), the local strains in both fibres attain almost equal values. At higher values of k_h , both local strains are identical. Also, this strain is found similar to the one obtained for the same problem by assuming that the fibres are fully bonded in this inter-fibre bonds as noticed in Fig. 51b (as used in Samantray, Peerlings, Massart, and Geers [60], where no relative displacement was allowed). As expected, the bond model at higher k_h reduces to the case where the fibres are completely bonded. for this meso-scale model idealization of a paper network.

Therefore, it can concluded that different bond properties trigger different local strains in the fibres, not captured in earlier work assuming fully coupled fibres in the bonds.

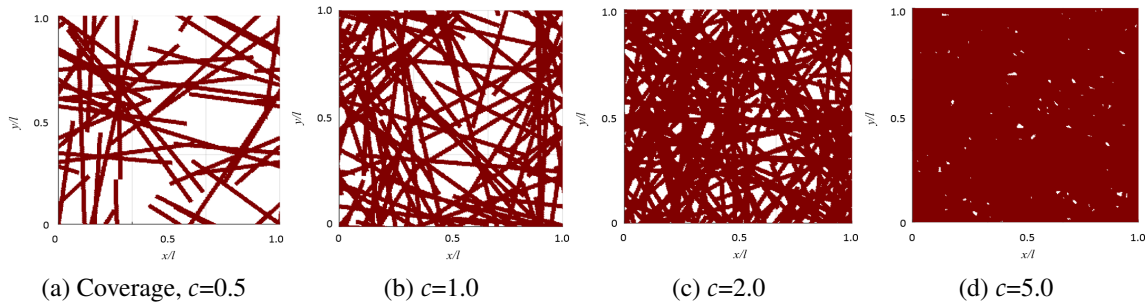


Figure 52: Random isotropic networks in a periodic unit cell.

5.3.2 Complex networks

In the present subsection, more complex networks are considered with a nearly isotropic orientation distribution of fibres for coverage, $c=0.5, 1.0, 2.0, 5.0$ as shown in periodic unit cell of length, l in Fig. 52. The paper fibres are transversely anisotropic with a longitudinal elastic modulus E_l , transverse elastic modulus $E_t=E_l/6$, shear modulus, $G=E_l/10$ and the dimensions as mentioned earlier. The in-plane Poisson's ratios are $\nu_{lt} = 0.3$ and $\nu_{tl} = 0.05$. The dimensions of the unit cell and fibres have been detailed before. The size of the finite element discretization adopted for the complex networks were taken sufficiently fine to obtain converged results.

5.3.3 Hygro-expansion

The hygro-mechanical response of these complex networks with finite stiffness bonds is next assessed by subjecting it to a unit change in moisture content, $\Delta\chi=1$ for a varying bond element modulus (k_h) using the same boundary conditions as in simplified two fibre network. A range of values of k_h was used for the inter-fibre bonds, see Fig. 53. The time taken for the simulations ranges from 17 to 330 mins. For all coverages, at a low value of the interfacial element modulus k_h (region A), the normalized effective hygro-expansivity in both direction is equal to the longitudinal swelling of a single fibre that is completely free in the considered periodic framework. At low k_h , the fibres are not bonded or very loosely connected with each other. Therefore, there is no interaction between the transverse swelling of a given fibre and the longitudinal swelling of another. As a result, the high transverse swelling of fibres cannot be transferred through the network and the network expands by longitudinal swelling of fibres only. This situation approximates fibre bonds that act as pinjoints only where only the longitudinal expansion governs the entire network. The lateral expansion of fibres does not have any influence on the macro-level response of the network. This explains the lower hygro-expansivity in both directions in the network. Moreover, in Fig. 54a and 55a, it can be observed that fibres in the network have rather independent strains (normalized with $|\beta_l|\Delta\chi$, $\Delta\chi=1$), as a consequence of the absence of bonding between them.

With an increase of the interfacial element modulus k_h to a value corresponding to the fibre shear modulus (region B in Fig. 53), an increased interaction takes place between the fibres. As a result, the transverse hygroscopic swelling of one fibre may cause another fibre to swell more through these inter-fibre bonds. Therefore, a larger average hygro-expansivity in the networks emerges. In Fig. 54b and 55b, the strain distributions in the bond regions and free standing parts of fibres of the

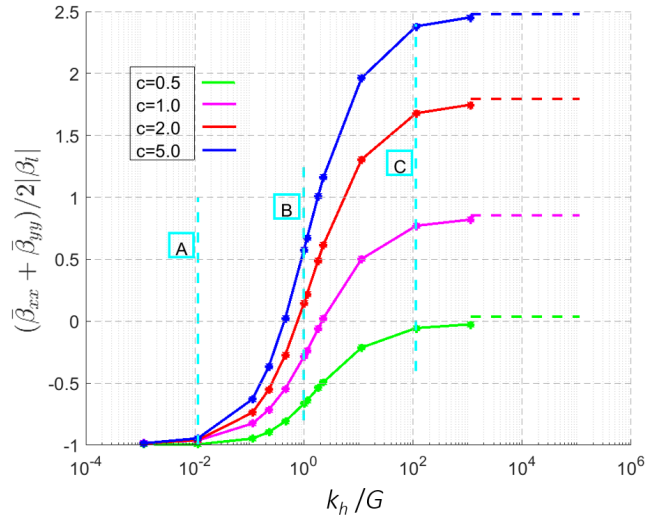


Figure 53: Normalized effective hygro-expansivity of the networks averaged in both direction vs the ratio of bond stiffness and shear modulus of fibre. The dashed lines represent the case of fully coupled bonding between fibres.

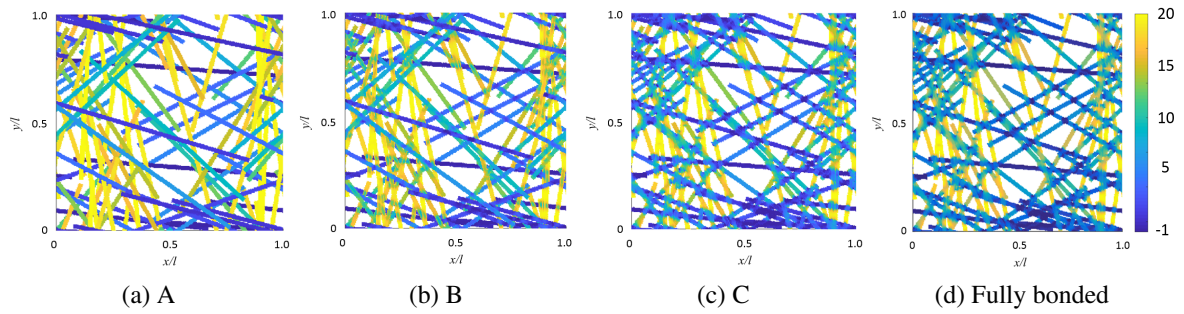


Figure 54: Strain distribution $\epsilon_{xx}/|\beta_l|$ in the network of coverage, $c=1.0$.

network with $c=1.0$ and $c=5.0$ are affected by the partial kinematic constraint. Also, it is worth to note that the network with higher coverage have high fibre density, which causes a higher average expansivity as compared to lower coverage at this value of k_h .

With further increase of k_h , the average expansivity further increases for the networks of all coverages. The local strain distribution plots in Fig. 54c and 55c demonstrate more interaction between fibres, triggering different strain distributions in the fibre bond regions when compared to free standing regions. Note the tendency of fibres in a particular bond to attain identical strain values as the interfacial element modulus rises. As expected, the strain distribution in the network becomes similar to the earlier case in Fig. 54d and 55d, for which fibres are fully bonded. Likewise, the effective hygro-expansivity tends towards the same limit value for fibres. Hence, the sheet-scale results for rigid bonds is recovered as a limit case by the current bond model in the higher limit of k_h .

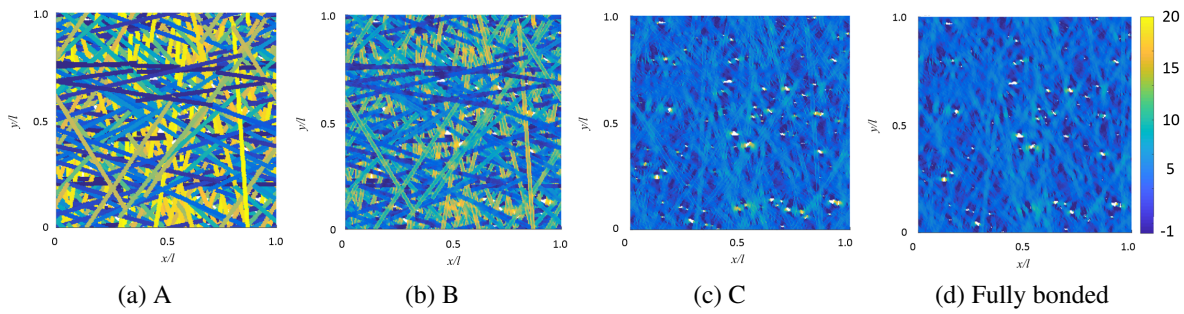


Figure 55: Strain distribution $\epsilon_{xx}/|\beta_l|$ in the network of coverage, $c=5.0$.

5.3.4 Tensile loading

In order to understand the effect of bonding between fibres on the effective stiffness of the nearly isotropic networks, they are subjected to an external uniaxial tensile load in the absence of hygroscopic strains. As can be noticed in Fig. 56, in the lower limit of the bond stiffness modulus k_h , the

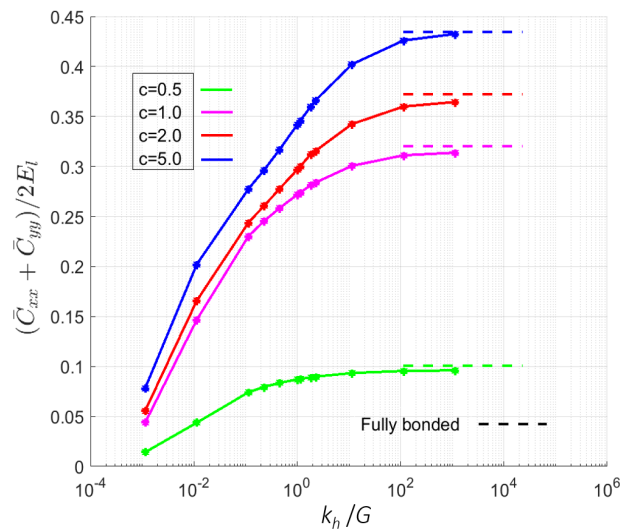


Figure 56: Normalized effective stiffness of networks averaged in both direction vs the ratio of the bond stiffness versus the fibre shear modulus. The dashed lines represent the case of fully coupled bonding between fibres.

fibres are loosely connected with each other at the inter-fibre bonds. This leads to less interaction between fibres, and hence a reduced ability to transfer stresses between fibres in the network. Since the effective stiffness of the fibrous network mostly depends on the ability of single fibres to transmit stresses, it results in a low effective stiffness of the networks for all coverages. As the bonding between the fibres becomes stiffer (k_h increases), the effective stiffness response of the networks also enhances as expected. Like in the previous case, for high values of k_h , the average stiffness of the networks approaches the case of full kinematic constraints between fibres in the bonded regions. Furthermore, as expected, the higher coverages exhibit a higher stiffness due to presence of more bonds as the number of fibres is higher. Also, for a particular value of k_h , a lower coverage network has fewer bonds between fibres as compared to a higher coverage. Therefore, it has a relatively reduced ability to transfer the stresses as compared to a network with higher coverage, resulting

in less effective stiffness. It can be seen in Fig. 56 that networks with higher coverage have higher effective stiffness for a particular value of k_h .

Based on the response of networks to hygro-expansion and tensile loading, some conclusions emerge. Firstly, a different effective response for each coverage results for different values of the bond stiffness. Therefore, even after relaxation of the kinematic constraints between fibres in the bonded regions of the network, the coverage still plays an essential role in determining the hygro-mechanical response of networks. This is consistent with earlier findings on the effect of coverage on hygro-expansivity [60, 61]. Even though at a high value of k_h the rigid bond case is recovered, the observed trend may be different. Having said this, the LS-XFEM method remains valid and attractive. Next, for each coverage, the effective response of network at $k_h=G$ (the value which describes the 3D case with perfect bonding), is substantially lower with respect to the 2D rigid case. This outlines the effect of the kinematics of the bond on the macroscopic response of the networks and highlights the limitation of the rigid bond assumption.

5.3.5 Anisotropy

The effect of the bond stiffness on the sheet-scale response for anisotropic networks is further studied here. The orientation of the generated fibres in a network representing paper can be described by a probability density function based on Cox [17] as represented in Fig. 57

$$f(\theta) = \frac{1}{\pi} \frac{1 - q^2}{1 + q^2 - 2q \cos(2\theta)} \quad (63)$$

where, θ is the angle between the fibre and the machine direction $-\pi/2 < \theta < \pi/2$ and q is a

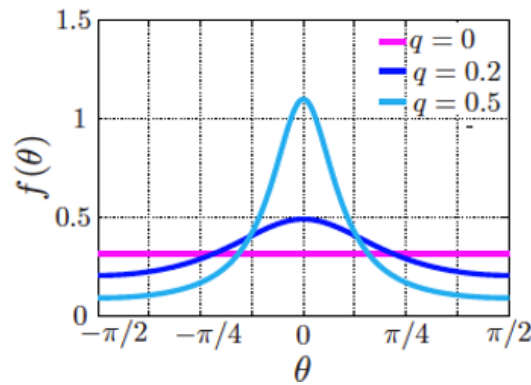


Figure 57: Probability distribution function for fibre orientations in networks with different anisotropy levels [8].

measure of the anisotropy of network.

In this study, networks of coverage, $c=2.0$ are considered with three different degrees of anisotropy, $q=0.25, 0.5$ and 0.75 respectively. These networks are subjected to a change in moisture content (hygroscopic loading) in one case and a uniaxial tensile loading in other, as done for the previous cases.

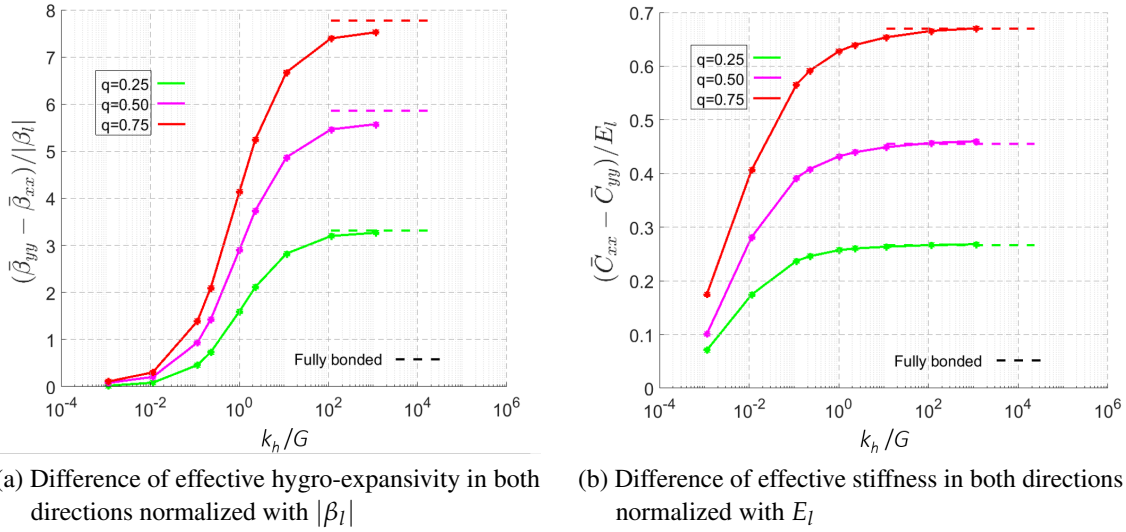


Figure 58: Anisotropic response of networks with a varying interfacial element modulus k_h .

For rigidly connected inter-fibre bonds (dashed line in Fig. 58a) more fibres oriented along the machine direction for $q=0.25$ entail a larger expansion in the cross direction of the network at the sheet-level, as $\beta_t=20\beta_l$ for each individual fibre. The transverse expansivity of these fibres oriented close to the machine direction becomes more aligned with the network cross-direction for $q=0.25$ as compared to $q=0.0$. This effect becomes more pronounced for higher values of $q=0.75$ leading to a higher hygro-expansivity in cross-direction of the networks for full bonding.

For the developed bond model, at a low value of k_h , the fibres in the networks behave like pinjoint fibres exhibiting independent strains pertaining to the local longitudinal strain of each of the fibres ($|\beta_l|\Delta\chi, \Delta\chi=1$) in both the machine and cross directions irrespective of the values of q . Therefore, in Fig. 58a, it can be observed that the difference between the effective hygro-expansivity coefficients in both directions almost vanishes. As the bonding increases between fibres, the difference between the expansivity of the networks in vertical and horizontal directions increases, implying a higher degree anisotropy in the response at higher q values.

Let us consider the case where the networks of different anisotropy are subjected to tensile loading. In terms of the effective stiffness of networks, considering the full kinematic constraint case for $q=0.25$ with more fibres oriented along the machine direction compared to cross-direction results in a higher stiffness in the machine direction as the $E_l=6E_t$ for the fibres. Therefore, Fig. 58b shows that as the anisotropy increases the effective stiffness increases in machine direction, and hence also the difference in effective stiffness in both directions. A similar trend is again observed in the effective stiffness for different values of the bond stiffness for each of the values of q under consideration. Therefore, the assumption of fully coupled bonding between fibres is not appropriate for predicting the anisotropic response of a paper fibre network because, it depends significantly on the extent of kinematic constraints or bonding between the fibres in the network.

5.4 CONCLUSIONS

In this chapter, the influence of bonding between fibres at inter-fibre bonds on the sheet-level behavior of paper fibrous networks subjected to tensile loading and hygro-expansion was studied. The response of individual fibres was considered to be hygro-elastic for the sake of simplicity.

Initially, a random fibrous network is generated with rectangular shaped fibres. These fibres are generated sequentially such that each fibre lies in a separate layer. Periodic boundary conditions are imposed for all the configurations considered. The entire network is discretized with triangular finite elements numbered in the same sequence as the fibres. In the bond regions, an additional triangular interfacial element is added between each couple of fibres in contact, allowing both fibres to be partially coupled with relative displacements between them. The extent to which both fibres in a bond undergo relative displacements depends on the stiffness modulus k_h of the bond represented by the interfacial element. In order to investigate the influence of this modulus (bond stiffness) on the macro-scale response of the networks, numerical simulations for hygro-expansion and tensile uniaxial loading have been performed.

1. At low values of k_h , the macro-level hygro-expansive response corresponds to the individual/single fibre longitudinal expansion in a free state. At high values of k_h , the corresponding macro-level response tends towards the fully coupled case for both hygro-expansion and tensile load cases.

2. Given the substantial difference between the effective hygro-expansivity of a particular network at $k_h=G$ and the fully bonded case, it is concluded that the extent of kinematic constraints in the bonds are important in influencing the sheet-scale behavior of the network. Hence, the bond model with $k_h=G$ (representing the physics between the mid-plane of fibres) is a more realistic approach for predicting the hygro-mechanical behavior of paper.

3. At different coverages, a different effective response of the network results for the bond model. This is in accordance with earlier findings Samantray, Peerlings, Massart, and Geers [60, 62].

4. The anisotropic response at the sheet-level also increases with an increase in k_h and vice-versa highlighting significance of the bonding between fibres.

Therefore, clear insights have been obtained on the variability of the sheet-scale hygro-mechanical response of fibrous networks at different values of the bonding stiffness between fibres. Moreover, the degree to which the anisotropic response of the network is affected by the bond modulus in the inter-fibre bonds is also studied for anisotropic orientation fibre distributions. This study also showed that with relatively low computational efforts an adequate representation of 3D fibres in a two dimensional framework can be made using the bond model.

In future, this work could be extended further by adopting a moisture dependent interfacial element modulus so as to study its role on the effective hygro-expansivity of network. However, this can be a difficult task as its formulation can be better achieved by a comprehensive experimental characterization. Also, the statistical variation of the bond properties like stiffness of the interfacial element in the bonds shall be taken in to account.

Another possible scope of future work would be to investigate the hygro-inelastic response of the networks. This requires include modeling of the plastic deformation in the fibres (Samantray, Peerlings, Massart, and Geers [62]), still preserving the interfacial elements in bonds so as to understand their role on the development of irreversible deformations in the network at different coverages.

As a further extension, the interfacial elements can be extended to account for a non-linear response. Furthermore, a damage model can be incorporated in these interfacial elements, so that at certain stress levels bond failure is induced and the fibres in the inter-fibre bonds will get detached. In this case, a suitable relation may be developed between the k_h and damage variable by a relevant methodology.

CONCLUSIONS AND FUTURE WORK

In this thesis, the influence of the hygro-mechanical response of paper fibres at the scale of paper sheet was investigated. For this purpose, a complex fibrous network was modeled using an advanced numerical discretization scheme to describe their complex geometries. Next, the irreversible strains in paper sheets dried under restraint is modeled using a numerical model. Thereafter, the time-dependent response of paper fibres subjected to changes in moisture and external loading is adequately captured by adopting a suitable creep model. After a thorough analysis of the results, the micro-level parameters influencing the macro-level behavior of paper were identified. Up to this point, the fibres were assumed to be fully constrained in the bonds. In order to determine the influence of bonding between fibres on the sheet-scale response of a paper network, the kinematic constraints between fibres were relaxed in the bonds. This was achieved by the bond model developed in Chapter 5 of the thesis.

6.1 RESULTS AND DISCUSSION

With the models developed and the results obtained, a better understanding of the fine-scale parameters influencing the sheet-level hygroscopic swelling of paper is achieved. Hence, the central objective of the thesis has been properly addressed.

In response to the research questions formulated in the introduction of the thesis, the results obtained that address each of them are enumerated briefly in this section.

Modeling the complex geometry in a fibrous network accurately with less computational effort than in conforming finite element discretization.

The fibres in a network are represented by randomly generated rectangular fibres with an anisotropic orientation distribution function within a periodic unit cell framework. Generally, in such complex networks, capturing the geometry of fibres poses a big challenge as it requires the use of strongly refined meshes, leading to large computational efforts.

In the proposed approach, each fibre is implicitly described by a level-set function that is coupled with XFEM to compute the hygro-mechanical response of the overall network. In the LS-XFEM formalism, the fibre edges are tracked by nodal values of a level-set function in the discretized geometry, employing a relatively coarse grid in comparison with the reference solution. The solution obtained (local fields like displacements, stresses and strains) is validated by comparison with a standard FEM (reference) solution computed using a very fine conforming mesh. Therefore, the results by LS-XFEM formalism demonstrate its ability to capture the fibre edges in a sufficiently accurate manner in a complex geometry, with a lower computational system size. This is more advantageous for modeling of a 3D network.

Modeling the irreversibility mechanism at the fibre level and its sheet-scale dependence on microstructural parameters.

As noticed in experiments (Mäkelä [43]), paper fibres dried under constraint during the manufacturing process exhibit irreversible strains upon exposure to a subsequent moisture cycle, i.e. during printing operations. At the sheet-scale, such irreversible strains appear as curls, waviness and cause instabilities occurring in paper. Here, the entire sequence of events i.e from manufacturing to printing was modeled using a rate-independent kinematic hardening model at the level of fibres. The sheet-scale irreversible strains were captured qualitatively for complex paper networks of different coverages by this model.

One of the remarkable findings of these numerical simulations for the complex networks is the dependence of the magnitude of the irreversible strain on the area fractions of the free standing fibres. The irreversible strain was observed to decrease at higher coverages, containing less free standing fibres. Therefore, a better understanding of the microstructural parameters governing dimensional instabilities observed in paper was inferred.

Modeling the time dependence of paper fibres and its influence on network properties.

Over the past years, the time-dependent response of paper when subjected to a constant and fluctuating ambient humidity has been a concern, especially in packaged paper products. Therefore, a rate-dependent model was adopted to capture such time dependence of the paper network. It was

identified on the basis of experimental results (Jentzen [32] and Sedlachek [64]) obtained on single paper fibres. The model was able to capture the rate effects qualitatively and quantitatively for single fibres with an adequate agreement. With these identified parameters for single fibres, the numerical simulations were extended towards the relaxation response of complete fibre networks. The results obtained for the networks demonstrate the ability of the model to predict the response of networks at different coverages. Among the significant effects, two main observations were noted i.e. (i) a faster relaxation at lower coverages and moisture content (ii) a faster relaxation for single fibre as compared to the networks. Using this time-dependent model, the magnitude of the irreversible strains for different coverage subjected to a moisture cycle was found to increase significantly until $c=2.0$ and started to decrease after $c=3.0$.

Which type of mechanical model needs to be adopted for relaxing the kinematic constraints in the inter-fibre bonds? How does it affect the macro-scale deformation of networks of different coverages?

A bond model comprising of an interfacial element between each set of two fibres in the inter-fibre bonds is developed. The extent to which the fibres in such regions undergo relative displacements depends on the modulus k_h of the interfacial element. At the macro-scale, the network response corresponds to the longitudinal expansion of an individual fibre when low values of k_h are considered, and this for all coverages resemble to a pinjoint frame. Conversely, for a high value of k_h , the macro-level response tends to that obtained with the earlier assumption of rigid bonding between fibres. For intermediate values of the bond stiffness, the effect of the coverage on the hygro-expansive response of a network is clearly observable. For a particular coverage, the sheet-scale response at $k_h=G$ is considerably lower than the perfect bonding case. This is a clear indication of the influence of inter-fibre bonds on the macro-scale response of the network. Additionally, a similar influence of the bond stiffness k_h on the anisotropic response of the network is noticed. Therefore, the role of the stiffness of inter-fibre bonds on the sheet-scale behavior of the network has been unravelled, which paves the way for its incorporation in the nonlinear models.

The main novelties of the work performed in thesis are thus summarized as

1. Development of a framework to capture the fibre geometry with a good accuracy and limited computational efforts, applicable to a fibrous network for analyzing its hygro-mechanical behavior.
2. Modeling of the irreversible strains in single fibres through an appropriate plasticity model, allowing to study the dependency at the level of a paper network on microstructural parameters.
3. Modeling of the creep response of single paper fibres with a rate-dependent model followed by its application to complex network, allowing to analyze the relaxation response of paper networks.
4. Investigating the hygro-mechanical response in paper networks due to partially bonded fibres in the inter-fibre bonds. Further, its role is studied on the anisotropic behavior of a network at the macro-level.

6.2 FUTURE SCOPE

As stated above, even though most of the objectives of the thesis had been reached, there is still room for further improvements based on the proposed developments.

6.2.1 *Material and modeling aspects*

A. Paper network: The network of paper consists of fibres only in the present work, which can be extended to include filler materials. Also, with more experimental data and the use of statistical tools, heterogeneous properties can be assigned to different fibres in the network to represent a more realistic paper network. It will be interesting to perform simulations on such heterogeneous networks and assess the resulting sheet-level behavior.

B. Material properties: Material properties like the elastic modulus and hardening modulus were taken to be independent of the moisture content. The behavior of network to moisture changes can be further studied with these material properties being moisture dependent. Additionally, the yield stress can be formulated as a quadratic function or logarithmic function of the moisture content. Since, these require minimal implementation efforts, this path can be easily pursued.

C. Other aspects: The interfacial element model adopted to capture relative displacements in the inter-fibre bonds can be incorporated in the kinematic hardening plasticity model. This will be helpful in understanding the influence of the relaxation of kinematic constraints on the irreversible strains observed in paper at the macro-level. Moreover, the hygro-mechanical response of the network can be studied with a moisture dependent interfacial element modulus. Since, the formulation should not pose any serious difficulty, its implementation can be subject of future work.

6.2.2 *Other realms for possible exploration linked with the hygro-mechanical response of paper*

A. Modeling in three dimensions: The hygro-elastic model described earlier can be modified to model the out of plane macroscopic behaviour of curl and waviness in paper by incorporating the constitutive model in 3D. For this purpose, a moisture profile needs to be prescribed along the thickness of the sheet. The entire 3D RVE can be modelled using three dimensional finite elements like tetrahedrons/hexahedrons. The boundary conditions should be generalized and compared with the periodicity employed here in order to allow for bending. Also, the computational advantages of the LS-XFEM formalism may be more pronounced in 3D. In 3D, with the LS-XFEM formalism, the geometry can be captured accurately even with a coarse mesh with smaller system size. This would be beneficial in reduction of the computational efforts and time. At the bonded regions in the 3D framework, contact modelling is necessary to describe the interaction between fibres touching each other.

B. Including thermal effects in model: A more accurate deformation response of paper networks can be achieved by taking into consideration the thermal effects which occur in tandem with the hygroscopic changes in ambient conditions and printing operations.

C. Mechanosorptive creep modeling: Upon exposure to subsequent cyclic humidity, creep accelerates which is termed as mechanosorptive creep. Many mechanisms have been suggested to explain this phenomena. Modeling these mechanisms to simulate mechanosorptive creep in paper fibres, in order to study its influence on the rate effects of a network subjected to cyclic humidity, forms an important topic to pursue in future work.

C. Other: As a part of future efforts, more experiments can be performed on the paper sheets to gain even more understanding on the behaviour of the paper sheets. Since the numerical simulations to predict the irreversible response of networks were performed until a coverage $c=10.0$, it will be interesting to run the simulations for higher coverages to observe the irreversible strains. A sensitivity analysis of the materials parameters like E_l, E_t, G_{lt} can be performed to study their effect on the sheet scale response. In the current work, the material and model parameters are assumed to be constant irrespective of the moisture content. As another future effort, these can be modelled as moisture dependent, with linear or non-linear variation with the moisture content. The plasticity models used in the current thesis assume plasticity only under tension. As a future work, these models can be extended to include plasticity in compression as well.

APPENDIX

A.1 DERIVATION OF PLASTIC MULTIPLIER AND CONSISTENT TANGENT OPERATOR

The trial stress and trial backstress represented by the return mapping algorithm are

$$\boldsymbol{\sigma}_{trial}^{f,t+\Delta t} = {}^4\mathbf{D}^f : (\boldsymbol{\epsilon}^{f,t+\Delta t} - p \boldsymbol{\epsilon}^{f,t} - h \boldsymbol{\epsilon}^{f,t+\Delta t}) \quad (64)$$

$$\bar{\mathbf{q}}_{trial}^{f,t+\Delta t} = - {}^4\mathbf{H} : \bar{\boldsymbol{\zeta}}^{f,t} \quad (65)$$

$$F_{trial}^{f,t+\Delta t} = |(\boldsymbol{\sigma}_{trial}^{f,t+\Delta t} - \bar{\mathbf{q}}_{trial}^{f,t+\Delta t}) : \vec{p}\vec{p}| - \sigma_y, F^{f,trial} \text{ is trial yield function} \quad (66)$$

Therefore, the stress and the backstress can now be computed as

$$\boldsymbol{\sigma}^{f,t+\Delta t} = \boldsymbol{\sigma}_{trial}^{f,t+\Delta t} - \Delta\gamma {}^4\mathbf{D}^f : \mathbf{N} \quad (67)$$

$$\bar{\mathbf{q}}^{f,t+\Delta t} = \bar{\mathbf{q}}_{trial}^{f,t+\Delta t} + \Delta\gamma {}^4\mathbf{H}^f : \mathbf{N}, \text{ where } \mathbf{N} = \text{sign}((\boldsymbol{\sigma}^{f,t+\Delta t} - \bar{\mathbf{q}}^{f,t+\Delta t}) : \vec{p}\vec{p}) \vec{p}\vec{p} \quad (68)$$

$$\boldsymbol{\sigma}^{f,t+\Delta t} - \bar{\mathbf{q}}^{f,t+\Delta t} = \boldsymbol{\sigma}_{trial}^{f,t+\Delta t} - \bar{\mathbf{q}}_{trial}^{f,t+\Delta t} - \Delta\gamma ({}^4\mathbf{D}^f : \mathbf{N} + {}^4\mathbf{H}^f : \mathbf{N})$$

We need to derive the expression for the plastic multiplier $\Delta\gamma$. For this, we write the yield function

$$\begin{aligned} F^{f,t+\Delta t} &= |(\boldsymbol{\sigma}^{f,t+\Delta t} - \bar{\mathbf{q}}^{f,t+\Delta t}) : \vec{p}\vec{p}| - \sigma_y \\ &= (\boldsymbol{\sigma}^{f,t+\Delta t} - \bar{\mathbf{q}}^{f,t+\Delta t}) : \vec{p}\vec{p} \text{ sign}[(\boldsymbol{\sigma}^{f,t+\Delta t} - \bar{\mathbf{q}}^{f,t+\Delta t}) : \vec{p}\vec{p}] - \sigma_y \\ &= (\boldsymbol{\sigma}^{f,t+\Delta t} - \bar{\mathbf{q}}^{f,t+\Delta t}) : \mathbf{N} - \sigma_y \\ &= (\boldsymbol{\sigma}^{f,t+\Delta t} - \bar{\mathbf{q}}^{f,t+\Delta t}) : \mathbf{N}_{trial} - \sigma_y \end{aligned}$$

Here, we have used the fact that for sufficiently small increments, we have (69)

$$\mathbf{N} = \mathbf{N}_{trial} = \text{sign}((\boldsymbol{\sigma}_{trial}^{f,t+\Delta t} - \bar{\mathbf{q}}_{trial}^{f,t+\Delta t}) : \vec{p}\vec{p}) \vec{p}\vec{p} \quad (70)$$

Now, introducing the $\boldsymbol{\sigma}^{f,t+\Delta t}$ and $\bar{\mathbf{q}}^{f,t+\Delta t}$ from Eq. (67) and (68), we have

$$\begin{aligned} F^{f,t+\Delta t} &= (\boldsymbol{\sigma}_{trial}^{f,t+\Delta t} - \bar{\mathbf{q}}_{trial}^{f,t+\Delta t}) : \mathbf{N}_{trial} - \Delta\gamma ({}^4\mathbf{D}^f : \mathbf{N}_{trial} + {}^4\mathbf{H}^f : \mathbf{N}_{trial}) : \mathbf{N}_{trial} - \sigma_y \\ &= F_{trial}^{f,t+\Delta t} - \Delta\gamma (\mathbf{N}_{trial} : {}^4\mathbf{D}^f : \mathbf{N}_{trial} + \mathbf{N}_{trial} : {}^4\mathbf{H}^f : \mathbf{N}_{trial}) \\ F^{f,t+\Delta t} &= F_{trial}^{f,t+\Delta t} - \Delta\gamma (\vec{p}\vec{p} : ({}^4\mathbf{D}^f + {}^4\mathbf{H}^f) : \vec{p}\vec{p}) \end{aligned}$$

The yield condition expresses that $F^{f,t+\Delta t}$ should vanish, which gives the plastic multiplier $\Delta\gamma$ as

$$\Delta\gamma = \frac{F_{trial}^{f,t+\Delta t}}{\vec{p}\vec{p} : ({}^4\mathbf{D}^f + {}^4\mathbf{H}^f) : \vec{p}\vec{p}} \quad (71)$$

To derive the consistent elastoplastic material tangent, ${}^4\mathbf{D}_{ep}$, the plastic multiplier is linearized as

$$\delta\gamma = \frac{\delta F_{trial}^{f,t+\Delta t}}{\vec{p}\vec{p} : ({}^4\mathbf{D}^f + {}^4\mathbf{H}^f) : \vec{p}\vec{p}} = \frac{\mathbf{N}_{trial} : \delta\boldsymbol{\sigma}_{trial}^{f,t+\Delta t}}{\vec{p}\vec{p} : ({}^4\mathbf{D}^f + {}^4\mathbf{H}^f) : \vec{p}\vec{p}} \quad (72)$$

The stress operator is linearized as

$$\delta\boldsymbol{\sigma}^{f,t+\Delta t} = \delta\boldsymbol{\sigma}_{trial}^{f,t+\Delta t} - \delta\gamma \mathbf{4D}^f : \mathbf{N}_{trial}$$

Here, the contribution of $\delta\bar{\boldsymbol{q}}_{trial}^{f,t+\Delta t} = 0$ as it depends on $\bar{\boldsymbol{\xi}}^{f,t}$ of previous time step. Substitution of $\delta\gamma$ according to Eq. (72) now gives

$$\begin{aligned} \delta\boldsymbol{\sigma}^{f,t+\Delta t} &= \delta\boldsymbol{\sigma}_{trial}^{f,t+\Delta t} - \mathbf{4D}^f : \mathbf{N}_{trial} \frac{\mathbf{N}_{trial} : \delta\boldsymbol{\sigma}_{trial}^f}{\bar{\boldsymbol{p}}\bar{\boldsymbol{p}} : (\mathbf{4D}^f + \mathbf{4H}^f) : \bar{\boldsymbol{p}}\bar{\boldsymbol{p}}} \\ &= \mathbf{4D}^f : \delta\boldsymbol{\epsilon}^{f,t+\Delta t} - \frac{1}{\bar{\boldsymbol{p}}\bar{\boldsymbol{p}} : (\mathbf{4D}^f + \mathbf{4H}^f) : \bar{\boldsymbol{p}}\bar{\boldsymbol{p}}} \mathbf{4D}^f : \mathbf{N}_{trial} \mathbf{N}_{trial} : \mathbf{4D}^f : \delta\boldsymbol{\epsilon}^{f,t+\Delta t} \\ &= \left(\mathbf{4D}^f - \frac{\bar{\boldsymbol{p}}\bar{\boldsymbol{p}} : \mathbf{4D}^f \mathbf{4D}^f : \bar{\boldsymbol{p}}\bar{\boldsymbol{p}}}{\bar{\boldsymbol{p}}\bar{\boldsymbol{p}} : (\mathbf{4D}^f + \mathbf{4H}^f) : \bar{\boldsymbol{p}}\bar{\boldsymbol{p}}} \right) : \delta\boldsymbol{\epsilon}^{f,t+\Delta t} \end{aligned} \quad (73)$$

Therefore, the consistent tangent operator is denoted as

$$\mathbf{D}_{ep} = \mathbf{4D}^f - \frac{(\bar{\boldsymbol{p}}\bar{\boldsymbol{p}} : \mathbf{4D}^f \mathbf{4D}^f : \bar{\boldsymbol{p}}\bar{\boldsymbol{p}})}{\bar{\boldsymbol{p}}\bar{\boldsymbol{p}} : (\mathbf{4D}^f + \mathbf{4H}^f) : \bar{\boldsymbol{p}}\bar{\boldsymbol{p}}} \quad (74)$$

A.2 NON-LINEAR GLOBAL EQUILIBRIUM EQUATIONS

In order to predict the irreversible response of a fibrous network as discussed in the first section, a finite element scheme is adopted using a non-linear incremental iterative methodology based on the Newton Raphson scheme. The fibrous network in the periodic unit cell is discretized using a regular grid with constant strain triangular finite elements. The finite elements with their centroid lying inside the fibres contribute to the stiffness and hygroscopic load in the assembly of the global system of equations, while the other elements lie in voids. Now, as we are incorporating the hygro-expansion model in the non-linear equilibrium equations, it is important to obtain the correct initial guess of the plastic multiplier $\Delta\gamma$ in the first iteration of every time increment to achieve convergence. Therefore, this is followed for only the first iteration of each time increment. So,

$$\Delta^p \epsilon^f = \Delta\gamma \mathbf{N} = \Delta\gamma \mathbf{N}_{trial} \quad (75)$$

Now, the stress at time $t+\Delta t$ is denoted by

$$\begin{aligned} \sigma^{f,t+\Delta t} &= \sigma^{f,t} + \Delta\sigma^f \\ &= \sigma^{f,t} + {}^4\mathbf{D}^f : (\Delta\epsilon^f - \Delta^h\epsilon^f - \Delta^p\epsilon^f) \\ &= \sigma^{f,t} + {}^4\mathbf{D}^f : (\Delta\epsilon^f - \Delta^h\epsilon^f - \Delta\gamma \mathbf{N}_{trial}) \end{aligned} \quad (76)$$

$$= \sigma_{trial}^{f,t+\Delta t} - \Delta\gamma {}^4\mathbf{D}^f : \mathbf{N}_{trial}, \quad \sigma_{trial}^{f,t+\Delta t} = \sigma^{f,t} + {}^4\mathbf{D}^f : (\Delta\epsilon^f - \Delta^h\epsilon^f) \quad (77)$$

Now, the plastic multiplier as derived earlier and the trial yield function are represented as

$$\Delta\gamma = \frac{F_{trial}^{f,t+\Delta t}}{(\vec{p}\vec{p} : ({}^4\mathbf{D}^f + {}^4\mathbf{H}^f) : \vec{p}\vec{p})}, \quad F_{trial}^{f,t+\Delta t} = |(\sigma_{trial}^{f,t+\Delta t} - \bar{q}_{trial}^{f,t+\Delta t}) : \vec{p}\vec{p}| - \sigma_y \quad (78)$$

Substituting the value of $\sigma_{trial}^{f,t+\Delta t}$ in $F_{trial}^{f,t+\Delta t}$, we have

$$\begin{aligned} F_{trial}^{f,t+\Delta t} &= |(\sigma^{f,t} + {}^4\mathbf{D}^f : \Delta\epsilon^f - {}^4\mathbf{D}^f : \Delta^h\epsilon^f - \bar{q}^{f,t}) : \vec{p}\vec{p}| - \sigma_y^{t+\Delta t} \\ &= |(\sigma^{f,t} + {}^4\mathbf{D}^f : \Delta\epsilon^f - {}^4\mathbf{D}^f : \Delta^h\epsilon^f - \bar{q}^{f,t}) : \mathbf{N}_{trial} - (\sigma_y^t + \Delta\sigma_y)| \\ &= ((\sigma^{f,t} - \bar{q}^{f,t}) : \mathbf{N}_{trial} - \sigma_y + ({}^4\mathbf{D}^f : \Delta\epsilon^f - {}^4\mathbf{D}^f : \Delta^h\epsilon^f) : \mathbf{N}_{trial} - \Delta\sigma_y) \end{aligned}$$

Assuming continued plastic flow in the same direction, we have $\mathbf{N}_{trial} = \mathbf{N}^t$ and hence, $(\sigma^{f,t} - \bar{q}^{f,t}) : \mathbf{N}^t - \sigma_y = |(\sigma^{f,t} - \bar{q}^{f,t}) : \vec{p}\vec{p}| - \sigma_y = F_{trial}^{f,t} = 0$, this simplifies to

$$F_{trial}^{f,t+\Delta t} = ({}^4\mathbf{D}^f : \Delta\epsilon^f - {}^4\mathbf{D}^f : \Delta^h\epsilon^f) : \mathbf{N}_{trial} - \Delta\sigma_y, \quad (79)$$

Substituting this expression for $F_{trial}^{f,t+\Delta t}$ in the plastic multiplier in Eq. 71, we have,

$$\Delta\gamma = \frac{({}^4\mathbf{D}^f : \Delta\epsilon^f - {}^4\mathbf{D}^f : \Delta^h\epsilon^f) : \mathbf{N}^t - \Delta\sigma_y}{\vec{p}\vec{p} : ({}^4\mathbf{D}^f + {}^4\mathbf{H}^f) : \vec{p}\vec{p}} \quad (80)$$

Now, substituting the value of $\Delta\gamma$ in Eq. 76, we have

$$\begin{aligned}
\sigma^{f,t+\Delta t} &= \sigma^{f,t} - {}^4\mathbf{D}^f : \Delta^h \boldsymbol{\epsilon}^f + {}^4\mathbf{D}^f : \Delta \boldsymbol{\epsilon}^f \\
&\quad - \mathbf{D}^f : \frac{({}^4\mathbf{D}^f : \Delta \boldsymbol{\epsilon}^f - {}^4\mathbf{D}^f : \Delta^h \boldsymbol{\epsilon}^f) : \mathbf{N}^t - \Delta \sigma_y \mathbf{N}^t}{\vec{p}\vec{p} : ({}^4\mathbf{D}^f + {}^4\mathbf{H}^f) : \vec{p}\vec{p}} \mathbf{N}^t \\
&= \sigma^{f,t} + \left({}^4\mathbf{D}^f - \frac{(\vec{p}\vec{p} : {}^4\mathbf{D}^f \quad {}^4\mathbf{D}^f : \vec{p}\vec{p})}{\vec{p}\vec{p} : ({}^4\mathbf{D}^f + {}^4\mathbf{H}^f) : \vec{p}\vec{p}} \right) : \Delta \boldsymbol{\epsilon}^f \\
&\quad - \left({}^4\mathbf{D}^f - \frac{(\vec{p}\vec{p} : {}^4\mathbf{D}^f \quad {}^4\mathbf{D}^f : \vec{p}\vec{p})}{\vec{p}\vec{p} : ({}^4\mathbf{D}^f + {}^4\mathbf{H}^f) : \vec{p}\vec{p}} \right) : \Delta^h \boldsymbol{\epsilon}^f + \frac{{}^4\mathbf{D}^f : \mathbf{N}^t \Delta \sigma_y}{\vec{p}\vec{p} : ({}^4\mathbf{D}^f + {}^4\mathbf{H}^f) : \vec{p}\vec{p}} \quad (81)
\end{aligned}$$

$$= \sigma^{f,t} + \mathbf{D}_{ep} : \Delta \boldsymbol{\epsilon}^f - \mathbf{D}_{ep} : \Delta^h \boldsymbol{\epsilon}^f + \frac{{}^4\mathbf{D}^f : \mathbf{N}^t \Delta \sigma_y}{\vec{p}\vec{p} : ({}^4\mathbf{D}^f + {}^4\mathbf{H}^f) : \vec{p}\vec{p}} \quad (82)$$

Therefore, we obtained the prediction of stress at $(t + \Delta t)$ based on data at t .

A.3 DERIVATION OF PLASTIC MULTIPLIER IN THE CREEP MODEL

$$\dot{\gamma} = \frac{\gamma_0}{\tau} \left(\frac{|\boldsymbol{\sigma}^{f,t+\Delta t} - \bar{\mathbf{q}}^{f,t+\Delta t} : \vec{p}\vec{p}|}{\sigma_y} \right)^{\frac{1}{m}}$$

$$\Delta\gamma = \frac{\gamma_0\Delta t}{\tau} \left(\frac{(\boldsymbol{\sigma}^{f,t+\Delta t} - \bar{\mathbf{q}}^{f,t+\Delta t}) : \mathbf{N}}{\sigma_y} \right)^{\frac{1}{m}} \quad (83)$$

$$= \frac{\gamma_0\Delta t}{\tau} \left(\frac{(\boldsymbol{\sigma}^{f,t+\Delta t} - \bar{\mathbf{q}}^{f,t+\Delta t}) : \mathbf{N}_{trial}}{\sigma_y} \right)^{\frac{1}{m}} \quad (84)$$

where $\mathbf{N} = \text{sign}((\boldsymbol{\sigma}^{f,t+\Delta t} - \bar{\mathbf{q}}^{f,t+\Delta t}) : \vec{p}\vec{p}) \vec{p}\vec{p} = \mathbf{N}_{trial}$

$$\boldsymbol{\sigma}^{f,t+\Delta t} = \boldsymbol{\sigma}_{trial}^{f,t+\Delta t} - \Delta\gamma {}^4\mathbf{D}^f : \mathbf{N}_{trial} \quad (85)$$

$$\bar{\mathbf{q}}^{f,t+\Delta t} = \bar{\mathbf{q}}_{trial}^{f,t+\Delta t} + \Delta\gamma {}^4\mathbf{H}^f : \mathbf{N}_{trial} \quad (86)$$

Substituting the expression of $\boldsymbol{\sigma}^f$ and $\bar{\mathbf{q}}^f$ from Eq. (85) and Eq. (86) respectively in Eq. (84), we have

$$\Delta\gamma = \frac{\gamma_0\Delta t}{\tau} \left[\frac{(\boldsymbol{\sigma}_{trial}^{f,t+\Delta t} - \bar{\mathbf{q}}_{trial}^{f,t+\Delta t}) : \mathbf{N}_{trial} - \Delta\gamma \mathbf{N}_{trial} : ({}^4\mathbf{D}^f + {}^4\mathbf{H}^f) : \mathbf{N}_{trial}}{\sigma_y} \right]^{\frac{1}{m}}$$

$$G(\gamma) = \Delta\gamma - \frac{\gamma_0\Delta t}{\tau} \left[\frac{(\boldsymbol{\sigma}_{trial}^{f,t+\Delta t} - \bar{\mathbf{q}}_{trial}^{f,t+\Delta t}) : \mathbf{N}_{trial} - \Delta\gamma \mathbf{N}_{trial} : ({}^4\mathbf{D}^f + {}^4\mathbf{H}^f) : \mathbf{N}_{trial}}{\sigma_y} \right]^{\frac{1}{m}} \quad (87)$$

where $G(\gamma) = 0$

Therefore, the non-linear equation to be solved for the plastic multiplier is given by Eq. (87).

A.4 DERIVATION OF MATERIAL TANGENT MODULUS

In order to derive the tangent operator, a variation of the non-linear equation obtained above in Eq. (87) is used

$$\delta\gamma = \frac{\gamma_0\Delta t}{\tau} \left[\frac{(\boldsymbol{\sigma}_{trial}^{f,t+\Delta t} - \bar{\boldsymbol{q}}_{trial}^{f,t+\Delta t}) : \mathbf{N}_{trial} - \Delta\gamma \mathbf{N}_{trial} : ({}^4\mathbf{D}^f + {}^4\mathbf{H}^f) : \mathbf{N}_{trial}}{\sigma_y} \right]^{\frac{1}{m}-1} \\ \times \frac{1}{m\sigma_y} \left[\delta\boldsymbol{\sigma}_{trial}^{f,t+\Delta t} : \mathbf{N}_{trial} - \delta\gamma \mathbf{N}_{trial} : ({}^4\mathbf{D}^f + {}^4\mathbf{H}^f) : \mathbf{N}_{trial} \right]$$

Here, $\delta\bar{\boldsymbol{q}}_{trial}^{f,t+\Delta t} = 0$ as it depends on ${}^c\boldsymbol{\epsilon}^{f,t}$ of the previous time step. (88)

Now, the above equation can be represented as

$$[1 + AA \mathbf{N}_{trial} : ({}^4\mathbf{D}^f + {}^4\mathbf{H}^f) : \mathbf{N}_{trial}] \delta\gamma = AA \mathbf{N}_{trial} : \delta\boldsymbol{\sigma}_{trial}^{f,t+\Delta t},$$

$$\text{Here } AA = \frac{\gamma_0\Delta t}{m\tau\sigma_y} \left[\frac{(\boldsymbol{\sigma}_{trial}^{f,t+\Delta t} - \bar{\boldsymbol{q}}_{trial}^{f,t+\Delta t}) : \mathbf{N}_{trial} - \Delta\gamma \mathbf{N}_{trial} : ({}^4\mathbf{D}^f + {}^4\mathbf{H}^f) : \mathbf{N}_{trial}}{\sigma_y} \right]^{\frac{1}{m}-1}$$

One thus obtains (89)

$$\delta\gamma = \frac{AA \mathbf{N}_{trial}}{1 + AA \mathbf{N}_{trial} : ({}^4\mathbf{D}^f + {}^4\mathbf{H}^f) : \mathbf{N}_{trial}} : \delta\boldsymbol{\sigma}_{trial}^{f,t+\Delta t} \quad (90)$$

Now, the stress variation is represented as

$$\delta\boldsymbol{\sigma}^{f,t+\Delta t} = \delta\boldsymbol{\sigma}_{trial}^{f,t+\Delta t} - \delta\gamma {}^4\mathbf{D}^f : \mathbf{N} \\ = \delta\boldsymbol{\sigma}_{trial}^{f,t+\Delta t} - \mathbf{D}^f : \mathbf{N}_{trial} \frac{AA \mathbf{N}_{trial}}{1 + AA \mathbf{N}_{trial} : ({}^4\mathbf{D}^f + {}^4\mathbf{H}^f) : \mathbf{N}_{trial}} : \delta\boldsymbol{\sigma}_{trial}^{f,t+\Delta t} \\ = {}^4\mathbf{D}^f : \delta\boldsymbol{\epsilon}^{f,t+\Delta t} - \frac{AA}{1 + AA \mathbf{N}_{trial} : ({}^4\mathbf{D}^f + {}^4\mathbf{H}^f) : \mathbf{N}_{trial}} \\ \times {}^4\mathbf{D}^f : \mathbf{N}_{trial} \mathbf{N}_{trial} : {}^4\mathbf{D}^f : \delta\boldsymbol{\epsilon}^{f,t+\Delta t} \quad (91)$$

$$= \left[{}^4\mathbf{D}^f - \frac{AA \Delta t {}^4\mathbf{D}^f : \mathbf{N}_{trial} \mathbf{N}_{trial} : {}^4\mathbf{D}^f}{1 + AA \mathbf{N}_{trial} : ({}^4\mathbf{D}^f + {}^4\mathbf{H}^f) : \mathbf{N}_{trial}} \right] : \delta\boldsymbol{\epsilon}^{f,t+\Delta t} \quad (92)$$

$$\delta\boldsymbol{\sigma}^{f,t+\Delta t} = {}^4\mathbf{D}_{ep}^{f,t+\Delta t} : \delta\boldsymbol{\epsilon}^{f,t+\Delta t}$$

The tangent modulus is thus obtained as

$${}^4\mathbf{D}_{ep}^{f,t+\Delta t} = {}^4\mathbf{D}^f - \frac{AA}{1 + AA \mathbf{N}_{trial} : ({}^4\mathbf{D}^f + {}^4\mathbf{H}^f) : \mathbf{N}_{trial}} {}^4\mathbf{D}^f : \vec{p}\vec{p} \otimes \vec{p}\vec{p} : {}^4\mathbf{D}^f \quad (93)$$

BIBLIOGRAPHY

- [1] J.A. Van Akker. “Some theoretical considerations on the mechanical properties of fibrous structures.” In: *The Formation and Structure of Paper. Technical Section of British Papers and Board Makers Association* 1 (1962), pp. 205–241.
- [2] M.J. Alava and R.K. Ritala. “Fracture of fibrous networks with varying fibre length.” In: *Physics Scripta* T33 (1990), pp. 155–158.
- [3] J. Alfthan. “A simplified network model for mechanosorptive creep in paper.” In: *Journal of Pulp and Paper Science* 29 (2003), pp. 228–234.
- [4] J. Alfthan. “The effect of humidity cycle amplitude on accelerated tensile creep of paper.” In: *Mechanics of Time-Dependent Materials* 8 (2004), pp. 289–302.
- [5] J. Astrom, S. Saarinen, K. Niskanen, and J. Kurkijarvi. “Microscopic mechanics of fiber networks.” In: *Journal of Applied Physics* 75 (1994), pp. 2383–2392.
- [6] P. Bergstrom. “Modelling mechanics of fibre network using discrete element method.” In: *Thesis for Licentiate degree, Mid-Sweden University* 8 (2018), pp. 289–302.
- [7] E. Bosco, R.H.J. Peerlings, and M.G.D. Geers. “Explaining irreversible hygroscopic strains in paper: a multi-scale modelling study on the role of fibre activation and micro-compressions.” In: *Mechanics of Materials* 91 (2015), pp. 76–94.
- [8] E. Bosco, R.H.J. Peerlings, and M.G.D. Geers. “Predicting hygro-elastic properties of paper sheets based on an idealized model of the underlying fibrous network.” In: *International Journal of Solids and Structures* 56-57 (2015), pp. 43–52.
- [9] E. Bosco, R.H.J. Peerlings, and M.G.D. Geers. “Asymptotic homogenization of hygro-thermo-mechanical properties of fibrous networks.” In: *International Journal of Solids and Structures* 115-116 (2017), pp. 180–189.
- [10] C. Boutin. “Microstructural effects in elastic composites.” In: *International Journal of Solids and Structures* 33 (1996), pp. 1023–1051.
- [11] J. Brezinski. “The creep properties of paper.” In: *Technical Association of Pulp and Paper Industry* 39 (1956), pp. 116–128.
- [12] C.A. Bronkhorst. “Modeling paper as a two-dimensional elastic–plastic stochastic network.” In: *International Journal of Solids and Structures* 40 (2003), pp. 5441–5454.
- [13] V.L. Byrd. “Effect of relative humidity changes during creep on handsheet properties of paper.” In: *Technical Association of Pulp and Paper Industry* 55 (1972), pp. 247–252.
- [14] T.R. Chandrupatla and A.D. Belgundu. *Introduction to Finite Elements in Engineering*. 3rd Edition. Pearson, 2002.
- [15] T.W. Clyne, A.E. Markaki, and J.C. Tan. “Mechanical and magnetic properties of metal fibre networks with and without a polymeric matrix.” In: *Composites Science and Technology* 65 (2005), pp. 2492–2499.

- [16] D.W. Coffin and S.B. Boese. "Tensile creep behavior of single fibers and paper in a cyclic humidity environment." In: *Proceedings of the 3rd International Symposium: Moisture and Creep Effects on Paper, Board and Containers, New Zealand* (1997), pp. 39–52.
- [17] H. Cox. "The elasticity and strength of paper and other fibrous materials." In: *British Journal of Applied Physics* 3 (1952), pp. 72–79.
- [18] C. Daux, N. Moes, J. Dolbow, N. Sukumar, and T. Belytschko. "Arbitrary branched and intersecting cracks with the extended finite element method." In: *International Journal for Numerical Methods in Engineering* 48 (2000), pp. 1741–1760.
- [19] A. DeMaio and T. Patterson. "Influence of bonding on the tensile creep behavior of paper in a cyclic humidity environment." In: *Mechanics of Time Dependent Material* 10 (2006), pp. 17–33.
- [20] J. Dirrenberger, S. Forest, and D. Jeulin. "Towards gigantic RVE sizes for 3D stochastic fibrous networks." In: *International Journal of Solids and Structures* 51 (2014), pp. 359–376.
- [21] A. Erkkila, T. Leppanen, M. Ora, T. Tuovinen, and A. Puurtinen. "Hygroexpansivity of anisotropic sheets." In: *Composites Science and Technology* 30 (2015), pp. 325–334.
- [22] J. Guedes and N. Kikuchi. "Preprocessing and postprocessing for materials based on the homogenization method with adaptive finite element methods." In: *Computer Methods in Applied Mechanics and Engineering* 83 (1990), pp. 143–198.
- [23] C.C. Habeger and D.W. Coffin. "The role of stress concentrations in accelerated creep and sorption-induced physical aging." In: *Journal of Pulp and Paper Science* 26 (2000), pp. 145–157.
- [24] H.W. Haslach. "The mechanics of moisture accelerated tensile creep in paper." In: *Technical Association of Pulp and Paper Industry Journal* 77 (1994), pp. 179–186.
- [25] H.W. Haslach. "Time-dependent mechanisms in fracture of paper." In: *Mechanics of Time Dependent Materials* 13 (2009), pp. 11–35.
- [26] M. Henriksson, L.A. Berglund, P. Isaksson, T. Lindstrom, and Nishino Takashi. "Cellulose nanopaper structures of high toughness." In: *Biomacromolecules* 9 (2008), pp. 2492–2499.
- [27] S. Heyden. "Network modelling for the evaluation of mechanical properties of cellulose fibre fluff." In: *PhD Thesis. Lund University* (2000).
- [28] R.L. Hill. "The creep behavior of individual pulp fibers under tensile stress." In: *Technical Association of Pulp and Paper Industry Journal* 50 (1967), pp. 432–440.
- [29] P. Hoffmeyer. "Non-linear creep caused by slip plane formation." In: *Wood Science and Technology* 27 (1993), pp. 321–335.
- [30] P. Hoffmeyer and R.W. Davidson. "Mechano-sorptive creep mechanism of wood in compression and bending." In: *Wood Science and Technology* 23 (1989), pp. 215–227.
- [31] D.G. Hunt and C.F. Shelton. "Longitudinal moisture-shrinkage coefficients of softwood at the mechano-sorptive creep limit." In: *Wood Science Technology* 22 (1988), pp. 199–210.
- [32] C.A. Jentzen. "The effect of stress applied during drying on the mechanical properties of individual pulp fibres." In: *Doctoral Dissertation. Appleton WI* (1964), pp. 335–344.
- [33] Frans Johanson and Josef Kubát. "Measurements of Stress Relaxation in Paper." In: *Svensk Papperstidning* 20 (1967), pp. 822–832.

- [34] A. Karakoc, E. Hiltunen E., and J. Paltakari J. “Geometrical and spatial effects on fiber network connectivity.” In: *Composite Structures* 168 (2017), pp. 335–344.
- [35] C.T. Koh and M.L. Oyen. “Branching toughens fibrous networks.” In: *Journal of the mechanical behavior of biomedical materials* 12 (2012), pp. 74–82.
- [36] A. Kulachenko and T. Uesaka. “Direct simulations of fiber network deformation and failure.” In: *Mechanics of Materials* 51 (2012), pp. 1–14.
- [37] P.A. Larsson and L. Wagberg. “Influence of fibre–fibre joint properties on the dimensional stability of paper.” In: *Cellulose* 15 (2008), pp. 515–525.
- [38] Y. Lee and I. Jasiuk. “Apparent elastic properties of random fiber networks.” In: *Computational Materials Science* 79 (2013), pp. 715–723.
- [39] J.X. Liu, Z.T.Chen, H. Wang H., and K.C. Li. “Elasto-plastic analysis of influence of bond deformability on the mechanical behavior of fiber networks.” In: *Theoretical and Applied Fracture Mechanics* 55 (2011), pp. 131–139.
- [40] R. Mao, S. Goutianos, and T. Peijs. “Effect of inter-fibre bonding on the fracture of fibrous networks with strong interactions.” In: *International Journal of Solids and Structures* 136-137 (2018), pp. 271–278.
- [41] R. Mao, S. Goutianos, W. Tu, N. Meng, S. Chen, and T. Peijs. “Modelling the elastic properties of cellulose nanopaper.” In: *Materials and Design* 126 (2017), pp. 183–189.
- [42] A. Martensson. “Mechanosorptive effects in wooden material.” In: *Wood Science and Technology* 28 (1994), pp. 437–449.
- [43] P. Mäkelä. “Comparison of test methods for measurement of in-plane hygroexpansivity.” In: *Innventia Report No:122* (2010).
- [44] H.R. Motamedian and A Kulachenko. “Simulating the hygro-expansion of paper using a 3D beam network model and concurrent multiscale approach.” In: *International Journal of Solids and Structures* 161 (2019), pp. 23–41.
- [45] K. Niskanen. *Paper Physics (Papermaking science and technology)*. 2nd Edition. Fapet Oy, 1998.
- [46] K. Niskanen, S.J. Kuskowski, and C.A. Bronkhorst. “Dynamic hygro-expansion of paperboards.” In: *Nordic Pulp Paper Research Journal* 12 (1997), pp. 103–110.
- [47] L. Nordman. “Laboratory investigations into the dimensional stability of paper.” In: *Technical Association of the Pulp and Paper Industry* 41 (1958), pp. 23–30.
- [48] Stanley Osher and Ronald Fedkiw. *Level Set Methods and Dynamic Implicit Surfaces*. 1st. Springer-Verlag New York, 2003, p. 273.
- [49] D.H. Page and P.A. Tydemann. “A new theory of the shrinkage, structure and properties of paper.” In: *Transactions of the symposium held at Oxford, ed.F.Bolam. London: Technical Section, British Paper and Board Makers’ Association* (1961), pp. 397–421.
- [50] D.H. Page and P.A. Tydemann. “Transverse swelling and shrinkage of softwood tracheids.” In: *Nature* 199 (1963), pp. 471–472.
- [51] J. Panek, C. Fellers, and T. Haraldsson. “Principles of evaluation for the creep of paperboard in constant and cyclic humidity.” In: *Nordic Pulp and Paper Research Journal* 19 (2004), pp. 155–163.

- [52] R.H.J. Peerlings and N.A. Fleck. “Computational evaluation of strain gradient elasticity constants.” In: *International Journal for Multiscale Computational Engineering* 2 (2004), pp. 599–619.
- [53] M.K. Ramasubramanian and R.W. Perkins. “Computer simulation of the uniaxial elastic-plastic behavior of paper.” In: *ASME Journal of Engineering Materials and Technology* 110 (1988), pp. 117–123.
- [54] M.C. Rivara. “New longest-edge algorithms for the refinement and/or improvement of unstructured triangulations.” In: *International Journal for Numerical Methods in Engineering* 40 (1997), pp. 3313–3324.
- [55] D. Roylance. *Mechanics of Materials*. 1st Edition. Wiley and Sons, 1996.
- [56] A. Sabit. “Paper machine clothing: Key to paper making process.” In: *CRC Press 1st edition* (1997).
- [57] L. Salmen and A.M. Olsson. “Mechanosorptive creep in pulp fibres and paper.” In: *Wood Science and Technology* 48 (2014), pp. 569–580.
- [58] L. Salmen, A.M. Olsson, and F. Dong. “Fibre morphological effects on mechano-sorptive creep.” In: *Wood Science and Technology* (2010), pp. 475–483.
- [59] L. Salmen, R. Boman, C. Fellers, and M. Htun. “The implications of fiber and sheet structure for the hygroexpansivity of paper.” In: *Nordic Pulp Paper Research Journal* 2 (1987), pp. 127–131.
- [60] P. Samantray, R.H.J. Peerlings, T.J. Massart, and M.G.D. Geers. “Level set based extended finite element modeling of the response of fibrous networks under hygroscopic swelling.” In: *In preparation* ().
- [61] P. Samantray, R.H.J. Peerlings, T.J. Massart, and M.G.D. Geers. “Modeling the effects of creep in paper fibres under the influence of external loading and changes in moisture.” In: *In preparation* ().
- [62] P. Samantray, R.H.J. Peerlings, T.J. Massart, and M.G.D. Geers. “Modeling the irreversible behavior in paper networks subjected to moisture cycles.” In: *In preparation* ().
- [63] K. Schulgasser and D.H. Page. “The influence of transverse fibre properties on the in-plane elastic behaviour of paper.” In: *Composite Science and Technology* 32 (1988), pp. 279–292.
- [64] K.M. Sedlachek. “The effect of hemicelluloses and cyclic humidity on the creep of single fibers.” In: *Ph.D. Thesis. Institute of Paper Science and Technology. Atlanta.* (1995).
- [65] J. A. Sethian. *Level Set Methods and Fast Marching Methods*. Second. Cambridge University Press, 1999.
- [66] A. Shahsavari and R. Picu. “Size effect on mechanical behavior of random fiber networks.” In: *International Journal of Solids and Structures* 50 (2013), pp. 3332–3338.
- [67] O.M. Starzewski and D.C. Stahl. “Random fiber networks and special elastic orthotropy of paper.” In: *Journal of Elasticity* 60 (2000), pp. 131–149.
- [68] J. Strömbro and P. Gudmundson. “An anisotropic fibre-network model for mechano-sorptive creep in paper.” In: *International Journal of Solids and Structures* 45 (2008), pp. 5765–5787.
- [69] N. Sukumar, D.L. Chopp, N. Moes, and T. Belytschko. “Modeling holes and inclusions by level sets in the extended finite-element method.” In: *Computer Methods in Applied Mechanics and Engineering* 190 (2001), pp. 6183–6200.

- [70] D. Tsarouchas and A.E. Markaki. “Extraction of fibre network architecture by X-Ray tomography and prediction of elastic properties using an affine analytical model.” In: *Acta Materialia* 59 (2011), pp. 6989–7002.
- [71] T. Uesaka. “General formula for hygroexpansion of paper.” In: *Journal of Material Science* 29 (1994), pp. 2372–2377.
- [72] T. Uesaka and D. Qi. “Hygroexpansivity of paper-effects of fibre to fibre bonding.” In: *Journal of Pulp and Paper Science* 20 (1994), pp. 175–179.
- [73] T.J. Urbanik. “Hygroexpansion-creep model for corrugated fiberboard.” In: *Wood and Fiber Science* 27 (1995), pp. 134–140.
- [74] A.K. Vainio and H. Paulapuro. “Interfiber bonding and fibre segment activation mechanism in paper.” In: *Nordic Pulp Paper Research Journal* 2 (2007), pp. 442–458.
- [75] Nick Verschuur. “Robust Measurement of Paper Fiber surface Hygroexpansion using Global Digital Height Correlation.” In: *Final Report* 161 (2018), pp. 23–41.
- [76] X.F.Wu and Y.A. Dzenis. “Elasticity of planar fiber networks.” In: *Journal of Applied Physics* 98 (2005), 093501(1)–093501(9).
- [77] L. Berhan L. Y.B. Yi and A.M. Sastry. “Statistical geometry of random fibrous networks, revisited: Waviness, dimensionality and percolation.” In: *Journal of Applied Physics* 96 (2004), pp. 1318–1327.

ACKNOWLEDGMENTS

Four and half years ago, I embarked on an entirely different journey of life. It has been a very rich and diverse experience in all these years that I will cherish for eternity. First of all my sincere thanks to my supervisor Ron Peerlings for being very kind and helpful towards me throughout the complete PhD studies. I still have fond memories of early morning meetings with you say 08:30am in the first years of my studies since I was staying in the university campus. Also, I would like to express my gratitude towards Marc Geers for providing me critical feedback during the tenure of the PhD. I would also like to thank Thierry Massart for inspiring and guiding me during my stay at Brussels which constituted the vital last 1.5 years of PhD. Looking back, I realized all these years are filled with wonderful scientific experiences. I am highly indebted to all you.

A lot of thanks to CIMNE, Barcelona for bestowing me the opportunity and funds to carry research work as a PhD student through the Simulation in Engineering and Entrepreneurship Development (SEED) program. I would also like to thank Océ (A Canon company) especially Dr. Louis Saes for funding a part of my project as well as monitoring the research activities.

In the course of studies, I made a lot of new friends. During the first two years of my PhD, I was located at room 4.18 in Gemini zuid, TU/e where I was with Frank, Christos and Maxime. Later, Debarshi and Konstantinos joined us. I want to thank all of you. Also, I would like to thank Varun Shah, Maqsood, Siavash, Awital, Tarek, Franz in the Mechanics of materials group.

During my studies at the ULB, Brussels, I would like to thank the people in the university Roland, Peter, Rohit, Lee, Gerrit, Karim, Zoltan and Batoma. I really enjoyed all of your company. Also, I would like to thank Sibren and Alejandro for the nice activities in Brussels.

I would also like to thank all the friendly people in the biomedical group Martijn, Gitta, Bregje, Tilai, Tamar, Jan-Willem, Cas, Cristina, Cansu, Celien. I really enjoyed the last days of the PhD due to the cheerful environment in the office 4.09.

More importantly, I would like to express gratitude to Luv, Hector, Maxime, Varun Raj, Zoltan, Ondrej, Aslan, Emanuela, Satheesh and Chetan for being supportive during the vital stages of my PhD.

On a final note, special thanks to my late mom, dad and sister for all the support.

CURRICULUM VITAE

Priyam Samantray was born on 11th July, 1987 in Bhubaneswar, India. He completed his primary school education in 2003 at D.A.V Public school. After finishing secondary school in 2005 at Kendriya Vidyalaya in Bhubaneswar, he underwent a one-year preparatory course for the engineering entrance examination. Subsequently, he started his four year study in Bachelor in Civil Engineering, NITK Surathkal. During his studies, he worked as a summer researcher at IIT Kharagpur, India for couple of months on computational sciences.

Next, he started his master studies on Computational Mechanics at UPC in Barcelona, Spain from 2012 after receiving an Erasmus Mundus scholarship. During the course of studies, he completed an internship at CIMNE in Barcelona for three months. After completion of one year, he did another internship at IST in Lisbon for three months on the study of freight distribution systems in the world. Thereafter, he began his second year of Erasmus Mundus master program at the University of Stuttgart in Germany. He completed his studies in 2014 with a master thesis where he implemented advanced algebraic turbulent models on a staggered grid.

Subsequently, he started a joint doctoral project in the Department of Mechanical Engineering at the TU Eindhoven, Netherlands in the last month of 2014 under supervision of R.H.J. Peerlings, T.J. Massart and M.G.D. Geers. During the studies, he spent one and half year at the secondary institution ULB, Brussels, Belgium as a requirement for the joint doctorate programme. His research focused on gaining insights on the micro-level parameters that determine the macro-level behavior of sheets of paper. This has further importance on understanding several problems of practical importance in the fields of paper, printing and packaging among others.